Reaction mechanism development and numerical modeling of biomass gasification process

A thesis accepted by the Faculty of Aerospace Engineering and Geodesy
of the University of Stuttgart in partial fulfillment of the requirements for
the degree of Doctor of Engineering Sciences (Dr. -Ing.)

by

Koruwage Christopher Niranjan Fernando

born in Panadura, Sri Lanka

main referee: Prof. Dr. rer. nat. Uwe Riedel

co-referee: Prof. Dr. -Ing. Henning Bockhorn

date of defense: 28.04.2021

Institute of Combustion Technology for Aerospace Engineering

University of Stuttgart

2021

Acknowledgement

Outline

Kurzfassung

Angesichts der negativen Auswirkungen durch die Nutzung fossiler Brennstoffe auf die Umwelt und der steigenden Preise fossiler Brennstoffe gewinnt die Suche nach erneuerbaren Energiequellen weltweit zunehmend an Interesse. Biomasse ist eine solch erneuerbare Energiequelle, die zur Erzeugung grüner Energie genutzt werden kann. In seiner natürlichen Form ist Biomasse allerdings für die meisten industriellen Anwendungen nicht geeignet, was vor allem auf den geringeren Energiegehalt zurückzuführen ist. Daher kommen Technologien zur Erhöhung der Energiedichte von Biomasse zum Einsatz. Die Flugstromvergasung ist ein weit verbreiteter thermochemischer Umwandlungsprozess, der Biomasse in ein Gemisch brennbarer Gase, das sogenannte Synthesegas (auch Syngas genannt), umwandelt, das anschließend weiter in konventionelle Brennstoffe umgewandelt werden kann.

Bei der Flugstromvergasung wird der Brennstoff von der Oberseite des Vergasers in eine Umgebung mit hoher Temperatur eingespritzt. Die Wechselwirkung des Brennstoffs mit der Hochtemperaturumgebung führt zu dessen thermischer Zersetzung, wobei letztendlich Synthesegas entsteht. Das vom Karlsruher Institut für Technologie (KIT) entwickelte bioliq®-Verfahren konzentriert sich zum Beispiel auf die Herstellung von individuell angepassten Brennstoffen aus Biomasse. Der Flugstromvergaser des bioliq®-Verfahrens verwendet als Brennstoff für die Vergasung ein Bio-Öl, das in einer Biomasse-Pyrolyse gewonnen wird.

Die Untersuchung und die Optimierung von Flugstromvergasungsprozessen können durch die Anwendung eines experimentellen und/oder eines Modellierungsansatzes erfolgen. Aufgrund des Kosten- und Zeitaufwandes für experimentelle Studien gewinnen numerische Modelle als möglicher Ansatz für die Durchführung von Optimierungsstudien zunehmend an Bedeutung.

Für die Einbindung der chemischen Kinetik der Brennstoffvergasung in numerische Modelle ist ein geeigneter chemisch-kinetischer Reaktionsmechanismus erforderlich. Die zuvor genannten Bio-Öle sind komplexe Mischungen und bestehen aus vielen verschiedenen chemischen Komponenten. Diese komplexe Zusammensetzung erschwert die Entwicklung von Reaktionsmechanismen für Vergasungsprozesse. Für die Lösung dieses Problems wird auf das Konzept von Ersatzbrennstoffen zurückgegriffen. Ein Ersatzbrennstoff ist ein Modellkraftstoff, der die physikalischen und chemischen Eigenschaften von

Biomasse-Pyrolyseöl annähert und gleichzeitig eine einfache chemische Zusammensetzung aufweist.

In der vorliegenden Arbeit wird Ethylenglykol als ein Einkomponenten-Ersatzkraftstoff verwendet, um das Bio-Öl im Flugstromvergasungsprozess abzubilden. Dadurch wird die Kinetik der Bio-Öl-Vergasung durch die Kinetik der Ethylenglykol-Vergasung angenähert. Reaktionsmechanismen für die Beschreibung der Kinetik zur Brennstoffoxidation und pyrolyse können in detaillierte, reduzierte und globale Mechanismen eingeteilt werden. Detaillierte Mechanismen beschreiben den Prozess der Brennstoffoxidation über einen weiten Bereich von Betriebsbedingungen, reduzierte Mechanismen hingegen nur über einen relativ kleinen Bereich, während globale Mechanismen einen äußerst eingeengten Anwendungsbereich aufweisen. Aufgrund der hohen Rechenzeiten, die für detaillierte Mechanismen erforderlich sind, finden diese keine praktische Anwendung in raumaufgelösten numerischen Modellen für Vergasungsprozesse. Deshalb müssen reduzierte Mechanismen entwickelt werden, die den relevanten Parameterbereich für den Vergasungsprozess gut abbilden.

In der vorliegenden Arbeit erfolgt daher die Entwicklung und Validierung eines reduzierten Reaktionsmechanismus für die Ethylenglykol-Vergasung, der auf einem an dem Deutschen Zentrum für Luft- und Raumfahrt (DLR) in Stuttgart entwickelten detaillierten Ethylenglykol-Mechanismus basiert. Für die Mechanismus-Reduktion werden drei unterschiedliche Methoden angewandt: Sensitivitätsanalyse, die sogenannte gerichtete Relationsgraphen-Methode und die kürzlich am DLR entwickelte lineare Transformationsmethode. Die so erzeugten reduzierten Mechanismen werden dann über die Berechnung von Zündverzugszeiten und laminaren Flammengeschwindigkeiten des Brennstoffes selbst sowie wichtiger Zwischenprodukte validiert, für Drücke zwischen 1 und 16 bar, für Temperaturen zwischen 800 und 1800 K und für Äquivalenz-Verhältnisse zwischen 0,5 und 2. Es zeigte sich, dass die reduzierten Modelle eine gute Übereinstimmung sowohl mit dem detaillierten Modell als auch mit den experimentellen Daten im untersuchten Parameterbereich aufweisen.

Der reduzierte Mechanismus mit den besten Ergebnissen wird mittels CFD Simulationen des am KIT betriebenen Forschungs-Flugstromvergasers (REGA) weiter validiert. Bei REGA handelt sich es um einen Versuchsaufbau, der für die Untersuchung des Flugstromvergasungsprozesses im Zusammenhang mit dem bioliq®-Verfahren entwickelt wurde. Die CFD-Simulationen werden mit dem Open-Source-CFD-Tool OpenFOAM

durchgeführt, wobei die Ergebnisse mithilfe der veröffentlichten experimentellen Daten aus dem REGA validiert werden. Anschließend erfolgt unter Verwendung des reduzierten Mechanismus eine Parameterstudie des REGA. Eine Reihe von CFD-Simulationen mit verschiedenen Brennstoffvorwärmtemperaturen, Äquivalenzverhältnissen und Betriebsdrücken wird durchgeführt, und der Einfluss dieser Betriebsbedingungen auf die Synthesegaserzeugung wird untersucht.

Abstract

With the adverse environmental impacts of fossil fuel use and the increasing prices of fossil fuels, search for renewable energy sources is gaining increased attention of researchers worldwide. Biomass is one such renewable energy source which can be used to produce green energy. However, biomass in its natural form is not suitable for most industrial applications. This is primarily due to the low energy content of biomass. Conversion technologies are therefore applied to increase the energy density of biomass. Entrained flow gasification is a widely applied thermo-chemical conversion process which converts the biomass into a mixture of combustible gases called the synthesis gas (syngas) which can further be converted into conventional fuels.

In the entrained flow gasification process, fuel is injected from the top of a gasifier to a high temperature environment. The interaction of the fuel with the high temperature environment leads to the thermal decomposition of the fuel, ultimately producing syngas. For example, the bioliq® process developed by the Karlsruhe Institute of Technology focuses on producing customized fuels starting from biomass. The entrained flow gasifier of the bioliq® process uses bio-oil obtained from biomass pyrolysis as the fuel for gasification.

In order to investigate and optimize entrained flow gasification processes, two main approaches are used. These are the experimental approach and the modeling approach. Due to the costs and time requirements of experimental studies over numerical models, numerical modeling is gaining popularity as a possible approach to conduct optimization studies.

In order to implement the chemical kinetics of fuel gasification into numerical models, a suitable chemical kinetic reaction mechanism is required. Bio-oils mentioned above are a complex mixture consisting of many different chemical components. This complex composition makes it difficult to develop reaction mechanisms to describe their gasification process. As a solution to this problem, the concept of a surrogate fuel is used. A surrogate fuel is a model fuel that approximates the physical and chemical characteristics of biomass pyrolysis oil while at the same time having a simple chemical composition.

In the present work, ethylene glycol is used as a single component surrogate fuel to represent the bio-oil in the entrained flow gasification process. The kinetics of the bio-oil gasification is therefore approximated by the kinetics of ethylene glycol gasification. The reaction mechanisms that describe the kinetics of fuel oxidation can be classified as detailed

mechanisms, reduced mechanisms and global mechanisms. Detailed mechanisms describe the fuel oxidation process over a wide range of operating conditions, reduced mechanism describe the fuel oxidation process over a relatively narrow region while global mechanisms have a very narrow range of applicability. With the high CPU time demands required by detailed mechanisms, they do not find practical applications in space-resolved numerical models for gasification processes. Therefore, reduced mechanisms which perform well in the interested parameter range of the gasification process need to be developed.

Therefore, in the present work, a reduced reaction mechanism for ethylene glycol gasification is developed and validated. This reduced reaction mechanism is based on a detailed ethylene glycol mechanism developed earlier at the German Aerospace Center (DLR) Stuttgart. Three different reduction methods, namely: sensitivity analysis, directed relation graph method and a linear transformation method recently developed at DLR are applied to obtain three variants of reduced mechanisms. These reduced mechanisms are then validated using ignition delay time calculations and laminar flame speed calculations with respect to the fuel and other major intermediates. Validation is performed for pressures between 1 and 16 bar, temperatures between 800 and 1800 K and equivalence ratios between 0.5 and 2. It has been found that the reduced mechanisms show good agreement with both the detailed mechanism and the experimental data over the parameter range investigated.

The best reduced mechanism is further validated using CFD simulations of the research entrained flow gasifier (REGA) operated at the Karlsruhe Institute of Technology. The REGA is an experimental setup developed to study the entrained flow gasification process related to the bioliq® process. The CFD simulations are performed using the open source CFD tool OpenFOAM. The results of the CFD simulations are validated by using the published experimental data from the REGA. Then, the reduced mechanism is used to conduct a parameter study of the REGA. A series of CFD simulations are performed using different fuel preheat temperatures, equivalence ratios and operating pressures and the effect of these operating conditions on the syngas production is studied.

List of Figures

List of Tables

Nomenclature

Roman letters

a	Pre exponential factor
a_R	Absorption coefficient (m^{-1})
A_s	Species A_s
b	Temperature exponent
c_i	Concentration of species i (mol m^{-3})
c_p	Specific heat capacity under constant pressure (J K^{-1} kg^{-1})
c_{pi}	Specific heat capacity of ith species under constant pressure (J K^{-1} kg^{-1})
C_D	Drag coefficient
d_l	Diameter of the liquid phase droplets (m)
$D_{i,eff}$	Effective diffusivity of ith species (m^2 s^{-1})
E	Activation energy (J mol^{-1})
g	Gravitational acceleration (m s^{-2})
G	Radiation intensity (W m^{-2})
$\dot{h}_i$	Rate of energy generation in the ith phase (W m^{-3})
H_i	Specific enthalpy of the ith phase (J kg^{-1})
$I(r,s)$	Intensity of radiation at position r in the direction of vector s (W m^{-2} sr^{-1})
I_{AB}	Importance index of species B to the production rate of species A
$I_b(r)$	Blackbody radiation intensity at position r (W m^{-2} sr^{-1})
$I_-(s_i)$	Incident intensity at point r from the direction s_i (W m^{-2} sr^{-1})
k	Turbulent kinetic energy (m^2 s^{-2})
k_r	Rate constant of reaction r
K_{lg}	Momentum transfer coefficient
K_p	Equilibrium constant
$\dot{m}_i$	Rate of mass generation in the ith phase (kg m^{-3} s^{-1})
$\dot{m}_s$	Rate of mass generation of species s (kg m^{-3} s^{-1})
$\dot{m}^*$	Mass transfer rate between the fine structures and the surrounding gas phase (s^{-1})
M_i	Interphase momentum transfer rate (kg m^{-2} s^{-2})
M_v	Molar mass of the vapor (kg mol^{-1})
M_∞	Molar mass of the gas phase (kg mol^{-1})
n	Refractive index
Nu	Nusselt number
p	Pressure (Pa)
p^{new}	New pressure field to be used in the momentum predictor step (Pa)
p^{old}	Pressure field used in the previous momentum predictor (Pa)
p^p	Pressure solution (Pa)
$P_{sat}(T_l)$	Saturation pressure at liquid phase temperature T_l (Pa)
P_∞	Pressure of the gas phase (Pa)
q_r	Radiation heat flux (W m^{-2})
r_i	Reaction rate of ith reaction (mol s^{-1})
R	Universal gas constant (J mol^{-1} K^{-1})
R_d	Droplet radius (m)
R_i	Reynolds stress tensor of the ith phase (kg m^{-1} s^{-2})
R_k	Rate of production of species k per unit volume (mol m^{-3} s^{-1})
$\bar{R}_k$	Average rate of production of species k per unit volume (mol m^{-3} s^{-1})

R'	Specific gas constant (J kg^{-1} K^{-1})
S	Total number of species in the mechanism
S_f	Face surface area vector (m^2)
S_G	Radiation source term in P1 equation (W m^{-3})
S_{ij}	Sensitivity coefficient
$S_\emptyset$	Source term for scalar $\emptyset$
t	Time (s)
T	Temperature (K)
T_l	Liquid phase temperature (K)
u	Instantaneous flow velocity (m s^{-1})
u'	Fluctuating velocity component (m s^{-1})
U_i	Average velocity of the ith phase (m s^{-1})
U_r	Relative velocity between gas and solid phase (m s^{-1})
V_P	Cell volume with cell center P (m^3)
X_l	Mole fraction of the liquid phase
$X_{v,sat}$	Vapour saturation mole fraction
$\tilde{Y}_k$	Average species mass fraction
$Y_k{}^*$	Mass fraction of species k in the fine structures
Y_s	Mass fraction of species s
$Y_{v,sat}$	Vapour saturation mass fraction
$Y_{v,\infty}$	Mass fraction of the vapour in the gas phase

Greek letters

α_p	Pressure under-relaxation factor
γ^*	Volume fraction of the fine structures
ΔG	Gibbs energy difference between products and reactants (J mol^{-1})
Δh^0	Standard enthalpy difference between products and reactants (J mol^{-1})
ΔT	Temperature difference (K)
ε	Turbulent kinetic energy dissipation rate (m^2 s^{-3})
ε_g	Volume fraction of gas phase
ε_i	Volume fraction of ith phase
ε_l	Volume fraction of liquid phase
λ	Thermal conductivity (W m^{-1} K^{-1})
λ_g	Thermal conductivity of the gas phase (W m^{-1} K^{-1})
$\lambda_{i,eff}$	Effective thermal conductivity of ith species (W m^{-1} K^{-1})
μ_t	Turbulent viscosity (Pa s)
υ	Kinematic viscosity (m^2 s^{-1})
υ_{Ai}	Stoichiometric coefficient of species A in reaction i
$\upsilon_{rs}{}^{(e)}$	Stoichiometric coefficient of species s in the educts of reaction r
$\upsilon_{rs}{}^{(p)}$	Stoichiometric coefficient of species s in the products of reaction r
ρ	Density (kg m^{-3})
ρ_i	Density of the ith phase (kg m^{-3})
ρ_g	Density of the gas phase (kg m^{-3})
σ	Stefan Boltzmann constant (W m^{-2} K^{-4})
σ_S	Scattering coefficient (m^{-1})
τ_{ch}	Chemical kinetic time scale (s)
τ_m	Turbulent mixing time scale (s)

$\emptyset$	A general scalar field
$\emptyset_f$	Value of field $\emptyset$ at face center
$\emptyset_P$	Value of field $\emptyset$ at cell center P
$\emptyset_P{}^n$	Value of field $\emptyset$ at cell center P at current time step
$\emptyset_P{}^0$	Value of field $\emptyset$ at cell center P at previous time step
$\Phi(s_i, s)$	Scattering phase function
χ	Scalar diffusion coefficient
Ω	Solid angle (sr)

Subscripts

eff	Effective property
g	Gas phase
i	i^{th} phase
l	Liquid phase
lg	Liquid-gas transfer
υ	Vapor
sat	Saturation value
∞	Ambient condition

Superscripts

(e)	Reactants
n	Iteration n
new	New solution
old	Old solution
(p)	Products

Abbreviations

CFD	Computational Fluid Dynamics
DRG	Directed relation graph
EDC	Eddy dissipation concept
KIT	Karlsruhe Institute of Technology
RANS	Reynolds averaged Navier Stokes
REGA	Research entrained flow gasifier
PaSR	Partially stirred reactor model

1. Introduction and Background

1.1 Biomass as a renewable energy source

With adverse effects on the environment and with increasing and volatile prices of fossil fuels, alternative and environmentally friendly renewable fuels are gaining increasing attention as a possible option to meet the world's energy demand [1].

Biomass is, amongst others, a promising feedstock for providing renewable energy [2 – 5]. Presently, a large quantity of biomass exploitable for energy production is existing as byproducts and waste in the agricultural industry and food processing industries [6]. In 2017, bioenergy accounted for nearly 9% of world's energy supply [1].

A main disadvantage of biomass is its low energy density [2]. Untreated biomass is inefficient to transport over long distances. Therefore, conversion technologies are utilized to convert biomass into gaseous and liquid fuels with a higher energy density.

The technologies available for energy densification of biomass can be classified into three main groups. They are bio-chemical, thermo-chemical, and extraction processes [7, 8]. In the bio-chemical conversion, biomass is subjected to digestion or fermentation processes. In these processes, biomass is decomposed by microorganisms, releasing combustible product gases. For example, biogas, which consists mostly of methane and carbon dioxide besides small amounts of nitrogen, hydrogen and hydrogen sulphide is a typical product of bio-chemical conversion of biomass [9]. In the thermo-chemical conversion, biomass is decomposed into combustible chemical components by the use of heat [7]. The result is a liquid or gaseous fuel (mixture) with a higher energy density depending on the conversion process applied. Two widely applied thermo-chemical conversion technologies are pyrolysis and gasification. In the pyrolysis process, biomass is thermally decomposed by the use of heat in the absence of oxygen [10]. Depending on the operating conditions, the result of pyrolysis process is bio char or pyrolysis oil [10]. Gasification of biomass is considered as a very promising technique for supplying energy with important and significant benefits in terms of reduced GHG emissions, in particular CO_2.

1.2 Biomass gasification

Biomass gasification is the process of partial oxidation of biomass under fuel rich conditions to produce synthesis gas (syngas), a mixture of carbon monoxide (CO) and

hydrogen (H_2) [11]. Syngas can be used in a variety of ways. These include electricity generation, heat generation, and hydrogen production [12]. Syngas can also serve as a source for producing synthetic chemicals including conventional liquid fuels such as kerosene, petrol, and diesel through conversion processes such as the Fischer-Tropsch process [13]. The typical composition of a synthetic gas is given in Table 1.1.

The reactor in which the gasification process is carried out is called a gasifier. The gasification process can be started directly from raw biomass [14] or by using the fuel produced by a pyrolysis process. For example, in the bioliq® process, the pyrolysis oil produced by flash pyrolysis of biomass is used in an entrained flow gasification process to produce syngas [15].

In a typical gasification process, the biomass fuel is brought into contact with a gasifying medium (oxidizer) which is in the gas phase (Fig. 1.1). The gas phase is maintained at a high temperature (typically 1500 K) by the oxidation reactions of the fuel and, if needed, optionally through external heating of the reactor. The high temperatures of the gas phase initiate the thermal decomposition of the fuel [16].

First, the heat absorbed by the biomass from the gas phase is used for moisture evaporation. This process is called drying. When the temperature of the biomass reaches about 500 K, thermal degradation starts resulting in the release of volatile gases; these gases include hydrogen, carbon monoxide, carbon dioxide, and methane. During this process, a fraction of the raw biomass is converted into biochar, via pyrolysis [10].

In the next stage of the gasification process, two sets of reactions take place: First, heterogeneous reactions of the biochar with the gas phase; and second, homogenous reactions of the volatiles released during pyrolysis with the gas phase. The biochar react with the oxygen supplied in the gasification agent, as well as with carbon dioxide, hydrogen, and water vapor in the gas phase producing carbon dioxide, carbon monoxide, hydrogen, and methane [11, 17]. This process step is named gasification of biochar.

In the gas phase, volatiles released during the pyrolysis stage reacts with oxygen, producing water vapor, carbon dioxide, and carbon monoxide. Further, carbon monoxide and water vapor react to form carbon dioxide and hydrogen through the so called water gas shift reaction ($CO + H_2O \leftrightharpoons CO_2 + H_2$). These processes take place along the height of the gasifier. At the exit, syngas is obtained. A schematic of the fuel conversion taking place within the gasification process is presented in Fig. 1.1.

H$_2$O   CO, CO$_2$, CH$_4$ +O$_2$ +CO$_2$ +CO

Raw Biomass → Moisture evaporation → Volatile release → Biochar → Syngas
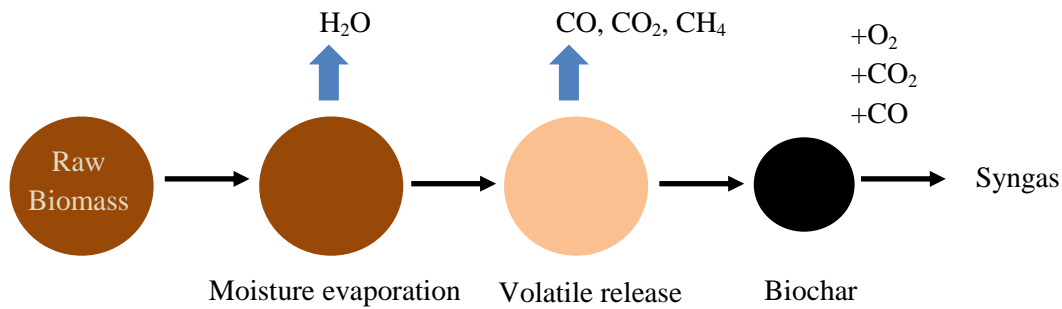
Figure 1.1: Gasification process.

Table 1.1: Typical composition of syngas as obtained from biomass gasification [18, 19].

Species	Composition (vol %)
H$_2$	5 – 17
CO	10 – 22
CH$_4$	1 – 7
CO$_2$	8 – 20
N$_2$	40 – 60

1.2.1 Types of gasifiers

Gasifiers can be classified into three main designs [11]: (i) Packed bed gasifiers; (ii) Fluidized bed gasifiers, and (iii) Entrained flow gasifiers.

The following sections discuss the operating principles, advantages, and disadvantages of these designs.

1.2.1.1. Packed bed gasifiers

Packed bed gasifiers consist of a packed bed of biomass inside a vertical reactor. Feed biomass is typically wood which is grinded into small pieces. The gasification agent (usually air) is driven through the packed bed. Three configurations of packed bed gasifiers exist: Updraft, downdraft, and cross flow [11]. These configurations are illustrated in Fig. 1.2. In each configuration, the operating principle is the same: Part of the biomass packed bed is ignited, in case of an updraft gasifier the packed bed is ignited at the bottom. This results in the development of a combustion zone in the lower part of the packed bed. The combustion zone consumes the oxygen present in the gasifying agent and increases its temperature. The oxygen free hot gas mixture leaving the combustion zone causes pyrolysis and gasification

reactions in the next layers of the packed bed. The resulting syngas is recovered from the end of the packed bed at the exit of the reactor [11]. Packed bed gasifiers have the advantages of a simple design and operation as well as lower cost compared to other gasifier configurations [19]. Disadvantages are scale up limitations, flow problems within the packed bed, and a variable syngas composition over time due to the difficulty in maintaining a uniform temperature inside the packed bed [11, 19].

(a) Updraft gasifier (b) Downdraft gasifier (c) Cross flow gasifier
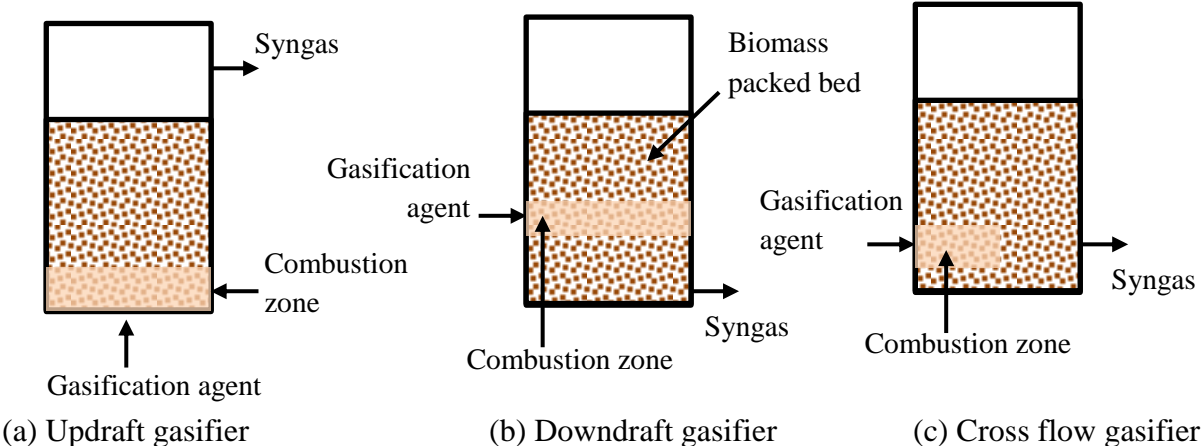
Figure 1.2: Configurations of packed bed gasifiers.

1.2.1.2 Fluidized bed gasifiers

In a fluidized bed gasifier, a bed of solid fuel particles is maintained in a suspension of the gasifying agent by introducing the gasifying agent from the bottom of the reactor. The mixing in the fluidized bed results in a uniform temperature over the bed [19]. A downstream cyclone separator is required to separate particles that are carried away in the exit gas and to re-introduce them to the gasifier [20]. Advantages of fluidized bed gasifiers include ability to operate it with fuels with high ash content, fuel flexibility, and the ability to operate at high pressures [11]. Disadvantages include complexity in operation due to maintenance of a fluidized bed and requirement of extensive downstream gas treatment due to the need of unconverted particle recovery and dust separation from the outlet gas [21]. A schematic diagram of a fluidized bed gasifier is shown in Fig. 1.3.
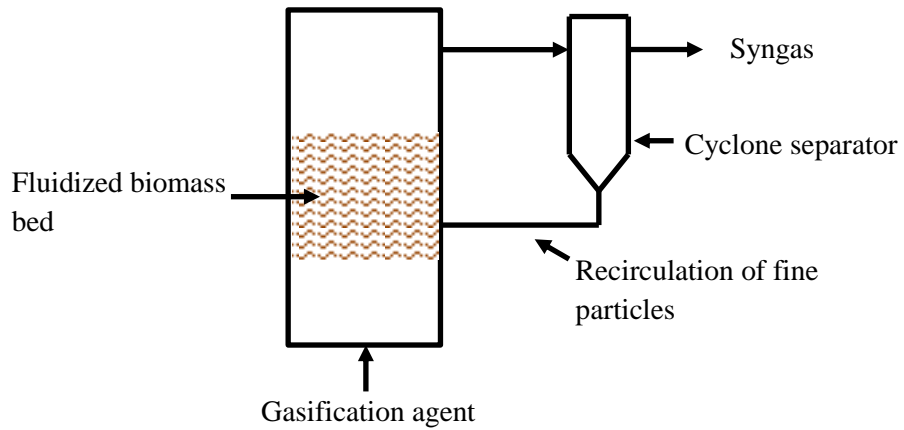
Figure 1.3: Schematic of a fluidized bed gasifier.

1.2.1.3 Entrained flow gasifiers

In an entrained flow gasifier, the fuel in droplet or powder form is injected together with an oxidizer at the top of the gasifier into a high temperature environment [22]. The schematic diagram of an entrained flow gasifier is shown in Fig. 1.4.
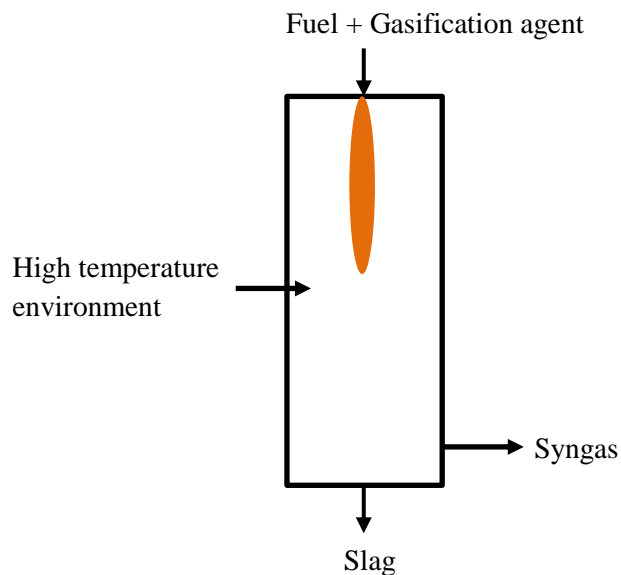
Figure 1.4: Schematic of an entrained flow gasifier.

After the injection, the oxidizer and the fuel spread into a cloud in which the oxidizer entrains the fuel. Due to the high temperature in the gasifier and the fineness of the fuel, the reaction

rates in an entrained flow gasication process are high, with a typical residence time of fuel in the reactor in the order of a few seconds [22]. Tars and other liquid products as produced during the fuel conversion become further converted to hydrogen and carbon monoxide [22], yielding a tar free syngas. Due to the high operating temperatures (typically around 1500 K) of the entrained flow gasification process, the exit gas is at a high temperature, making the thermal efficiency of the process low. To improve the thermal efficiency of the overall process, recovered heat from the exit gas can be applied to the pre-treatment of the fuel (*e.g.* drying). Major advantages of the entrained flow gasification process include the production of syngas with very low tar content and the fuel flexibility. Disadvantages include the complex operation and the requirement of a fine-sized feedstock [11].

1.3 The bioliq® process

The bioliq® process [15] is a recent example of the use of a centralized entrained flow gasifier to produce renewable fuels. It is initiated by the Karlsruhe Institute of Technology (KIT), Germany, with the goal to produce liquid fuels starting from low grade biomass feedstock [15]. This process can be divided into four stages: (1) Pyrolysis of the biomass feed stock using flash pyrolysis reactors in decentralized facilities, (2) Preparation of a bio slurry by mixing the bio char and bio oil produced in the pyrolysis stage, (3) Subjecting the bio slurry to a high pressure entrained flow gasification process in a centralized plant to produce syngas, and (4) cleaning and processing of syngas into synthetic fuels.

The starting raw material of the process can be almost any type of biomass, with a main focus on the residues from the agricultural industry, forestry, and landscaping [15]. In the first stage, raw biomass is pre-treated by drying and pulverizing. Then, the conditioned biomass is mixed with hot sand in a twin screw mixing reactor and subjected to a flash pyrolysis process under the absence of oxygen. The pyrolysis process takes place at around 800 K and produces pyrolysis oil and pyrolysis char as the output from the reactor. The relative quantities of oil and char depend on the type of biomass subjected to pyrolysis. The bio chars are mixed with the pyrolysis oil to produce a so-called slurry named as biosyncrude® [15].

In the next stage, biosyncrude® is subjected to entrained flow gasification in order to produce syngas in a centralized plant. The gasifier is operated in a pressure range of 40-80 bar and at a temperature exceeding 1500 K [15].

The third stage of the process comprises gas purification and fuel synthesis steps. After purification, syngas is to be processed, *e.g.*, into dimethyl ether and, further on, into gasoline

[15]. A variety of pathways are open for processing syngas into gaseous and liquid fuels. For example, through the Fischer-Tropsch process [13], syngas can be processed to obtain fuels like LPG (liquefied petroleum gas), kerosene, and diesel. A schematic diagram of the bioliq® process is presented in Fig. 1.5.

Biomass

Pyrolysis oil

Pretreatment

High pressure entrained flow gasification

Flash pyrolysis

Syngas

Cleaning

Fischer-Tropsch process

Pyrolysis oil

Synthetic Fuel
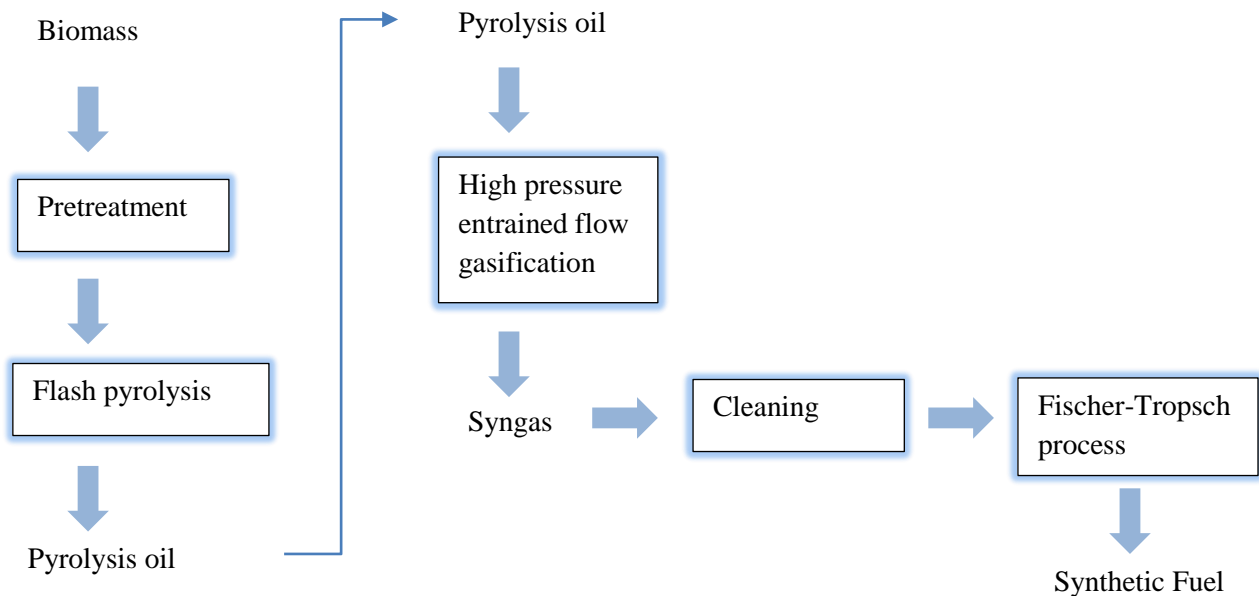
Figure 1.5: Schematic of the bioliq® process.

1.4 Approaches for the design and optimization of gasification processes

The composition and the heating value of the syngas leaving a gasifier depend on several global factors. These include the specific gasification technology [19] (fixed bed, fluidized bed, and entrained flow) and gasification agent, the composition and physical nature of the fuel, as well as the operating pressure, temperature, and equivalence ratio [23]. This dependence makes it difficult to find common principles for optimizing the performance of gasifiers. Therefore, the optimization of the gasifier performance is highly case dependent. Only rough values or tendencies can be identified from literature to be used as a guideline for process optimization or to select a suitable design point. Hence, a case dependent optimization is necessary. Two major approaches are used for the optimization studies of gasifiers: Experimental approach and modeling approach.

The experimental approach consists of conducting a series of experiments using the gasifier of interest under different operating parameters [24 – 27]. For example, to study the effect of equivalence ratio on the composition of syngas, a series of test runs are performed for

different equivalence ratios [27]. However, the experimental approach has the disadvantage of cost, time consumption, and difficulties in the measurements (in industrial operational units).

Due to these disadvantages and challenges related to the experimental approach, numerical modeling is gaining more attraction as a technique for designing and optimizing gasifiers. The models vary from simple zero dimensional equilibrium models to predict the final gas composition of the gasifier, to three dimensional, turbulent CFD simulations [28 – 31]. In the following section, a brief overview of different numerical models used for the modeling of biomass gasification processes is presented, including applications, advantages, and disadvantages of each model.

1.5 Numerical models of biomass gasification processes

The numerical models used to study gasification process can be divided into two main categories; single particle models (*e.g.*[16, 32, 33]) and reactor models (*e.g.* [34 – 36]). Single particle models focus on the conversion of a single biomass particle in a surrounding gas phase. The purpose of these models is to improve the understanding of the particle conversion kinetics and relevant transport phenomena such as heat and mass transfer processes associated with the particle.

Reactor models focus on studying the behavior of the entire reactor (gasifier) involved in the gasification process with the aim of reactor design and reactor optimization. Because hundreds and even thousands of biomass particles can be present in a gasifier, reactor models usually introduce simplifying assumptions in modeling the gasification process. The simplest type of such reactor models is called the equilibrium model (*e.g.* [29, 37]). In these models, only the equilibrium relationship between the inlet flow stream and the outlet flow stream is derived using the mass balances and equilibrium assumptions. But information related to spatial and temporal variation of the flow fields (species concentrations, temperature, velocity) inside the reactor cannot be extracted using these equilibrium models. Therefore, such models are usually applied to get a rough estimate of the composition of the outlet syngas for a given inlet composition.

One-dimensional reactor models calculate the flow field along the axis of the reactor. They are useful to determine the axial variation of quantities such as temperature and species concentrations. However, one-dimensional models have the following limitations: they cannot predict the radial variation of flow fields and they cannot take into consideration the radial effects on gasification process such as flow recirculation.

Two- and three-dimensional models overcome most of the shortcomings of one-dimensional models, at the expense of increased CPU time. In most situations, gasifiers can be considered as axisymmetric, which allows the reduction of a three-dimensional model to two dimensions by using suitable boundary conditions. These higher dimensional models are usually built using the tools of CFD and solved using the finite volume method. Two main approaches for CFD modeling can be identified: (i) The Euler-Lagrange approach and the (ii) Euler-Euler approach [38, 39].

In the Euler-Lagrange approach, calculations on individual fuel particles are performed to some extent, by dividing the initial particle cloud into a finite number of packets. The motion of each packet through the computational domain is then resolved using forces acting on the particle packet. In the Euler-Euler approach, both the fuel and the gas phase are treated as continua. The motion of each phase is calculated by solving the Navier-Stokes equations. The present work uses the Euler-Euler approach to model the two phase gasification process.

Even though mathematical modeling is widely applied to study and optimize gasification processes, a significant amount of research still needs to be done in order to improve the accuracy of these models [40], in particular two and three dimensional ones. The main difficulties in model design result from insufficient understanding of the various sub-processes involved in biomass gasification. These include biomass combustion, pyrolysis, gasification, evaporation process, as well as the formation of ash and tar. To develop reliable mathematical tools to simulate biomass gasification processes, a detailed understanding of physics and chemistry of these processes is necessary, especially in terms of chemical kinetics. The current approach to this problem is a combination of experimental and modeling framework, where experiments provide the insights required and needed to develop different mathematical models, then, these models are, in turn, compared against experimental data for validation.

In the next section, an experimental set up is described which is designed to provide important validation data for entrained flow gasifier models and which is used in the present work as the basis for modeling the entrained flow gasification process.

1.6 The Research Entrained Flow Gasifier (REGA)

The Research Entrained Flow Gasifier (REGA) developed at the Karlsruhe Institute of technology (KIT) is a laboratory scale experimental test facility to study the entrained flow gasification process at atmospheric pressure [41]. The REGA consists of a vertically

positioned ceramic tube of internal diameter 0.28 m and a length of 3.00 m. Sampling probes and optical access are provided along the reactor to allow the measurement of gas compositions and temperature [42]. A schematic of the REGA is shown in Fig. 1.6.
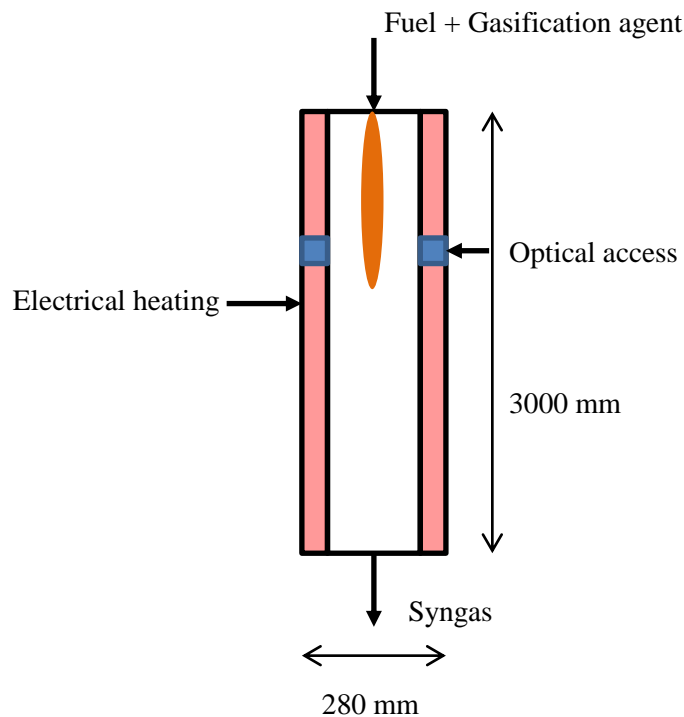
Figure 1.6: Schematic of the REGA [41, 42].

Due to the complexity of bio slurry used in industry (*e.g.* biosyncrude®), the experiments using the REGA reported so far in literature have used two different model fuels so far. These are ethylene glycol and ethylene glycol – biochar suspensions [41, 42]. The use of ethylene glycol as a model fuel and its chemistry will be discussed in detail in Chapter 2. These simplifications in the REGA experiments as compared to the high pressure bio slurry gasification in the bioliq® process are essential in terms of developing mathematical models, for several reasons. First, it is important to have a fuel with a well-defined composition for mathematical calculations. In this sense, the use of ethylene glycol in the REGA experiments provides useful validation data for developing and validating mathematical models. Second, the scientific principles of entrained flow gasification are still not well understood. Therefore it is preferable to start developing models at atmospheric conditions, which will be free from

any high pressure complications. Atmospheric experiments at REGA provide validation data for these atmospheric pressure mathematical models.

1.7 Goals and methodology of the present work

The present work focuses on the numerical modeling of the entrained flow gasification process with respect to the REGA geometry by using a comprehensive chemical kinetic reaction scheme to describe the fuel gasification process. Because of the complex chemical composition of real pyrolysis oil, ethylene glycol is selected as the model fuel for the biomass pyrolysis oil. This selection is based on the similarity of chemical and physical properties of ethylene glycol and of the pyrolysis oil.

In Chapter 2, the detailed combustion chemistry of ethylene glycol is discussed. Chapter 2 also presents the tools and the methodology used in the present work for the validation of the reaction mechanisms. Then, with the aim of using ethylene glycol chemistry in the CFD simulations of the REGA, a reduced reaction mechanism describing ethylene glycol gasification is developed based on the detailed reaction mechanism. Such a reduced reaction model is required because the very high CPU time demand of the detailed mechanism makes its use inefficient for CFD based parameter studies of the REGA. The reduced mechanism requires much less CPU time due to the considerably lower number of species and reactions. The detailed chemical-kinetic reaction mechanism is reduced in such a way that the performance of the generated reduced reaction model is in agreement with the one of the detailed reaction mechanism in the parameter range of interest for the selected target quantities. Chapter 2 presents the reduction procedure of the detailed mechanism and the reduction algorithms used. Three different reduced mechanisms are obtained using three different reduction algorithms. Validation of the reduced mechanisms is performed using ignition delay time calculations and laminar flame speed calculations of ethylene glycol and stable sub-species in the mechanism and comparing them with published experimental data.

Chapter 3 describes the governing equations as well as the physical and chemical sub models used by the Euler-Euler solver.

Chapter 4 presents the numerical solution of the CFD model. A description of the finite volume method, which is used to discretize the equations presented in Chapter 3 is given. Chapter 4 also describes the geometry of the REGA, the CFD mesh as well as initial and boundary conditions corresponding to the operating conditions of the gasifier.

Chapter 5 consists of results and discussion. First, the performance of the reduced mechanisms is presented with respect to ignition delay times and laminar flame speed computations of the specific fuels of interest. Next, the performance of the best reduced mechanism is presented in terms of two-dimensional Euler-Euler CFD simulations. Finally, the results of a parameter study performed using the validated reduced reaction mechanism are presented. Based on these results of the parameter study, the operating behavior of the gasifier under different temperature, pressure, and equivalence ratios is discussed.

2. Reaction mechanisms for ethylene glycol

This chapter describes the reaction mechanisms of ethylene glycol (EG) used in the present work and the methodology of validation of these mechanisms. First, reasons will be given why ethylene glycol was chosen as a model fuel for the pyrolysis oil. Then, the detailed chemical kinetic reaction mechanism for EG as developed at DLR Stuttgart [43] will be discussed. Next, the algorithms used for the reduction of the detailed EG reaction model will be presented. Finally, the methodology of validation of the reaction mechanisms is presented.

2.1 Ethylene glycol as a model fuel for biomass pyrolysis oil

In general, biomass feedstock comes from various sources. Examples are, wood, agricultural and animal residues, forestry residues, and wastes [44]. Biomass is composed of three main hetero-polymers: cellulose, hemicellulose, and lignin [45]. Depending on the specific source, the composition of biomass can vary significantly [45]. Table 2.1 presents the typical ranges of variation of these main components, in dry and ash free weight percentages (wt. % daf) [45].

Table 2.1: Typical composition of biomass.

Hemicellulose (wt. % daf)	Cellulose (wt. % daf)	Lignin (wt. % daf)	Other matter (wt. % daf)
20 – 40	24 – 51	15 – 53	0 – 10

When producing a pyrolysis oil through the pyrolysis process, the complex and varying composition of feed biomass results in a pyrolysis oil with a complex and varying composition, containing many different chemical components including aldehydes, ketones, phenols, acids, and oxygenates [46, 47]. For the modeling approach, the complex and varying composition of pyrolysis oil presents several problems. First, the presence of a large number of varying components makes it impossible to properly characterize the fuel in terms of component mass fractions, which is a necessary initial condition for mathematical models treating the fuel chemistry. Second, modeling of a fuel mixture with a large number of chemical components would require a complex reaction mechanism to describe the oxidation of the fuel. The implementation of such reaction mechanisms in CFD codes will result in very high CPU time demands making efficient CFD calculations impossible.

Therefore, as an alternative, previous studies have used ethylene glycol as a one-component surrogate fuel to represent pyrolysis oil [48, 49]. The use of a neat fuel (EG) makes the

development of a reaction model much simpler compared to the one of a multi-component fuel. The selection of ethylene glycol as a surrogate fuel for pyrolysis oil is based on the similar physical and chemical properties of ethylene glycol and pyrolysis oil. Table 2.2 presents a comparison of major chemical and physical properties of ethylene glycol to those of pyrolysis oil [50, 51]. Further, ethylene glycol is a low cost and non-toxic chemical, which is advantageous for its use in experiments. Due to these advantages, the oxidation chemistry of pyrolysis oil is modeled in the present work by the oxidation chemistry of ethylene glycol.

Table 2.2: Comparison of chemical and physical properties of ethylene glycol and bio-oil.

Property	Ethylene glycol [50]	Bio-oil [51]
Density (20 C, kg m^{-3})	1132	1100-1300
Dynamic Viscosity (cP)	18-56	40-100
Heat of combustion (MJ/kg)	16.96	16-19
C (wt %)	38.7	32-49
H (wt %)	9.7	6-8
O (wt %)	51.6	44-60

2.2 Detailed chemical kinetic reaction mechanism for ethylene glycol

Once the surrogate fuel is selected, the way it oxidizes in the gasification environment, through chemical reactions of the fuel with reactants in the surrounding gas phase, needs to be specified. There are three methods to specify the chemistry of the fuel oxidation in a mathematical model for gasification process: Global reaction mechanisms, reduced reaction mechanisms, and detailed reaction mechanisms.

Global reaction mechanisms are the simplest representations of the fuel oxidation. The oxidation of ethylene glycol can be expressed as a one-step global reaction as expressed in reaction R2.1.

$$C_2H_6O_2 + \frac{5}{2}O_2 \rightarrow 2CO_2 + 3H_2O \qquad\qquad R2.1$$

However, in a real combustion environment, the conversion of the fuel to products follows a complex pathway including many intermediate steps and elementary reactions [52]. Apart from the products indicated by the global reaction, several different stable products can be formed depending on the combustion environment. Therefore, an adequate description of the chemistry of the fuel gasification cannot be represented by the too simple global reaction model, which has only a narrow range of applicability [53]. Instead, a more detailed reaction

mechanism which describes the fuel conversion in the molecular level through a collection of elementary reactions is required.

In general, the oxidation of any fuel in the gas phase can be represented by a series of elementary reactions in the form as given for example in reaction R2.2 [52].

$$\sum_{s=1}^{S} v_{rs}{}^{(e)} A_s \longrightarrow \sum_{s=1}^{S} v_{rs}{}^{(p)} A_s \qquad\qquad R2.2$$

A_s represents species s; S is the total number of species in the reaction mechanism. $v_{rs}{}^{(e)}$ and $v_{rs}{}^{(p)}$, respectively are the stoichiometric coefficient of species A_s of the reactants (e) and of the products (p), respectively in reaction r.

The main difference between the reactions R2.1 and R2.2 is that the reactions presented in R2.2 are a set of elementary reactions, *i.e.* the reaction occurs in the gas phase through molecular collisions the way it is described by the equation. The global reactions have complicated rate laws with a very limited range of applicability in terms of pressure, temperature, and fuel equivalence ratio. In contrast, elementary reactions obey simple rate laws in a wide range of operating conditions. The rate law for the production of species i through an elementary reaction r is given by [52]:

$$\frac{\partial c_i}{\partial t} = k_r\big(v_{ri}{}^{(p)} - v_{ri}{}^{(e)}\big) \prod_{s=1}^{S} c_s{}^{v_{rs}{}^{(e)}} \qquad\qquad Eq.\,2.1$$

with the rate constant k_r given by the modified Arrhenius law [52].

$$k_r = aT^n exp\left(-\frac{E_{act}}{RT}\right) \qquad\qquad Eq.\,2.2$$

k_r is commonly referred to as rate coefficient; T is the temperature and R is the universal gas constant. The Arrhenius parameters, a, n and E_{act} are called: Pre-exponential factor, temperature exponent, and activation energy.

The reaction coefficients (reaction rates) of some reactions in the mechanism can be dependent on both the temperature and pressure, due to the participation of third bodies in elementary reactions [52]. The rate constant of a pressure dependent reaction is evaluated by using two limits of rate constant, the low pressure limit and the high pressure limit. The rate constant between these two limits is given by the fall-off expression (Eq. 2.3). The rate constant for pressure dependent reactions in the fall-off region are calculated using the F-

Center treatment according to Troe [52]. The Troe approach uses two different sets of rate constants; one set for high pressure limit (k_∞) and one set for low pressure limit (k_0) along with four additional parameters (a, T^*, T^{**}, T^{***}) [52].

The pressure dependent rate constant is given by,

$$k = k_\infty \left(\frac{P_r}{1 + P_r}\right) F \qquad Eq.\,2.3$$

P_r and F are given by

$$P_r = \frac{k_0[M]}{k_\infty} \qquad Eq.\,2.4$$

$$logF = logF_{cent} \left\{1 + \left[\frac{logP_r + c}{n - d(logP_r + c)}\right]^2\right\}^{-1} \qquad Eq.\,2.5$$

where:

$$F_{cent} = a\,exp\left(-\frac{T}{T^*}\right) + exp\left(-\frac{T^{**}}{T}\right) + (1 - a)exp\left(-\frac{T}{T^{***}}\right) \qquad Eq.\,2.6$$

and $n = 0.75 - 1.27 logF_{cent}, c = -0.4 - 0.67 logF_{cent}, d = 0.14$

The catalog of all the reactions of the form R2.2 which completely describes the oxidation of the fuel to products is called the detailed reaction mechanism for the oxidation of the fuel in question.

The first detailed reaction mechanism for EG oxidation has been developed by Hafner *et al.* [48]. By the time this model was developed, experimental data for EG oxidation to validate the mechanism was lacking. Therefore, the mechanism has been validated using experimental data for various stable species as produced as major intermediates within the mechanism [48].

The detailed reaction mechanism for EG which has been recently developed at DLR Stuttgart (hereafter referred to as the DLR-EG mechanism) [43] is an enhancement of the Hafner model. Main features are attributed to better thermodynamic data of species as well as of rate coefficients of EG decomposition reactions based on new experimental data on EG oxidation. The DLR-EG mechanism which is the first EG mechanism validated with experiments performed on EG [43] consists of 78 species and 574 reactions [43].

2.3 The reduction of the detailed reaction mechanism for ethylene glycol

The detailed DLR-EG mechanism presented in section 2.2 provides a suitable model for the implementation of EG chemistry in a CFD code to be able to simulate the entrained flow gasification process of a pyrolysis oil. However, the large number of species and reactions present in this reaction model (78 species and 574 reactions) require extensive CPU time for CFD simulations. Also, the detailed mechanism has a wide range of applicability in terms of temperature, pressure, and equivalence ratios, while the operating conditions of a gasifier are much narrower, fortunately. For example, the gasification processes are usually performed only under fuel rich equivalence ratios. For these reasons, the detailed DLR-EG model can be reduced further to a more compact reaction mechanism with a fewer number of species and reactions [54]. The reduction is performed in such a way that the performance of the reduced mechanism is similar to the detailed mechanism in the parameter range of interest. This reduced mechanism can be implemented in CFD simulations, reducing drastically the CPU time demand required for the calculations.

Therefore, in the present work, reduced reaction mechanisms for describing ethylene glycol oxidation are produced by using three different reduction algorithms based on the detailed DLR-EG mechanism. The algorithms used are: Sensitivity analysis [55, 56] the directed relation graph method (DRG) [57], and a novel linear transformation reduction tool, lin-TM, recently developed at DLR Stuttgart by Methling *et al.* [58]. In the following sections, the reduction algorithms and tools used to produce the reduced mechanisms are presented.

2.3.1 Sensitivity analysis and the RedMaster approach

The RedMaster tool [55, 56, 59] as developed at DLR Stuttgart utilizes sensitivity analysis to produce reduced reaction mechanisms. In the present work, the RedMaster tool has been exploited to produce a first version of the EG reduced mechanism.

The variation of the concentration of a certain species c_i can be obtained by the summation of the rate equation according to Eq. 2.1 over all reactions according to Eq. 2.7 [52].

$$\frac{\partial c_i}{\partial t} = \sum_{j=1}^{R} k_j \left(v_{ji}^{(p)} - v_{ji}^{(e)} \right) \prod_{s=1}^{S} c_s^{v_{js}^{(e)}} \qquad\qquad Eq.\,2.7$$

It is evident from Eq. 2.7 that the concentration c_i is dependent on the rate constants k_j and the concentrations c_s of the other species in the mechanism. Sensitivity coefficients S are used as a way to quantify this dependence.

The absolute sensitivity coefficient $S_{i,j}$ of concentration c_i to rate constant k_j is defined [52] by:

$$S_{i,j} = \frac{\partial c_i}{\partial k_j} \qquad\qquad Eq.\,2.8$$

The higher the value of this sensitivity coefficient, the more sensitive the concentration c_i is to the value of the rate constant k_j. Therefore, a higher sensitivity coefficient means that the specific reaction with the rate constant k_j is important for the prediction of the concentration of the specific species c_i.

Because specific rate constants in a mechanism may have different units due to the different molecularities of the specific reactions, absolute sensitivity coefficients cannot be directly compared against each other. Therefore, a relative sensitivity coefficient [52] is introduced:

$$S_{i,j}^{rel} = \frac{k_j}{c_i}\frac{\partial c_i}{\partial k_j} \qquad\qquad Eq.\,2.9$$

It is important to note that the dependent variable of a sensitivity analysis can not only be concentrations; it can also be an overall variable such as the laminar flame speed. For time dependent systems, sensitivity coefficients can be calculated at each time point; also, the coefficients can be integrated in the whole time domain to obtain a single coefficient.

In the present work, the RedMaster approach has been exploited by utilizing sensitivity analysis to produce a first version of the EG reduced mechanism. According to this method, first, a group of initial important species (designated by Ω) is identified which include reactants and products. Then, the importance of other species within the mechanism to the production rate of species in Ω is evaluated by the following normalized sensitivity coefficient S_j [56].

$$S_j = \sum_{i=1}^{n}\left(\frac{\partial ln R_i}{\partial ln c_j}\right)^2 \qquad\qquad Eq.\,2.10$$

Here, i represents the ith species in Ω. n is the number of species in Ω and R_i is the rate of production of the ith species in Ω. c_j is the concentration of the jth species within the mechanism.

The normalized sensitivity coefficient S_j represents the importance of species j in the mechanism to the production rate of important species. Higher S_j values indicate a higher importance [56].

Species to be included in the final reduced mechanism are identified in an iterative way. First, S_j values corresponding to all the species in the mechanism other than the species in Ω are evaluated. Then, those species with the highest S_j value are added to the species given in the list Ω; and the procedure is repeated until a predefined agreement with reduction targets are obtained. [56]. Fig. 2.1 presents an overview of the RedMaster reduction procedure.
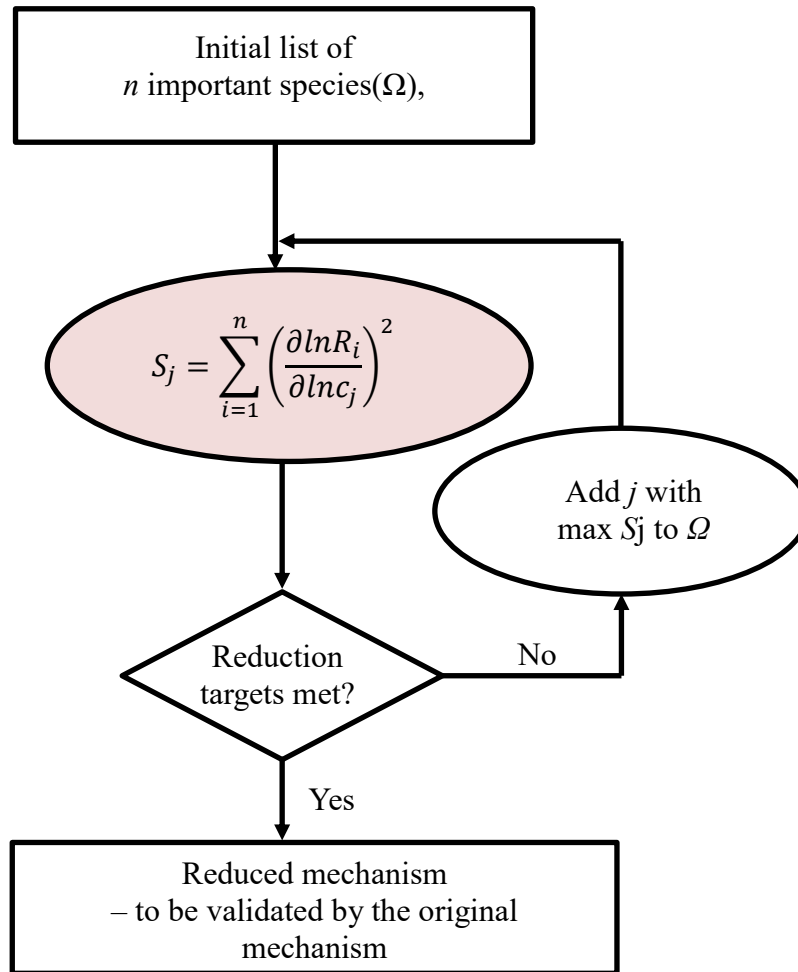
Figure 2.1: Schematic diagram of the RedMaster reduction procedure.

In the present work, the RedMaster tool is applied iteratively to produce the reduced mechanism. First, an initial version of the reduced mechanism is obtained using the procedure described above. Then, this initial version is validated against laminar flame speed data and ignition delay time data calculated using the detailed mechanism. Finally, this first version is

provided as the input mechanism to RedMaster for a further reduction step. This procedure is repeated until validation results showed significant deviation from the detailed mechanism, much higher than the selected deviation. The smallest mechanism that agrees well with the detailed mechanism, as well as experimental data, within the targets selected and the selected grade of agreement, is defined as the final reduced mechanism.

The reduced EG reaction mechanism obtained in the present work using the RedMaster tool is named Reduced Mechanism I (RM I) and consists of 49 species and 328 reactions. This is a reduction degree of approximately 40 % with respect to the number of species and 40% with respect to the number of reactions.

2.3.2 Directed Relation Graph (DRG) method

As a second method of reduction, the Directed Relation Graph method [57], as implemented in the software Chemical Work Bench [60], is applied.

The Directed relation graph method focuses on identifying and removing unimportant species in the detailed mechanism and their reactions [57]. In identifying the unimportant species, indirect dependence of species on each other are considered. For example, species A can be directly influenced by species B by both of them being present in the same reaction, and also A can be indirectly influenced by species C, which has a significant influence on B. Therefore, in order to predict the concentration of A sufficiently accurately, not only the species B should be kept in the mechanism but also species C. In the directed relation graph method, identification of such dependencies of species on each other is done through an iterative algorithm [57].

First, an importance index of species B to the production rate of species A is defined [57],

$$I_{AB} = \frac{\sum_{i=1}^{R} |v_{Ai} r_i| \delta_{B,i}}{\sum_{i=1}^{R} |v_{Ai} r_i|} \qquad\qquad Eq. 2.11$$

Here v_{Ai} is the stoichiometric coefficient of species A in reaction i. r_i is the reaction rate of ith reaction. $\delta_{B,i}$ is equal to unity if reaction i contains species B and zero otherwise.

If this index is greater than a user given threshold, then it is considered that species B is important to the production rate of species A.

To identify the important species in the mechanism, first a user given set of important species (Ω) is considered. Then for each species B in the detailed mechanism, important index is

evaluated with respect to the species in Ω. Their maximum value indicates how important the species B is to the mechanism. If this value is greater than the user given threshold value, species B is added to Ω and the whole procedure is repeated again. This task is performed until no further species are added to Ω. The final reduced mechanism consists of the species in Ω after the final iteration and their reactions [57]. Figure 2.2 presents a summary of the DRG reduction procedure.
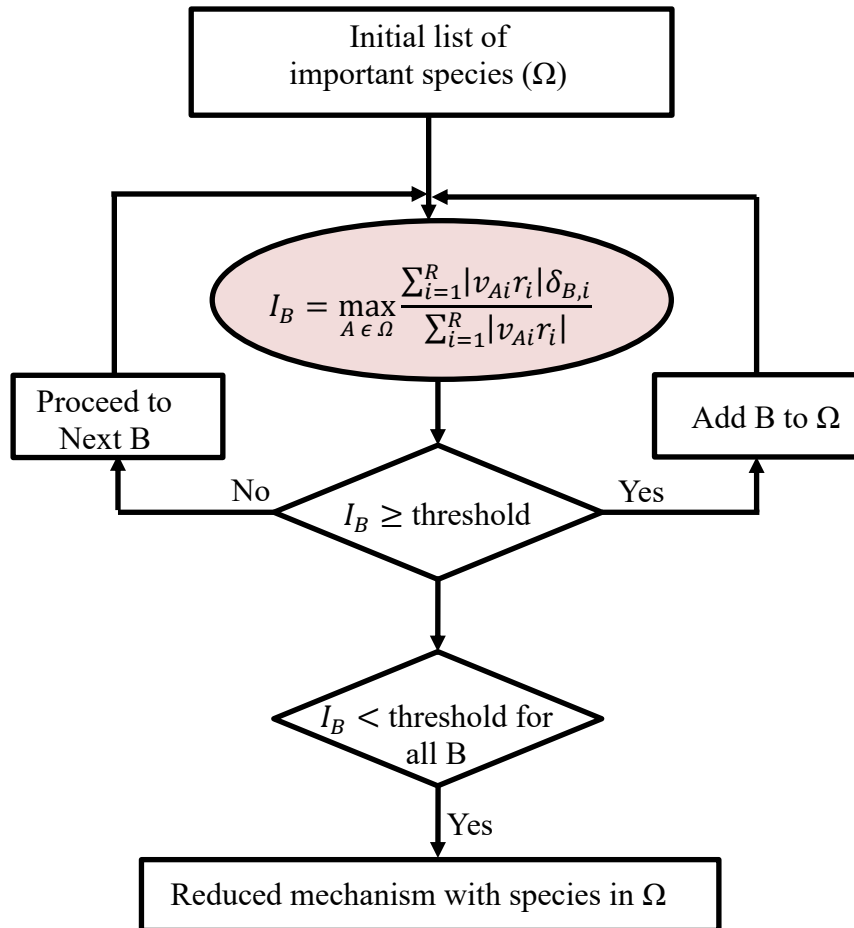
Figure 2.2: Schematic diagram of the DRG reduction procedure.

Similar to the reduction with sensitivity analysis, the DRG method is also repeatedly applied in the present work to gradually reduce the detailed mechanism. A first version of the reduced mechanism is obtained by applying the DRG method, which is then validated using ignition delay time and laminar flame speed calculations. This validated first version is then used again for another reduction step with the DRG method. This procedure is repeated until results obtained from reduced mechanism show deviations from the detailed mechanism and the experimental data. The smallest mechanism that predicts well the ignition delay times and laminar flame speeds is selected as the final version of the reduced mechanism. The reduced mechanism obtained using the DRG method is named Reduced Mechanism II (RM II) and

consists of 48 species and 297 reactions. This is a reduction degree of 40% with respect to the number of species and approximately 50% with respect to the number of reactions.

2.3.3 The Linear transformation method (lin-TM)

The lin-TM approach is a novel mechanism reduction tool developed recently at DLR Stuttgart by Methling *et al.* [58]. In this tool, a linear relationship is developed between input parameters (rate constants) and output parameters (*e.g.* ignition delay times, laminar flame speeds). This linearization allows a fast computation of sensitivity coefficients resulting in a fast mechanism reduction based on sensitivity analysis. In addition to mechanism reduction, the lin-TM tool allows for post-reduction optimization of the rate constants of the reduced reaction model. This means that the rate constants of the reduced mechanism can be optimized within a certain range to obtain an even higher agreement with the detailed mechanism and the experimental data. Figure 2.3 presents an overview of the lin-TM reduction procedure.
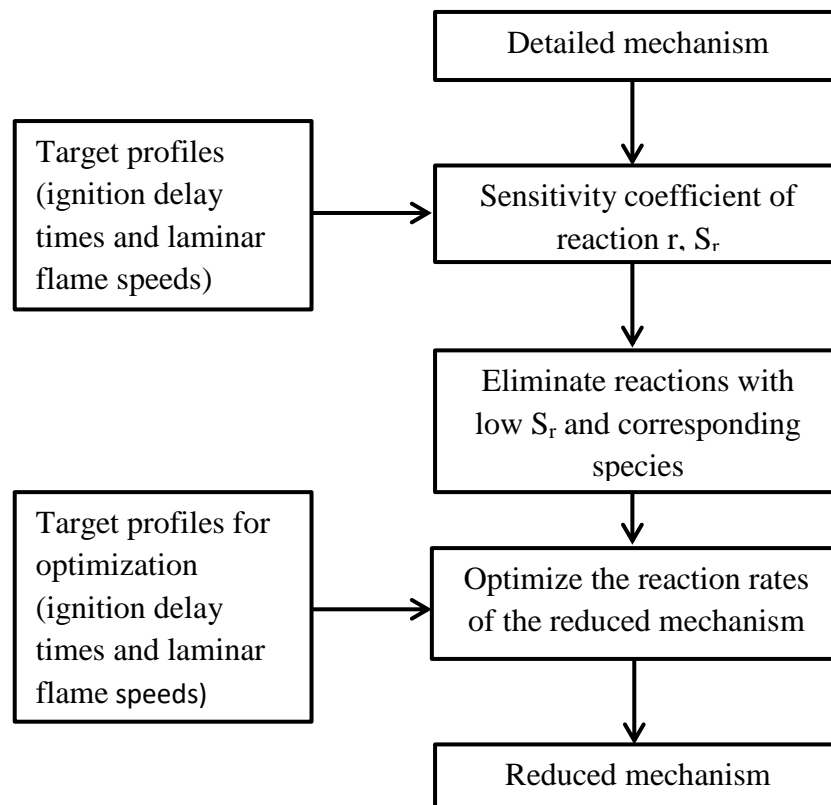
Figure 2.3 Schematic diagram of the lin-TM reduction procedure [58].

In the lin-TM reduction procedure, first, the ignition delay times and laminar flame speeds are calculated using the detailed mechanism for user given conditions. Then, the sensitivity coefficients of the reactions in the mechanism are calculated with respect to calculated ignition delay times and laminar flame speeds. Next, the mechanism is reduced by eliminating those reactions with sensitivities lower than a user given threshold. Optionally, the reduced mechanism can be optimized for user given conditions, by fine-tuning the rate constants within a certain tolerance limit as described in more details in Ref. [58].

The reduced mechanism developed in the present work using the lin-TM tool is named as Reduced Mechanism III (RMIII) and it consists of 38 species and 226 reactions. The reduction degree achieved is a reduction of 50% with respect to the number of species and a reduction of approximately 60% with respect to the number of reactions.

Table 2.3 present a comparison of the three reduced reaction mechanisms in terms of number of reactions and species as well as the reduction degree.

Table 2.3: Overview of the reduced mechanisms.

Mechanism	Species	Reactions	Reduction degree		Reduction method
			Species	Reactions	
RM I	49	328	40%	40%	Sensitivity analysis
RM II	48	297	40%	50%	Directed relation graph (DRG)
RM III	38	226	50%	60%	Sensitivity analysis using a linear transformation method

2.4 Effect of recirculation on the gas phase kinetic modeling

The high velocity of the gas flow in the REGA gasifier results in a recirculation zone [42] which brings a part of the syngas from the lower region of the reactor into the upstream combustion zone (Fig. 2.8). Therefore, in the combustion zone of the gasifier, in addition to the combustion of ethylene glycol, syngas combustion also takes place. Hence, the gas phase kinetic mechanism must also be able to describe well the combustion of syngas.

For these reasons, both the detailed and the reduced reaction mechanisms are tested in the present work against syngas combustion data. The composition of the syngas used in these computations is taken to be equal to the syngas composition at 680 mm from the injection point of the REGA gasifier, according the experimental data from the REGA gasifier as available from literature [41].
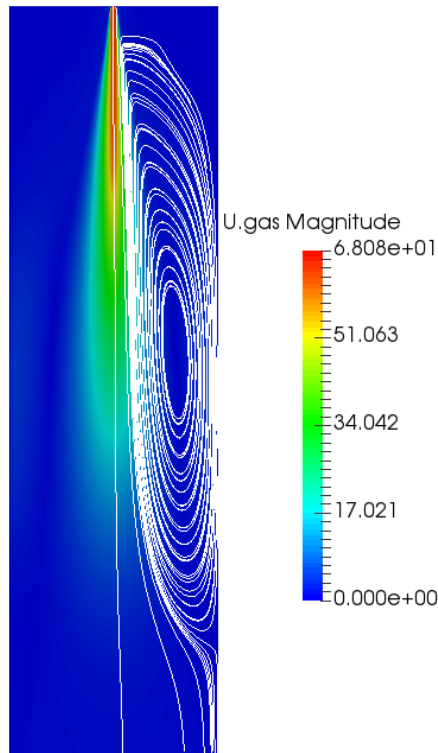
Figure 2.4: Calculated 2D recirculation of syngas in the reactor (present study).

2.5 Methodology of validation of the reaction mechanisms of EG

2.5.1 Ignition delay times

When a fuel and an oxidizer mixture are subjected to a certain pressure and temperature, spontaneous combustion may occur after a certain amount of time which depends on the initial equivalence ratio, temperature, and pressure, besides the fuel itself. This time period is called the ignition delay time [52]. Ignition delay time is a characteristic combustion property of any fuel in question. Ignition delay times for a particular fuel can be numerically computed using a suitable reaction mechanism. In the numerical calculation, ignition delay time is estimated by measuring the time for the concentration of a certain species to reach its maximum point (or maximum gradient). This is called the ignition delay time criteria and is selected based on the criteria used in the corresponding experiments. The reaction mechanism is validated by comparing the calculated ignition delay times against the published measured data for the fuel in question.

In the present work, ignition delay times are computed using the software Chemical Work Bench [60] under the assumption of no heat loss. Only one experimental data set exists for EG ignition delay times [43]. Therefore, in addition to EG, ignition delay time computations

are performed for acetaldehyde and methane as major intermediates, and also for syngas due to the reasons described in section 2.4. For the species acetaldehyde, methane, and syngas, the calculations are performed under constant pressure. In the ignition delay time calculations of ethylene glycol, an experimentally measured pressure profile [43] is used. The calculations are performed over a temperature range of 800 K to 1800 K, a pressure range of 3.5 bar to 16 bar, and an equivalence ratio range of 0.5 to 2. The conditions of ignition delay time computations are given in Table 2.4.

The results of the ignition delay time calculations in the present work are given in Chapter 5.

2.5.2 Laminar flame speeds

The second characteristic combustion property used to validate the reaction mechanisms in the present work is the laminar flame speed. The laminar flame speed is the speed of propagation of a laminar flame front into a mixture of unburnt reactants and depends on the fuel, mixture equivalence ratio, pressure, and initial temperature. In this work, laminar flame speeds are calculated using the software Cantera [61], under the assumption of a premixed flat flame. Mesh points in the calculation were refined using the "slope" and "curve" settings of the Cantera flame calculator to obtain a converged solution according to the set tolerances. The calculated flame speeds are then compared against the experimentally measured flame speed data taken from the literature. In the present work, laminar flame speeds are calculated for preheat temperatures between 298 K and 358 K, at pressures ranging between 1 and 3 bar, and equivalence ratios φ between 0.6 to 1.8. Unfortunately, until now, experimental data for laminar flame speeds of ethylene glycol are not available in literature. Therefore, the flame speeds are calculated for major intermediate species of the reaction mechanism. The conditions of the laminar flame speed calculations for each species is presented in Table 2.5.

Chapter 5 presents the results of laminar flame speed calculations.

Table 2.4: Validation targets of reaction mechanisms - Part I: Ignition delay times.

Species	Pressure (bar)	Temperature (K)	Equivalence ratio, ϕ
Acetaldehyde	3.5 – 5.0	1250 – 1800	0.5, 1.0, 2.0
Methane	3.5 – 5.0	900 – 1700	0.5
Ethylene glycol	16.0	800 – 1600	1.0
Syngas (50% CO + 50 % H_2)	4.0	950 – 1425	1.0

Table 2.5: Validation targets of reaction mechanisms - Part II: Laminar flame speeds.

Species	Pressure (bar)	Temperature (K)	Equivalence ratio, ϕ
Acetaldehyde	1	298 – 358	0.6 – 1.8
Methane	1 – 3	298	0.6 – 1.5
Ethylene glycol	1	300	0.5 – 1.7

2.5.3 Species profiles in a two-dimensional CFD simulation of the REGA gasifier

Finally, the best reaction mechanism as evaluated by the performance against ignition delay times and laminar flame speeds data is further validated using species profiles obtained in an entrained flow gasifier. The reaction mechanism is used in a two-dimensional Euler-Euler CFD simulation of the REGA. The mechanism is validated by comparing the radial species profiles of CO, H_2, CH_4, and CO_2 at two locations on the gasifier axis (at 300 mm and at 680 mm, respectively from the injection point) and comparing them to published experimental data [41], [42].

In the next chapter, the Euler-Euler CFD model for the REGA will be presented.

3. CFD model for the entrained flow gasification process

This chapter introduces the CFD model used for the numerical simulation of the entrained flow gasification process. First, the governing equations of the CFD model are presented. Then, the sub models used to model the relevant physical and chemical processes and to evaluate the source terms in the governing equations are given. The chapter ends with a discussion of the correlations used to evaluate the physical and chemical properties of the substances used in the model.

3.1 Numerical approaches for CFD simulations of the entrained flow gasification process

The entrained flow gasification process as introduced in Chapter 1 is a multiphase process which involves liquid pyrolysis oil droplets (modeled in the present work by ethylene glycol) and a gas phase entraining the liquid droplets. The liquid droplets and the gasification agent in the gas phase are injected into the entrained flow gasifier at high velocity (approx. 100 m s^{-1}) [42]. Therefore, the numerical solution results in a spray simulation with chemical reactions included for describing the fuel conversion. For CFD modeling of such multiphase flows, two approaches are available: the Euler-Euler approach and the Euler-Lagrange approach [62 – 64].

In the Euler-Euler approach, both the gas phase and the liquid droplet phase are treated as a ccontinuum [38]. The motion of each phase is described by the Navier Stokes equations. In the Euler-Lagrange approach, only the gas phase is treated as a continuum, with its motion being described by the Navier Stokes equations [65] as well. The liquid droplets are treated as individual particles, whose motion is governed by Newton's laws, based on forces acting on these particles as a result of their interaction with the gas phase [65]. As a result of the large number of calculations associated with separate droplets, the Euler-Lagrange method demands significantly more CPU time than the Euler-Euler approach [66]. In literature, spray simulations are successfully conducted using both the Euler-Euler and Euler-Lagrange approaches [66 – 69].

The aim of the present work is to develop a reduced reaction mechanism which can be used in CFD simulations successfully and efficiently, i.e. at reduced computational cost – only then, the CFD approach will be able to act as a valuable engineering optimization tool. The Euler-Euler approach is much more suited for that purpose because of its considerably lower CPU time demand compared to the Euler-Lagrange approach [66]. For this reason, in the present

work, the CFD simulations of the REGA gasifier are performed using the Euler-Euler approach.

The CFD simulation is done using the *reactingTwoPhaseEulerFoam* solver in the open source CFD tool OpenFOAM [70]. In the Euler-Euler approach, the solution procedure starts with the Navier Stokes equations, which are the conservation equations for momentum, mass and energy. For a chemically reacting system such as the entrained flow gasifier, individual mass conservation equations exist for each species present in the reaction environment. In the CFD model, the number of species conservation equations equals the number of species present in the reaction mechanism of the fuel minus one, the inert species (nitrogen). Individual species concentrations are obtained by the solution of each species mass conservation equation. The concentration of the inert species (*e.g.* N_2) is obtained by the constraint that the sum of mass fractions of gas phase species equals one. Models for relevant physical and chemical processes, here heat transfer, evaporation, radiation, and chemistry are included as source terms in the respective conservation equation. The results of the CFD simulations are validated using published experimental data from the REGA gasifier [41, 42], focusing on radial temperature profiles and radial species profiles of H_2, CO, CO_2, and CH_4 measured at two different axial locations of the gasifier. The simulation results are presented and discussed in Chapter 6.

3.2 The model geometry of the research entrained flow gasifier (REGA)

The REGA is a cylindrical entrained flow gasifier with a height of 3 m and a diameter of 0.28 m [42]. Ethylene glycol as the one component model fuel for bio-oil and the gasification agent are introduced at the top center of the gasifier (Fig. 3.1). For the model geometry, it is assumed that the flow fields within the gasifier are axisymmetric with only radial and axial variations. Therefore, a two-dimensional wedge geometry is selected for the model [71]. The model geometry considers only the first 1000 mm from the injection point. This simplification is introduced because after a certain distance from the injection point (approx. 600 mm), the gas phase compositions reach equilibrium values and no further significant axial variation can be observed in the variables. An overview of the model geometry with relevant boundaries is presented in Fig. 3.1.
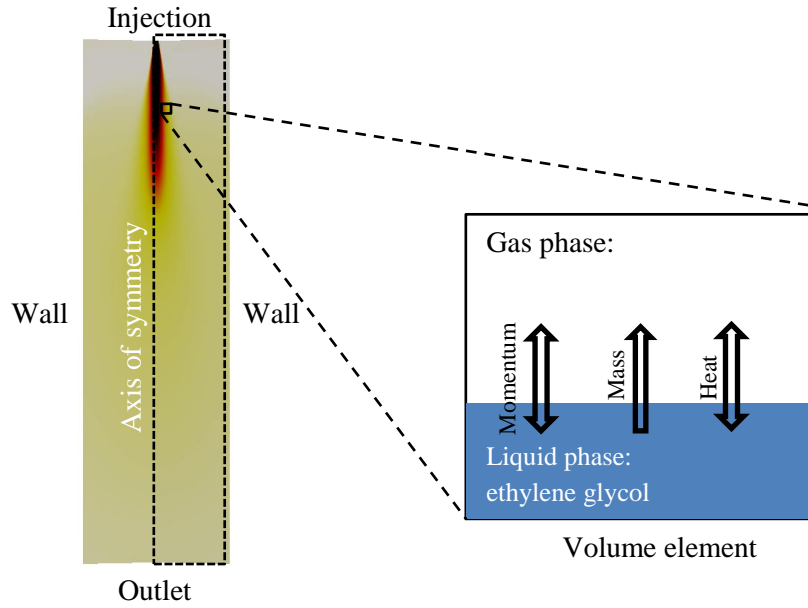
Figure 3.1: Model geometry for the REGA gasifier [42].

3.2 The governing conservation equations

The solutions for the velocity field, pressure field, temperature field, and species concentration fields are obtained in the CFD simulation by numerically solving the conservation equations for momentum, mass, and energy. For a general variable ϕ, the conservation equation takes the form given in Eq. 3.1 [72].

$$\frac{\partial(\rho\emptyset)}{\partial t} = -\nabla \cdot (\rho\emptyset U) + \nabla \cdot (\chi\nabla\emptyset) + S_\emptyset \ . \qquad\qquad Eq.\ 3.1$$

The left-hand side (LHS) of Eq. 3.1 describes the rate of accumulation of the variable within an infinitesimal control volume of the solution domain. The first term of the right-hand side (RHS) describes the net flow of the variable into the control volume as a result of convection. The second term of the RHS accounts for the net flow from the control volume due to molecular transport (*e.g.* thermal conduction in the energy equation). The final term of the RHS is the source term, which describes the rate of generation of the variable as a result of sources such as chemical reactions in the mass conservation equation.

3.3 The Euler-Euler model

The general conservation equation as given by Eq. 3.1 describes the time and the space evolution of a flow variable in a single phase system. In the Euler-Euler approach, the infinitesimal control volume is shared between two continuum phases. The fraction of volume each phase occupies in a given volume element is defined as the phase fraction of the

corresponding phase. The sum of the phase fractions equals unity. In the present work, the two continuum phases are the liquid phase consisting of ethylene glycol and the gas phase consisting of all the species to be represented in the chemical kinetic reaction mechanism (Fig. 3.1).

The motion of each phase is governed by the equations of form given by Eq. 3.1, within the volume fraction of each phase. Interactions between the two phases, such as the mass transfer due to evaporation, the heat transfer due to the temperature difference between the phases, and the drag force on liquid droplets are included as a source term in the corresponding conservation equation. The Euler-Euler conservation equations for mass, momentum, and energy of the two-phase system are presented in Eqs. 3.2 – 3.5.

Conservation of momentum

The momentum conservation equation for each phase is given by [73, 74]:

$$\frac{\partial \rho_i \varepsilon_i U_i}{\partial t} + \nabla \cdot (\varepsilon_i \rho_i U_i U_i) + \nabla \cdot (\varepsilon_i \rho_i R_i) = -\varepsilon_i \nabla p + \varepsilon_i \rho_i g + M_i \quad . \qquad Eq. 3.2$$

Here ε_i is the phase fraction of the ith phase, U_i is the average velocity of the ith phase, R_i is the turbulent and viscous stress tensor, ρ_i is the density of the ith phase, p is the pressure, g is the gravitational acceleration, and M_i describes the interphase momentum transfer.

Continuity equations

The continuity equation for each phase *i* is given by [73, 74]:

$$\frac{\partial \rho_i \varepsilon_i}{\partial t} + \nabla \cdot (\rho_i \varepsilon_i U_i) = \dot{m}_i \quad . \qquad Eq. 3.3$$

Species conservation equation

The mass balance for each species *s* in the gas phase leads to [75]:

$$\frac{\partial \varepsilon_g \rho_g Y_s}{\partial t} + \nabla \cdot (\varepsilon_g \rho_g U_g Y_s) - \nabla \cdot (\varepsilon_g \rho_g D_{i,eff} \nabla Y_s) = \dot{m}_s \quad . \qquad Eq. 3.4$$

where Y_s is the mass fraction of the species *s* in the gas phase.

The source term $\dot{m}_s$ consists of the generation and the loss of species through chemical reactions. The rate of generation of species *s* is evaluated based on the reduced chemical kinetic reaction mechanism described in Chapter 2 using the partially stirred reactor (PaSR) turbulence chemistry interaction model [76, 77]. This will be described later in section 3.4.3.

The source term also includes the evaporation rate from the liquid phase, consisting of pure ethylene glycol, to the gas phase.

Conservation of energy

The enthalpy conservation equation for each phase is solved to obtain the corresponding temperature fields [72, 75].

$$\frac{\partial \varepsilon_i \rho_i H_i}{\partial t} + \nabla \cdot (\varepsilon_i \rho_i U_i H_i) - \nabla \cdot \left(\varepsilon_i \rho_i \lambda_{i,eff} \nabla H_i\right) = \dot{h}_i \quad . \qquad\qquad Eq.\,3.5$$

The source term $\dot{h}_i$ accounts for heat generation due to chemical reactions, thermal radiation, and interphase heat transfer. The sub models used to evaluate these source terms will be discussed in section 3.4.

3.4 Models for calculating the source terms in the governing equations

The various chemical and physical processes in the gasifier are described as source terms in the conservation equations. These processes include single phase processes such as the generation or consumption of a certain species in a gas phase reaction as well as inter-phase processes such as the transfer of mass, heat, and momentum between the liquid and the gas phase. A summary of the sub-models used in the CFD simulation is presented in Table 3.1. These sub-models are described in detail in the following sections.

Table 3.1: Overview of the sub-models used in the CFD simulation.

Process	Gas phase	Liquid phase
Chemistry	EG reaction mechanism PaSR model [76, 77]	-
Evaporation	-	Spalding model [78, 79]
Interphase heat and mass transfer	Clift correlation [79, 80]	Clift correlation [79, 80]
Drag	Gidaspow drag model [81]	Gidaspow drag model [81]
Radiation	P1 model [82, 83]	-
Turbulence	RANS simulation [72] Standard k-ε turbulence model [72]	Laminar simulation

3.4.1 The radiation sub-model

Radiation heat transfer plays an important role in combustion simulations [72]. Due to the high temperatures in the flame zone (around 1800 K), a significant amount of heat transfer from the flame to the surrounding gas phase is attributed to thermal radiation. The gas phase within the entrained flow gasifier is rich with respect to carbon dioxide and water vapor, which interact with radiation.

In the present work, thermal radiation is considered in the gas phase heat transfer only while it is assumed that the liquid phase does not interact with radiation. This assumption is made because the injected liquid in the experiments consists of tiny droplets (of diameters in the order of 100 μm) which have accordingly small radiation cross sections. Also, in the simulations it was noted that the liquid phase almost completely evaporates in the first 100 mm downstream of the reactor before reaching the flame zone. Therefore it is assumed that the main mode of heat transfer to the liquid phase is through convective heat transfer from the hot gas phase surrounding the liquid droplets.

The governing equation for radiative heat transfer is given by the so-called Radiative Transfer Equation (RTE) obtained by considering the absorption, emission, and scattering of a ray of radiation as it passes through the medium (Fig. 3.2). The RTE is given by Eq. 3.6 [72].

$$\frac{dI(r,s)}{ds} = a_R I_b(r) - a_R I(r,s) - \sigma_s I(r,s) + \frac{\sigma_s}{4\pi} \int_{4\pi} I(s_i)\Phi(s_i,s)d\Omega_i \qquad . \qquad\qquad Eq.\,3.6$$

Here, s is the path length along a radiation beam. $I(r,s)$ is the intensity of radiation at position r in the direction of s. $I_b(r)$ is the emitted blackbody intensity at position r. a_R and σ_s are the absorption coefficient and the scattering coefficient, respectively of the medium. $I(s_i)$ is the incident intensity at point r from the direction s_i. $\Phi(s_i,s)$ represents the scattering phase function which gives the fraction of radiation incident on position r from the direction s_i which is then scattered in the direction s. Ω_i is the solid angle. The integral on RHS accounts for the total in-scattered radiation.

Equation Eq. 3.6 represents contributions to radiation intensity as it travels through a medium in the direction s. The terms on the RHS account for emitted intensity, absorbed intensity, as well as out-scattered and in-scattered intensity (Fig. 3.2).
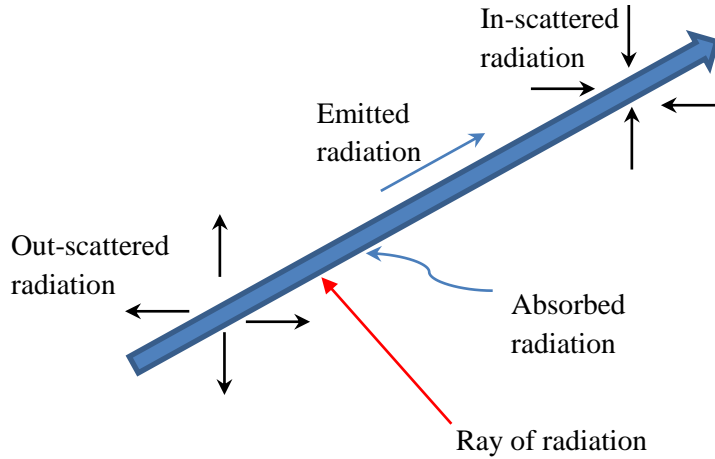
Figure 3.2: Interaction of radiation with the gas phase.

3.4.1.1 The P1-radiation model

The RTE equation given by Eq. 3.6 is an integral-differential equation which requires a special technique for its numerical solution. Commonly used solution methods include the Monte Carlo method, the discrete transfer method, the discrete ordinate method, the finite volume method, and the P-N method [72]. The P-N method converts the RTE to a set of differential equations to provide an approximate solution to the RTE. The P1 model is the lowest order P-N model [83]. The advantages of this P1-model are its low CPU time demand and a better suitability to combustion applications as compared to other radiation models [84].

In the P1-radiation model, the transport equation for the radiation intensity G, is given by [85],

$$\nabla.(\Gamma \nabla G) - a_R G + 4 a_R n^2 \sigma T^4 = S_G \quad , \qquad\qquad Eq.\,3.7$$

where

$$\Gamma = \frac{1}{3(a_R + \sigma_S) - C\sigma_S} \quad . \qquad\qquad Eq.\,3.8$$

The radiation heat flux, q_r is given by the P1-model according to:

$$q_r = -\Gamma \nabla G \quad . \qquad\qquad Eq.\,3.9$$

The source term for the energy equation S_E is given by:

$$S_E = -\nabla.q_r \quad . \qquad\qquad Eq.\,3.10$$

Combining Eq. 3.7, Eq. 3.9, and Eq. 3.10 results in Eq. 3.11, with the following expression for the radiation heat transfer source term in the energy equation,

$$S_E = a_R G - 4a_R n^2 \sigma T^4 + S_G \quad . \qquad\qquad Eq. 3.11$$

3.4.2 The turbulence model used: The Reynolds Averaged Navier Stokes Simulation (RANS)

This section presents the techniques used to model the turbulence of the flow field in the reactor. Turbulence plays an important role in the mixing of species and therefore affects the rates of chemical reactions through the so called turbulence-chemistry interaction [77]. Three main approaches of turbulence modeling can be identified; the Reynolds Averaged Navier Stokes Simulation (RANS), the Large Eddy Simulation (LES), and the Direct Numerical Simulation (DNS) [72].

In the RANS method, the instantaneous flow field is divided into a mean component and into a fluctuating component, and the Navier stokes equations are solved for the mean flow field [72]. In the LES approach, the Navier Stokes equations governing the instantaneous flow field are subjected to a spatial filtering [72] resulting in the resolution of turbulent flow structures up to a certain scale, usually of the order of the grid size of the computational mesh. The effect of turbulence of length scales which is smaller than the resolved scale is treated by using a suitable sub-grid scale (SGS) model [72]. The LES approach resolves the turbulent eddies which are larger than the SGS length scale. In the DNS method, turbulence is resolved into the finest structures using a very fine mesh. In terms of CPU time, DNS method has the highest CPU time demand. LES models require considerably larger CPU times than RANS models.

In the present work, the RANS approach is used for turbulence modeling due to its reduced computational cost.

3.4.2.1 The Reynolds Averaged Navier Stokes (RANS) approach

The RANS method separates the instantaneous flow velocity into two components [72]:

$$u = \bar{U} + u' \quad . \qquad\qquad Eq. 3.12$$

where $\bar{U}$ is the mean velocity and u' the fluctuating component.

$\bar{U}$ is given by

$$\overline{U} = \frac{1}{\Delta t}\int u\, dt \quad ,$$

<div align="right">$Eq.\,3.13$</div>

where Δt is the time scale of turbulent fluctuations.

Substituting Eq. 3.12 in the Navier Stokes equations for the instantaneous flow field results in a Navier Stokes equation for the mean flow velocity $\overline{U}$. This equation contains terms that involve the fluctuating velocity components, which are called the Reynolds stresses (Eq. 3.14) [72, 86].

$$R_{ij} = \rho\overline{u_i'u_j'} \quad .$$

<div align="right">$Eq.\,3.14$</div>

Since the fluctuating flow field is not known or solved, Reynolds stresses should be modeled using the mean flow velocity in order to close the Navier stokes equations using the mean flow. For this, the Boussinesq assumption is used [86] which relate the fluctuating components to the mean flow by using the turbulent viscosity to account for the energy dissipation in small turbulence structures.

$$-\rho\overline{u_i'u_j'} = \mu_t\left(\frac{\partial U_i}{\partial x_j} + \frac{\partial U_j}{\partial x_i}\right) - \frac{2}{3}\left(\rho k + \mu_t\frac{\partial U_k}{\partial x_k}\right)\delta_{ij} \quad .$$

<div align="right">$Eq.\,3.15$</div>

Here, μ_t is the turbulent viscosity and k is the turbulent kinetic energy. These quantities are calculated using turbulence models.

3.4.2.2 The standard k-$\boldsymbol{\varepsilon}$ model

The so-called standard k-ε model introduces two transport equations for the variables k (turbulent kinetic energy) and ε (the rate of dissipation of the turbulent kinetic energy) [72].

$$\frac{\partial(\rho k)}{\partial t} + div(\rho k U) = div\left[\frac{\mu_t}{\sigma_k}grad\,k\right] + 2\mu_t S_{ij}.S_{ij} - \rho\varepsilon \quad .$$

<div align="right">$Eq.\,3.16$</div>

$$\frac{\partial(\rho\varepsilon)}{\partial t} + div(\rho\varepsilon U) = div\left[\frac{\mu_t}{\sigma_\varepsilon}grad\,\varepsilon\right] + C_{1\varepsilon}\frac{\varepsilon}{k}2\mu_t S_{ij}.S_{ij} - C_{2\varepsilon}\rho\frac{\varepsilon^2}{k} \quad .$$

<div align="right">$Eq.\,3.17$</div>

Where,

$$C_\mu = 0.09, \qquad \sigma_k = 1.00, \qquad \sigma_\varepsilon = 1.3, \qquad C_{1\varepsilon} = 1.44, \qquad C_{2\varepsilon} = 1.92$$

are empirical constants.

The turbulent viscosity μ_t is evaluated by [72] as

$$\mu_t = \rho C_\mu \frac{k^2}{\varepsilon} \quad .$$

<div align="right">Eq. 3.18</div>

3.4.3 The turbulence chemistry interaction

Interaction between turbulence and chemistry plays an important role in combustion simulations. Flow turbulence initiates mixing of species in the reaction environment affecting the reaction rate of chemical reactions. The heat produced by chemical reactions in turn increases the fluid temperature and affects its density, thereby affecting the flow turbulence [77].

The chemical source term in the species conservation equations contains exponential terms due to the Arrhenius rate law describing the rate of chemical reactions and the products of concentrations (see Eqns. 2.2 and 2.7), making it highly non-linear. This makes is difficult to express the source term in terms of mean flow variables [77]. As a result, a suitable model for the chemical source term that considers the effect of turbulence on reaction rates is necessary. Commonly used approaches are the infinitely fast chemistry model, the Eddy dissipation concept (EDC,) and the partially stirred reactor model (PaSR) [76]. The infinitely fast chemistry approach does not take into consideration the kinetic rates of the reactions; instead, it assumes that reactions proceed with an infinitely fast reaction rate [76].

The present work uses chemical kinetic reaction mechanisms to describe the decomposition of the fuel; therefore, the infinitely fast chemistry approach is not suitable. The EDC and PaSR models both allow for finite rate kinetics while modeling the turbulence chemistry interactions. Therefore, these two models are discussed below in more detail.

3.4.3.1 The Eddy dissipation concept (EDC)

The EDC model assumes that the chemical reactions take place in fine structures within the flow where turbulent energy dissipation takes place (Fig. 3.3). These fine structures are of Kolmogorov scale, and reactants from surrounding fluid are mixed within these structures [77]. The volume fraction of the fine scales and the reaction time scale within the fine structures are evaluated based on the turbulence model parameters k and ε as given by Eqns. 3.19 and 3.21 [76, 77].
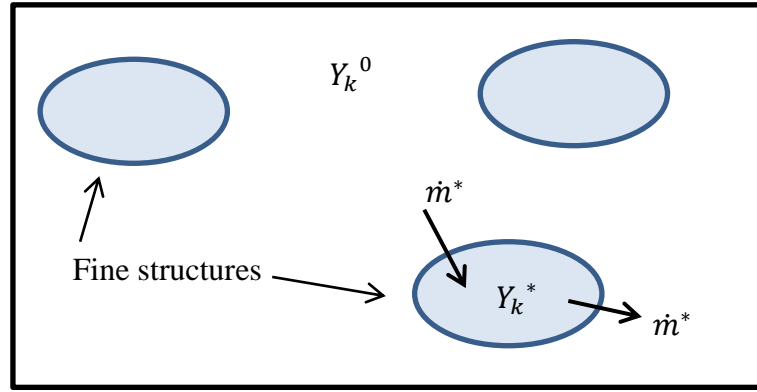
Figure 3.3: EDC model [76].

The volume fraction of the fine structures, γ^*, is calculated by [76]:

$$\gamma^* = C_\gamma \left(\frac{\nu\varepsilon}{k^2}\right)^{\frac{3}{4}} \quad . \qquad\qquad Eq.\,3.19$$

Here, C_γ is an experimentally determined emperical model constant.

The mass transfer rate between the fine structures and the surrounding gas phase is calculated using Eq. 3.20 [76].

$$\dot{m}^* = C_m \left(\frac{\varepsilon}{\nu}\right)^{\frac{1}{2}} \quad . \qquad\qquad Eq.\,3.20$$

The mass fractions of species in the fine structures, Y_k^*, are evaluated by a perfectly stirred reactor model (PSR) by using a specified chemical kinetic reaction mechanism [76]. The reaction time scale in the PSR, $\dot{\tau}^*$, is calculated using the Eq. 3.21 [76].

$$\dot{\tau}^* = \frac{1}{\dot{m}^*} \quad . \qquad\qquad Eq.\,3.21$$

The average species concentration $\tilde{Y}_k$ is calculated based on the species concentration of the fine structures and the species concentration of the surrounding gas phase:

$$\tilde{Y}_k = \gamma^* Y_k^* + (1 - \gamma^*) Y_k^0 \quad . \qquad\qquad Eq.\,3.22$$

where Y_k^0 is the concentration of the species k in the surrounding gas phase.

The mean reaction rate, $\bar{R}_k$, is finally calculated as:

$$\bar{R}_k = \frac{\bar{\rho}\gamma^*\dot{m}^*}{(1 - \gamma^*)}(Y_k^* - \tilde{Y}_k) \quad . \qquad\qquad Eq.\,3.23$$

37

3.4.3.2 The partially stirred reactor model (PaSR)

In the present work, the PaSR model is used to model the turbulence chemistry interaction.

In the PaSR model it is assumed that the reactions take place in a fraction of volume of each computational cell. The mean reaction rate, $\bar{R}_k$, is calculated by [77]:

$$\bar{R}_k = kR_k \quad , \qquad\qquad Eq.\,3.24$$

where R_k is the rate given by the chemical kinetic reaction mechanism.

The parameter k is evaluated by using two time scales, the chemical kinetic time scale (τ_{ch}) and the turbulent mixing time scale (τ_m) [76]:

$$k = \frac{\tau_{ch}}{\tau_m + \tau_{ch}} \quad . \qquad\qquad Eq.\,3.25$$

The chemical kinetic time scale is calculated based on Eq. 3.24 [76],

$$\frac{1}{\tau_{ch}} = -\frac{\partial R}{\rho\partial Y} \quad . \qquad\qquad Eq.\,3.26$$

The turbulence mixing time scale is calculated based on the k-ε model parameters [76]:

$$\tau_m = C_{mix}\sqrt{\frac{\mu_{eff}}{\rho\varepsilon}} \quad . \qquad\qquad Eq.\,3.27$$

3.4.4 Interphase heat and mass transfer models

The interphase heat and mass transfer models contribute to the temperature distributions of liquid and gas phases and also to the evaporation rate of the liquid ethylene glycol to the gas phase. Initially, no ethylene glycol is present in the gas phase of the entrained flow gasifier. The liquid EG droplets which are injected through the inlet nozzle get heated as a result of the heat transfer from the gas phase. The heated droplets evaporate into the gas phase.

The heat flux q due to the temperature difference between the liquid and gas phase is given by

$$q = K_h\Delta T \quad . \qquad\qquad Eq.\,3.28$$

where K_h is the heat transfer coefficient between the two phases.

The heat transfer coefficient K_h is evaluated using the following equation [79].

$$K_h = \frac{Nu\lambda_g}{2R} \quad .$$

Eq. 3.29

where λ_g is the thermal conductivity of the gas phase, Nu the Nusselt number, and R the droplet radius.

The Nusselt number is evaluated using the Clift correlation for the Nusselt number as given in Eq. 3.30 [79], [80]. The fractional powers arise because the correlation is obtained using dimensional analysis, where experimental data are used to determine the values of the powers that give best fit between the correlation and the experimental data.

$$Nu = 1 + (1 + RePr)^{\frac{1}{3}} \max(1, Re^{0.077}) \quad .$$

Eq. 3.30

Interphase mass transfer considers the evaporation rate of ethylene glycol, which is evaluated according to the Spalding evaporation rate [78, 79].

$$\dot{m} = 2\pi R_d D \rho_g Sh \ln(1 + B_M) \quad .$$

Eq. 3.31

where R_d is the droplet radius, D the diffusivity, Sh the Sherwood number, and B_M the mass Spalding number, the latter given by Eq. 3.32 [79].

$$B_M = \frac{Y_{v,sat} - Y_{v,\infty}}{1 - Y_{v,sat}} \quad ,$$

Eq. 3.32

with

$$Y_{v,sat} = \frac{M_v X_{v,sat}}{M_v X_{v,sat} + (1 - X_{v,sat})M_\infty} \quad .$$

Eq. 3.33

and

$$X_{v,sat} = X_l \frac{P_{sat}(T_l)}{P_\infty} \quad .$$

Eq. 3.34

where $Y_{v,\infty}$ is the mass fraction of the vapor in the gas phase, $X_{v,sat}$ the vapor saturation mole fraction, M_v the molar mass of the vapor, M_∞ the molar mass of the gas phase, X_l the mole fraction of the liquid phase, $P_{sat}(T_l)$ the saturation pressure at the liquid phase temperature T_l, and P_∞ the pressure of the gas phase.

The Sherwood number in Eq. 3.31 is evaluated using the Clift correlation for Sherwood number as given in Eq. 3.35 [79, 80].

$$Sh = 1 + (1 + Re.Sc)^{1/3} max(1, Re^{0.077}) \quad .$$

Eq. 3.35

3.4.5 The drag model

The drag model is used to evaluate the interphase momentum transfer source term in Eq. 3.2, which is given by Eqns. 3.36 and 3.37.

$$M_g = K_{lg}(U_l - U_g) \qquad . \qquad\qquad Eq. 3.36$$

$$M_l = K_{lg}(U_g - U_l) \qquad . \qquad\qquad Eq. 3.37$$

The coefficient K_{lg} is calculated using the Gidaspow drag model [81].

$$K_{lg} = \begin{cases} \dfrac{\frac{3}{4}C_D \varepsilon_g \rho_g |U_g - U_l|}{d_s} \varepsilon_g^{-2.65}, & \varepsilon_l < 0.2 \\ \dfrac{150\mu_g \varepsilon_l{}^2}{\varepsilon_g{}^2 d_l{}^2} + \dfrac{1.75\rho_g \varepsilon_l}{\varepsilon_g d_l} |U_g - U_l|, & \varepsilon_l \geq 0.2 \end{cases} \qquad . \qquad Eq. 3.38$$

The drag coefficient, C_D, is calculated by [81]:

$$C_D = \begin{cases} \dfrac{24}{Re}[1 + 0.15Re^{0.687}], & Re < 1000 \\ 0.44, & Re > 1000 \end{cases} \qquad . \qquad Eq. 3.39$$

3.5 Physical and chemical properties

The transport properties for the gas phase species are evaluated using the Sutherland transport model. The viscosity μ is calculated as a function of temperature using Sutherland's law [71]:

$$\mu = \frac{C_s\sqrt{T}}{1 + \frac{T_s}{T}} \qquad . \qquad\qquad Eq. 3.40$$

The constants C_s and T_s are given for each species s.

The effective diffusivities of the gas phase species are calculated based on the so-called Schmidt number. A Schmidt number equal to one is used making the effective diffusivity equal to the effective viscosity of the species [87]. This is justified within the present work because in turbulent combustion the turbulent mixing has a larger effect on species mixing compared to molecular diffusion.

For the liquid phase, a constant transport model, which uses a constant viscosity and Prandtl number, is used.

Molar heat capacities, enthalpy and entropy of gas phase species are calculated using Eqns. 3.41- 3.43.

$$C_p(T) = R(a_0 + a_1 T + a_2 T^2 + a_3 T^3 + a_4 T^4) \qquad . \qquad\qquad Eq.\,3.41$$

$$H(T) = a_5 R + \int_{298K}^{T} C_p(T) dT \qquad . \qquad\qquad Eq.\,3.42$$

$$S(T) = a_6 R + \int_{298K}^{T} \frac{C_p(T)}{T} dT \qquad . \qquad\qquad Eq.\,3.43$$

The coefficients $a_0 - a_6$ are obtained from databases such as NASA polynomials. Two sets of coefficients are used for two temperature ranges; low temperature region and high temperature region. Coefficients for low temperature region are given from T_{low} to T_{middle} and the coefficients for high temperature region are given from T_{middle} to T_{high}.

For the liquid phase, constant values are used for heat capacity and enthalpy.

4. Numerical solution methods of the governing equations of REGA gasification process

The mathematical model for the numerical simulation of the multiphase flow occurring within the REGA consists of coupled partial differential equations and equations describing relevant physical and chemical processes as presented in Chapter 3. In order to obtain the solution for the velocity, pressure, temperature, and species concentration fields in the reactor under the given initial and boundary conditions, the mathematical equations describing the REGA gasifier need to be solved numerically.

In the present work, the numerical solution is obtained by using the finite volume method (FVM) as implemented in the open source software OpenFOAM [70]. This chapter begins with an overview of the FVM approach. Then, the discretization of the solution domain which includes the computational mesh of the REGA gasifier is given. Next, the FVM procedure for the discretization and the solution of the governing equations is presented. Finally, the structure of the solver and case file used for the simulations of the REGA gasifier is discussed along with a summary of initial and boundary conditions and various solver settings.

4.1 The finite volume method – (FVM)

4.1.1 The discretization of the solution domain

The solution of the mathematical model described in Chapter 3 provides the steady state spatial variation of flow fields within the geometry of the gasifier. In a numerical solution, the solution of the flow fields is only obtained at discrete points within the solution domain [72]. In the finite volume method, this is called the discretization of the solution domain. The finite volume discretization is done using a computational mesh consisting of non-overlapping three dimensional cells covering the solution domain [88]. The solution is obtained at the volumetric centers of the individual cells [88]. The two dimensional mesh used in the present work consists of approximately 40,000 cells and is refined in the region of flame zone.

Figure 4.1 presents the computational mesh together with boundaries for the REGA gasifier used in the present study.
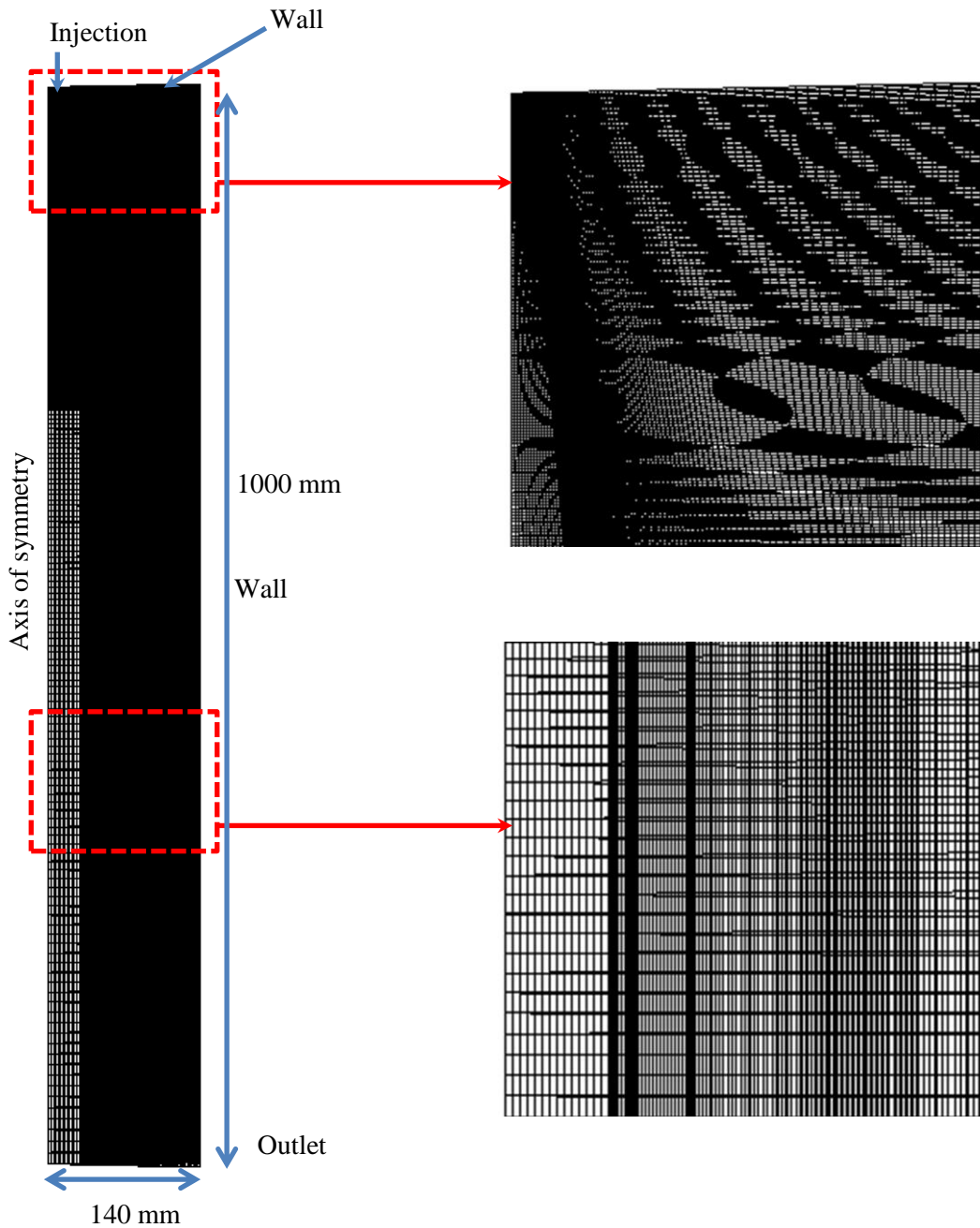
Figure 4.1: The computational mesh of the REGA as used in the present work.

4.1.2 The discretization of time

Similar to the spatial discretization, the solution is obtained at discrete time intervals starting from an initial time. The time interval is called the time step Δt. The time step Δt, the cell size Δx, and the magnitude of the velocity at the cell center $|U|$, forms the dimensionless so-called Courant number, Co [71].

$$Co = \frac{|U|\Delta t}{\Delta x} \quad .$$

<div align="right">$Eq. 4.1$</div>

In order to ensure the numerical stability of the solution, the time step Δt is selected so that the Courant number is less than one [71]. The smaller the time step, the higher the CPU time demand for the numerical calculation. In the present work, instead of a constant time step, the runtime modifiable time step feature of OpenFOAM is ultilized [71]. This feature automatically determines the time step based on a user specified maximum courant number [71].

4.1.3 The discretization of the governing equations

In the finite volume method, the partial differential equations governing the solution of the mathematical model are converted into a set of simultaneous algebraic equations using the special and temporal discretization procedure introduced earlier [72]. This is achieved by requiring that the partial differential equations should be satisfied in integral form over the discrete volume elements present in the computational mesh [88]. As introduced in section 3.2, the general transport equation for a property $\emptyset$ can be written as [72],

$$\frac{\partial(\rho\emptyset)}{\partial t} + \nabla.(\rho\emptyset U) - \nabla.(\rho\chi\nabla\emptyset) = S_\emptyset(\emptyset) \quad .$$

<div align="right">$Eq. 4.2$</div>

Integrating Eq. 4.2 over the cell volume and the time step results in,

$$\int_t^{t+\Delta t} \left[\frac{\partial}{\partial t} \int \rho\emptyset dV + \int \nabla.(\rho U\emptyset)dV - \int \nabla.(\rho\chi\nabla\emptyset) \right] dt = \int_t^{t+\Delta t} \left(\int S_\emptyset dV \right) dt \quad .$$

<div align="right">$Eq. 4.3$</div>

The integrals of Eq. 4.3 are then approximated by using cell center values and the geometrical properties of the cells. A general cell and its properties are schematically illustrated in Fig. 4.2.

In Fig. 4.2, the solution is sought at the cell center P. The volume of the cell is identified by V_p. The value of a general field $\emptyset$, at the cell center of the cell is designated by $\emptyset_P$. The solution consists of $\emptyset_P$ values for all cells in the computational domain. The cell centers of the adjacent cells are identified by N. The surface area vector S_f of the cell at whose center the solution is sought points outwards from P [88].
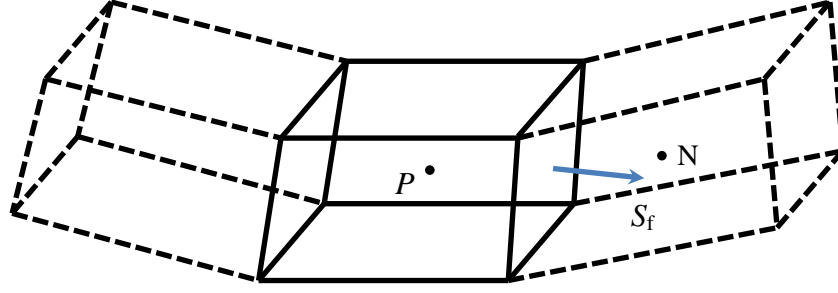
Figure 4.2: A general cell in the computational mesh.

The integral terms of the LHS in Eq.4.3 are approximated using the cell properties by using Eqns. 4.4 – 4.9 [88].

$$\int \rho\emptyset dV = \rho\emptyset_P V_P \quad .$$

Eq. 4.4

The volume integral of the second term of the LHS of Eq.4.4 is converted into a surface integral.

$$\int \nabla.(\rho\boldsymbol{U}\emptyset)dV = \int (\rho\boldsymbol{U}\emptyset).dS \quad .$$

Eq. 4.5

The surface of the computational cell is composed of a series of flat surfaces. Therefore, the surface integral in Eq. 4.5 can be written as a sum of surface integrals over individual cell faces [88] according to Eq. 4.6.

$$\int (\rho\boldsymbol{U}\emptyset).dS = \sum_f \int (\rho\boldsymbol{U}\emptyset).dS \quad ,$$

Eq. 4.6

where f denotes the cell face.

Individual face integrals are approximated by cell values:

$$\int (\rho\boldsymbol{U}\emptyset).dS = (\rho\boldsymbol{U})_f.S_f\emptyset_f \quad .$$

Eq. 4.7

where $(\rho\boldsymbol{U})_f$ is the cell face value of the mass flux and $\emptyset_f$ the one of property $\emptyset$.

The convective term of Eq. 4.3 is therefore discretized as

$$\int \nabla.(\rho\boldsymbol{U}\emptyset)dV = \sum_f (\rho\boldsymbol{U})_f.S_f\emptyset_f \quad .$$

Eq. 4.8

In a similar way, the gradient term is approximated by

$$\int \nabla \cdot (\rho \chi \nabla \emptyset) = \sum_f \rho \chi (\nabla \emptyset)_f \cdot S_f \quad . \qquad\qquad Eq.\, 4.9$$

The cell face values of the field and the gradient in Eq. 4.9 are evaluated using the cell center filed values [72]. The algorithm for computing cell face values based on cell center values of the cells is called the discretization scheme.

The RHS of the transport equation consists of the source term, which can be a general function of the field variable. The source terms are written in a linear form prior to discretization [88].

$$S_\emptyset(\emptyset) = S_u + S_p \emptyset \quad . \qquad\qquad Eq.\, 4.10$$

S_u and S_p may also depend on $\emptyset$.

The volume integral of the source term is calculated by using Eqns. 4.4 and 4.10,

$$\int S_\emptyset dV = S_u V_P + S_p \emptyset_P V_P \quad . \qquad\qquad Eq.\, 4.11$$

Combining Eqns. 4.3, 4.4, 4.8, 4.9 and 4.11, the spatially discretized form of the transport equation can be written as [88]

$$\int_t^{t+\Delta t} \left[\left(\frac{\partial \rho \emptyset}{\partial t} \right)_P V_P + \sum_f (\rho \boldsymbol{U})_f \cdot S_f \emptyset_f - \sum_f \rho \Gamma (\nabla \emptyset)_f \cdot S_f \right] dt$$

$$= \int_t^{t+\Delta t} \left(S_u V_P + S_p \emptyset_P V_P \right) dt \qquad . \qquad\qquad Eq.\, 4.12$$

The integrands of Eq. 4.12 can be totally evaluated numerically based on the cell center values and the mesh properties together with the appropriate discretization schemes.

The first term in the integrand of Eq. 4.12 contains the time derivative of the filed value $\emptyset$. The time derivative is written in terms of cell center field values using the approximation of Eq. 4.13 [88].

$$\left(\frac{\partial \rho \emptyset}{\partial t} \right)_P = \frac{\rho_P(t)\emptyset_P(t) - \rho_P(t-\Delta t)\emptyset_P(t-\Delta t)}{\Delta t} \qquad . \qquad\qquad Eq.\, 4.13$$

The unknown term is the value of the gradient at time t (LHS of Eq. 4.13). The solution at time $(t - \Delta t)$ is already known from the previous iteration or from the initial condition at the start of the solution. The gradient is evaluated using the expression at the RHS of Eq. 4.13.

The middle term of the integrand of Eq. 4.12 contains the field values at the cell faces of the computational mesh (terms involving subscript f). These values can be evaluated in two ways: By using explicit discretization or by using implicit discretization.

In the explicit discretization method, face values are evaluated from the known solution of the previous time step [88] using an appropriate discretization scheme. For example, in the central differencing discretization scheme using explicit method, the unknown face value at time t is calculated (for a uniform mesh) by using the known cell center values at time $(t - \Delta t)$ using Eq. 4.14.

$$\emptyset_f(t) = \frac{\emptyset_P(t - \Delta t) + \emptyset_N(t - \Delta t)}{2} \qquad . \qquad\qquad Eq. 4.14$$

Using the explicit method, Eqns. 4.12 – 4.14 can be combined to directly calculate the current value of the field at each cell center.

In the implicit method, the face values are evaluated based on the unknown field values at time t, as in Eq. 4.15.

$$\emptyset_f(t) = \frac{\emptyset_P(t) + \emptyset_N(t)}{2} \qquad . \qquad\qquad Eq. 4.15$$

Since the face values then depend also on the present field values of the neighboring cells (denoted by subscript N), the implicit method results in an algebraic equation for each cell, of the form as given in Eq. 4.16 [88].

$$a_P \emptyset_P(t) + \sum_N a_N \emptyset_N(t) = S_P \qquad . \qquad\qquad Eq. 4.16$$

When written for every cell in the computational mesh, Eq. 4.16 yields a system of algebraic equations of the form:

$$A\emptyset = S \qquad . \qquad\qquad Eq. 4.17$$

where matrix A consists of coefficients a_P as diagonal entries, and coefficients a_N as off diagonal entries. $\emptyset$ is the vector consisting of cell center values of the field for all cells in the mesh and S is the source term vector.

The system of algebraic equations as given by Eq. 4.17 is then numerically solved to obtain the unknown fields (species concentrations, temperature, velocity, pressure etc.) for the given time step; the solution is proceeded in time until the end time of the simulation is reached.

4.2 The pressure-velocity coupling

The numerical solution of the momentum conservation equation (Eq. 3.2) introduces some difficulties due to the nonlinearity of the convective term and the absence of an explicit equation for pressure [72].

The single phase incompressible form of the momentum conservation equations takes the form [88]:

$$\nabla \cdot U = 0 \qquad . \qquad\qquad Eq.\,4.18$$

$$\frac{\partial U}{\partial t} + \nabla \cdot (UU) - \nabla \cdot (\nu U) = -\nabla p \qquad . \qquad\qquad Eq.\,4.19$$

The momentum equation is discretized using the procedure described in the section 4.1.3 to obtain Eqns. 4.20 - 4.24 [88]:

$$a_P U_P = H - \nabla p \qquad , \qquad\qquad Eq.\,4.20$$

where

$$H = -\sum_N a_N U_N + \frac{U^0}{\Delta t} \qquad . $$

Then, U_P is given by:

$$U_P = \frac{H}{a_P} - \frac{1}{a_P}\nabla p \qquad . \qquad\qquad Eq.\,4.21$$

The interpolated form of Eq. 4.21 gives the velocities on the cell faces:

$$U_f = \left(\frac{H}{a_P}\right)_f - \left(\frac{1}{a_P}\nabla p\right)_f \qquad . \qquad\qquad Eq.\,4.22$$

An equation for pressure is obtained by substituting U_P in the continuity equation (Eq.4.18).

$$\nabla \cdot \left(\frac{1}{a_P}\nabla p\right) = \sum_f S_f \cdot \left(\frac{H}{a_P}\right)_f \qquad . \qquad\qquad Eq.\,4.23$$

The face flux F, is given by:

$$F = S_f \cdot U_f \qquad . \qquad\qquad Eq.\,4.24$$

The correct solution of both the pressure and the velocity field should satisfy simultaneously both the continuity equation and the momentum equation (Eqns. 4.18 and 4.19). These

solutions are found by iteratively solving the discretized Eqns. 4.20 - 4.23. The main algorithms used for the iterative solution are the PISO [89] and the SIMPLE algorithm [90]. The PISO algorithm is applied to transient simulations while the SIMPLE algorithm is used for steady state flows where the nonlinearity of convective term of the momentum equation is more important. The PIMPLE algorithm which is a combination of the PISO and SIMPLE algorithms is used in the present work.

4.2.1 The PISO algorithm

The PISO algorithm is used to solve the discretized Eqns. 4.20 - 4.23 in transient simulations. The algorithm proceeds through the following four steps [88].

1. Momentum predictor: Eq. 4.20 is solved using the pressure field from the previous time step, giving an approximate solution for the new velocity field.

2. Pressure solution: Predicted velocities in step 1 are used to evaluate H and solve the pressure equation Eq. 4.23 to obtain the new pressure field.

3. Explicit velocity correction: The velocity field is corrected based on the new pressure field using Eq. 4.21.

4. Based on the corrected velocities, the H field is updated, the new pressure equation is solved, and the procedure is repeated from step 3 until a selected set tolerance (difference between the present solution and the previous solution) for the convergence is reached.

4.2.2 The SIMPLE algorithm

The SIMPLE algorithm is used for the pressure velocity solution in steady state problems [88]. It consists of 5 specific steps as follows [91]:

1. An approximate velocity field is calculated by solving the momentum equation using the pressure field of the previous iteration.

2. Using the approximate velocity field, the mass fluxes at the cell faces are computed. These mass fluxes are not conservative because the velocity field is only approximate.

3. The pressure equation is solved to obtain a new pressure field; pressure under relaxation is applied (Eq.4.26). In pressure under relaxation, the pressure solution is modified according to Eq. 4.26 to improve the numerical stability of the solution.

4. The velocity field and the mass fluxes are corrected based on the new pressure field.

5. Procedure is repeated from step 1 until finally convergence is reached.

The pressure under relaxation is performed according to Eq. 4.26 [88]:

$$p^{new} = p^{old} + \alpha_p(p^p - p^{old}) \qquad . \qquad\qquad Eq. 4.26$$

where p^{new} is the new pressure field to be used in the momentum predictor step; p^{old} is the pressure field used in the previous momentum predictor, p^p is the pressure solution and α_p is the user specified pressure under relaxation factor. α_p varies between 0 and 1.
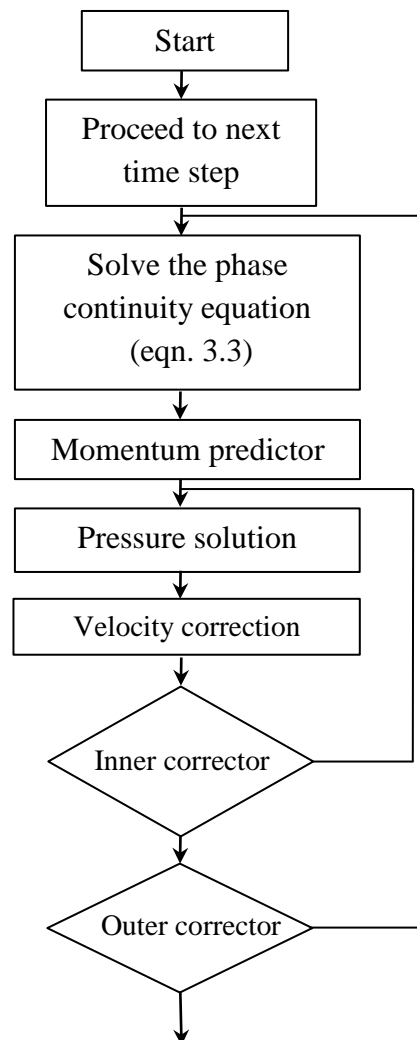
Figure 4.3: The PIMPLE solution algorithm – schematic illustration.

4.2.3 The PIMPLE algorithm

The PIMPLE algorithm [92] is a combination of the PISO and SIMPLE algorithms and is used in the OpenFOAM solver in the present work to solve the pressure and velocity fields. In the PIMPLE algorithm, SIMPLE stages (outer correctors) are applied over a given number of PISO stages (inner correctors) until convergence is reached for each time step. Then, the procedure is repeated with the next time step. If the number of outer correctors is set to 1, the algorithm acts as the PISO algorithm [92]. A schematic of the PIMPLE solution procedure is presented in Fig. 4.3 [93]. Same algorithms are applied in the two phase case, where they are applied to each phase separately.

4.3 The CFD simulation of the REGA gasifier

The present work uses the open source CFD tool OpenFOAM [70] to perform the CFD simulations of the REGA gasifier. The CFD solver used is called the *reactingTwoPhaseEulerFoam*. The *reactingTwoPhaseEulerFoam* solver of the OpenFOAM package is a two-phase solver for modeling reacting flows using the Euler-Euler approach. The governing mathematical equations of the solver are the ones presented in Chapter 3. The numerical solution techniques and algorithms used by the solver are discussed in the present chapter.

The CFD mesh is generated using the mesh generation utility *blockMesh* of the OpenFOAM package. Instructions for the mesh generation as well as the instructions for the solver (*e.g.* selection of sub models, discretization schemes and of time step, simulation times) are provided in a case file. The file structure of the OpenFOAM case file to run simulations is illustrated in Fig. 4.4.

Simulations were performed using parallel computing with 20 cores at 2.5 GHz. The approximate time for the solution to reach the steady state was 60 days using the detailed mechanism and 12 days using the reduced mechanism II. The reduced mechanism II is selected for CFD simulations based on the comparison of performances of the three reduced mechanisms in terms of accuracy. This is presented in detail in chapter 5 (Tables 5.1 and 5.2).

```
REGA Simulation
    ├── 0  ─ Consists of initial and boundary
    │         conditions for solved variables
    ├── constant
    │      ├── Polymesh ─ Consists of instructions for mesh generation
    │      ├── chemistryProperties – instructions for the chemistry solver
    │      ├── combustionProperties – combustion model and numerical constants
    │      ├── phaseProperties – settings for phase sub models (e.g. drag model)
    │      ├── radiationProperties – numerical constants for radiation model
    │      ├── thermophysicalProperties – transport model, equations of state,
    │      │                                thermodynamics specification.
    │      ├── turbulenceProperties – settings for RANS k-e turbulence model
    │      ├── thermo – thermodynamic data file
    │      └── reactions – chemical kinetic reaction mechanism
    └── system
           ├── controlDict – general solver settings, start time, end time,
           │                    write interval etc.
           ├── decomposeParDict – settings for parallel computing
           ├── fvSchemes – Schemes for finite volume discretization
           └── fvSolution – Algebraic solvers and PIMPLE settings
```

Figure 4.4: The structure of the OpenFOAM case setup.

4.3.1 Initial and boundary conditions

The initial and boundary conditions of the CFD simulation are set according to the experimental conditions of the REGA gasifier [41, 42]. In the experiments, ethylene glycol, oxygen, and air are injected from the top center of the REGA gasifier at two different inlet fuel/air equivalence ratios, 2.12 and 1.67, respectively. In the experiment, the reactor walls are heated using electrical heating. The reactor is operated at atmospheric pressure [41, 42]. The

initial conditions of the fields at the start of the simulations and boundary conditions used in the present work corresponding to these experimental conditions are listed in Tables 4.1 and 4.2.

Table 4.1: Initial and boundary conditions for the experimental setup at $\phi = 2.12$.

	Velocity / $m\ s^{-1}$	Pressure / atm	Temperature / K	Species mass fraction
Inlet	67	$P_{in} = 1$	$T_{in,g,l} = 300$	$O_2 = 0.721$ $N_2 = 0.279$ $EG_{liquid} = 1$
Wall	No slip condition	Zero gradient	Zero gradient	Zero gradient
Outlet	Zero gradient	Zero gradient	Zero gradient	Zero gradient
Initial condition	(0,0,0)	1	$T_g = 1473$ $T_l = 300$	$O_2 = 0$ $N_2 = 0.15$ $H_2 = 0.02$ $CO = 0.34$ $CO_2 = 0.25$ $H_2O = 0.24$

Table 4.2: Initial and boundary conditions for the experimental setup at $\phi = 1.67$.

	Velocity / $m\ s^{-1}$	Pressure / atm	Temperature / K	Species mass fraction
Inlet	125	$P_{in} = 1$	$T_{in,g,l} = 300$	$O_2 = 0.516$ $N_2 = 0.484$ $EG_{liquid} = 1$
Wall	No slip condition	Zero gradient	Zero gradient	Zero gradient
Outlet	Zero gradient	Zero gradient	Zero gradient	Zero gradient
Initial condition	(0,0,0)	1	$T_g = 1473$ $T_l = 300$	$O_2 = 0$ $N_2 = 0.25$ $H_2 = 0.015$ $CO = 0.25$ $CO_2 = 0.245$ $H_2O = 0.24$

4.4 The parameter study of the REGA

The composition of the syngas produced in a gasification process varies with the operating conditions of the gasifier. One of the aims of the present work is to study the effect of the operating conditions of the REGA gasifier on the output composition of the syngas using numerical simulations. The reduced CPU time of the present CFD model as a result of using a reduced chemical kinetic reaction mechanism and the Euler-Euler approach allows

53

conducting a parameter study of the REGA gasifier. In the parameter study, three parameters are varied: the pressure, the fuel preheat temperature, and the equivalence ratio. The resulting final syngas composition is studied by performing a series of CFD simulations. The summary of the calculations of the parameter study and the ranges of the variation of parameters are presented in Table 4.3.

Table 4.3: Summary of the simulations of the parameter study of the REGA gasifier.

Simulation number	Fuel preheat temperature (K)	Operating pressure (atm)	Equivalence ratio ϕ
Temperature			
1	300	1	2.12
2	325	1	2.12
3	350	1	2.12
4	375	1	2.12
5	400	1	2.12
6	425	1	2.12
Pressure			
1	300	1	2.12
7	300	2	2.12
8	300	3	2.12
9	300	4	2.12
10	300	5	2.12
Equivalence ratio			
11	300	1	1.50
12	300	1	1.67
13	300	1	1.80
14	300	1	2.00
1	300	1	2.12

5. Results and Discussion

This chapter presents the results of the validation of the reduced mechanisms by use of experimental data taken from literature as well as comparison with calculations using the detailed mechanism. Three reduced mechanisms developed by using three different reduction methods as presented in Chapter 2 are validated and the most accurate reduced model is further validated using CFD simulations. This chapter presents: (i) Computations of two fundamental combustion properties, ignition delay times and laminar flame speeds of ethylene glycol and of major intermediates within the oxidation of ethylene glycol, (ii) the two-dimensional CFD simulations of REGA, and (iii) the results of the parameter study of the REGA.

The chapter consists of three main sections. The first section presents the validation results of the detailed and reduced reaction mechanisms for ethylene glycol oxidation. As given in Chapter 2, the reduced mechanisms in the present work are developed by applying three different reduction techniques to the detailed reaction mechanism. A summary of the number of species and reactions of the developed reduced mechanisms are given in Table 2.3. The reaction mechanisms are validated by calculating ignition delay times and laminar flame speeds for the conditions presented in Tables 2.4 and 2.5 in Chapter 2 and by comparing them with published experimental data.

In the next section, results of the CFD simulations are presented. For the two-dimensional CFD simulations of the REGA, the best reduced mechanism, in terms of the agreement with the detailed mechanism and experimental data, is selected for further validation with respect to ethylene glycol entrained flow gasification experiments in the REGA. The results of the CFD simulations using the detailed and reduced mechanisms are presented. Simulation results are compared against the published experimental data for radial species profiles and temperature profiles from the REGA [41, 42].

Finally, the validated reduced mechanism is used to perform a parameter study of REGA to investigate the effect of fuel preheat temperature, operating pressure, and equivalence ratio on syngas produced, and the results are presented.

5.1 Reaction pathway analysis of ethylene glycol decomposition

Figure 5.1 presents the reaction pathway diagram of ethylene glycol conversion under the typical gasification conditions of REGA ($T = 1500$ K, $p = 1$ atm, $\phi = 2$). The reaction pathway

diagram is obtained using the detailed mechanism and is constructed using the software tool chemical work bench [60].
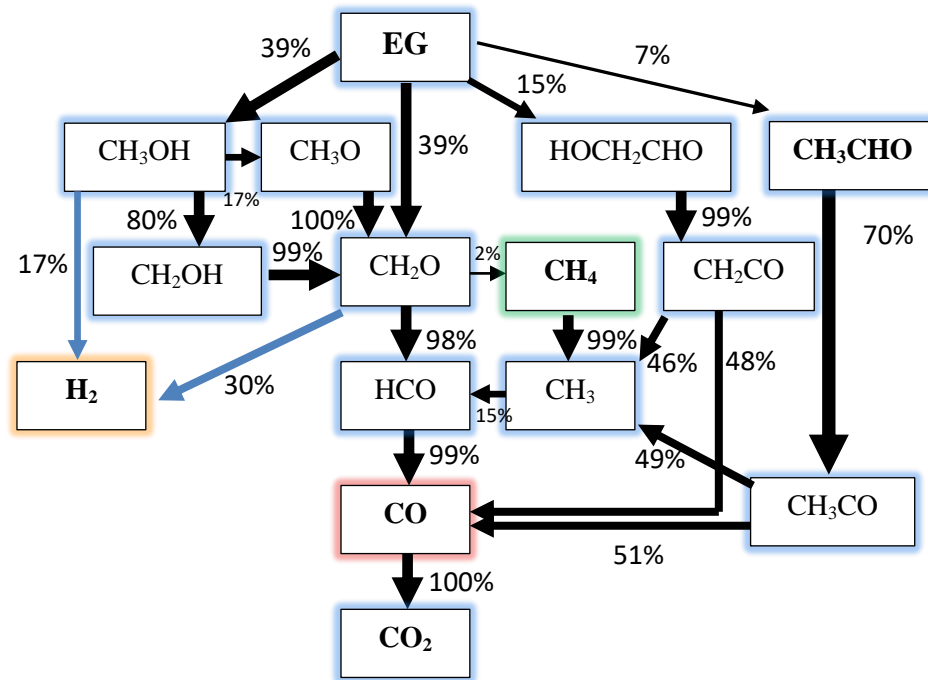

Figure 5.1: Reaction pathway diagram for the pyrolysis of EG at $\phi = 2,\ T = 1500\ K,$ and $p = 1\ bar$. Black arrows: C atom flux, Blue arrows: H atom flux.

According to Fig. 5.1, a major decomposition pathway of EG, to methanol and to formaldehyde, can be identified:

$$OHCH2CH2OH \rightleftharpoons CH_3OH + CH_2O \qquad\qquad R5.1$$

This reaction accounts for about 80% of the decomposition of ethylene glycol under the investigated conditions. The remaining 20% converts to acetaldehyde and $HOCH_2CHO$.

Methane is produced through methyl radical reactions with formaldehyde ($R5.2$).

$$CH_2O + CH_3 \rightleftharpoons HCO + CH_4 \qquad\qquad R5.2$$

In the major path, formaldehyde is converted to HCO through reactions $R5.3$ and $R5.4$, which further reacts to produce CO and subsequently CO_2:

$$CH_2O + H \rightleftharpoons HCO + H_2 \qquad\qquad R5.3$$

$$CH_2O + OH \rightleftharpoons HCO + H_2O \qquad\qquad R5.4$$
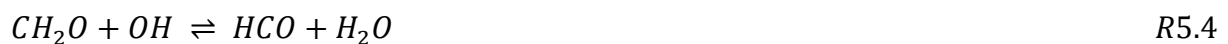
According to the reaction pathway diagram, acetaldehyde, methane and syngas (mixture of hydrogen and carbon monoxide) are formed as stable intermediates within the EG decomposition. In addition to ethylene glycol, these species are used for the validation of the reduced reaction mechanisms.

5.2 Validation of the reaction mechanisms – Ignition delay times

The results of the ignition delay time (IDT) computations for three different species, ethylene glycol, acetaldehyde, and methane, as well as for syngas (50% CO and 50% H_2) are presented in Figs. 5.2 - 5.12.

*Ethylene glycol ignition delay time*s. Figure 5.2 presents the ignition delay times of ethylene glycol, calculated using the detailed mechanism and three reduced mechanisms. The results are compared against experimental data taken from [43].
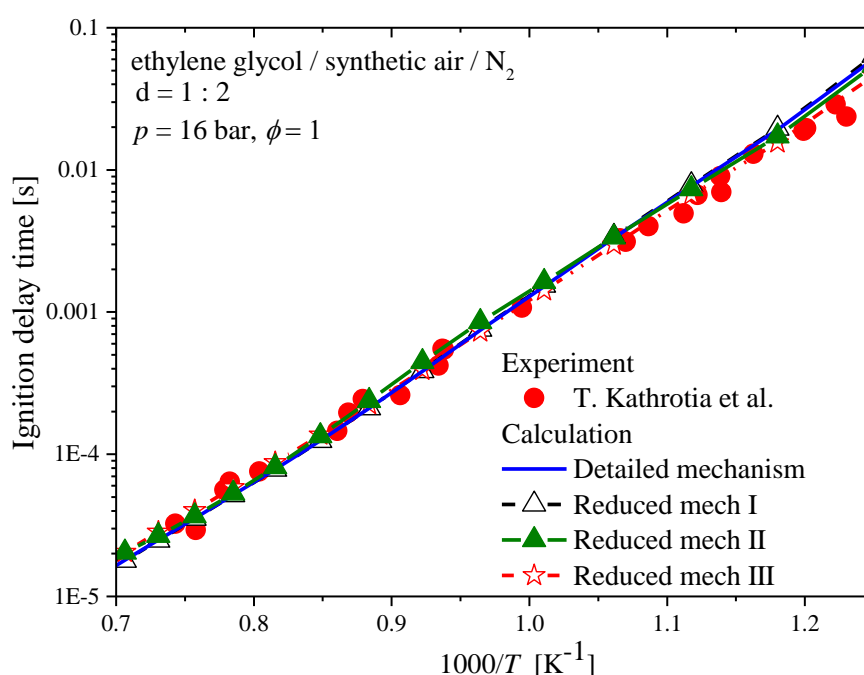

Figure 5.2: Calculated (lines; reduced mechanisms, this work) and experimental (symbols; Kathrotia et al. [43]) ignition delay times of ethylene glycol/air mixtures: $p = 16$ bar, $\phi = 1$.

Computations are performed over a temperature range of 800 K to 1400 K, at an elevated pressure of 16 bar, and at stoichiometric conditions with a 1:2 dilution in N_2. The detailed mechanism shows excellent agreement with the experimental data over the whole temperature range, except a very slight over prediction in the low temperature region. All three reduced mechanisms show very good agreement with both the detailed mechanism and the

57

experimental data for temperatures ranging from 800 K to 1400 K. For temperatures above 1100 K, the predicted IDTs of three reduced mechanisms almost coincide. This is because the reduction procedure is focused on high temperature target conditions which are important in REGA simulations. For temperatures below 1100 K, the three reduced mechanisms slightly deviate among each other, while still showing a very good performance.

*Acetaldehyde ignition delay time*s. Figures 5.3 - 5.6 present the comparison between measured and calculated ignition delay times of acetaldehyde, a stable decomposition product within the conversion of ethylene glycol (see Fig. 5.1), at a pressure of 3.5 bar for fuel lean and fuel rich equivalence ratios.

For the fuel lean regime at $\phi = 0.5$ (Figs. 5.3 and 5.4), the ignition delay times of acetaldehyde calculated by using the detailed reaction mechanism (Fig. 5.3) and the three reduced models (Fig. 5.4) show a good agreement with the experimental data only in the high temperature region, for T > 1500 K . In the lower temperature region, i.e. T<1500 K, all mechanisms show a similar deviation with respect to the experimentally measured data. The simulations overpredict the measured IDT. The maximum over prediction with experimental data is about 4 ms.

Figs. 5.5 and 5.6 present the acetaldehyde IDT in the fuel rich region for $\phi = 2$. Considerable deviations can be observed in the low temperature region (T < 1600 K) between the computed and the experimental values. Again, the reduced mechanism II shows the best agreement with the detailed mechanism.

These deviations from the experimental data in acetaldehyde computations can be explained with respect to the base reaction mechanism. This base mechanism is a high temperature ethylene glycol oxidation mechanism, which needs not to have a complete acetaldehyde sub mechanism. Therefore, disagreements between experimental and computational data can be expected. The reduced mechanisms show good agreement with the detailed mechanism with respect to acetaldehyde calculations. Reduced mechanism II, developed using the DRG method shows the best agreement with the detailed mechanism. This is because the DRG method operates by identifying couplings between species within ethylene glycol mechanism. In the rate of production diagram (Fig. 5.1) it can be seen that acetaldehyde is strongly coupled to ethylene glycol and hence the DRG method preserves the acetaldehyde submechanism, showing better agreement with the detailed mechanism as compared to other

two methods. The reduced mechanisms I and III are both based on sensitivity analysis and show similar performance with respect to acetaldehyde IDT.
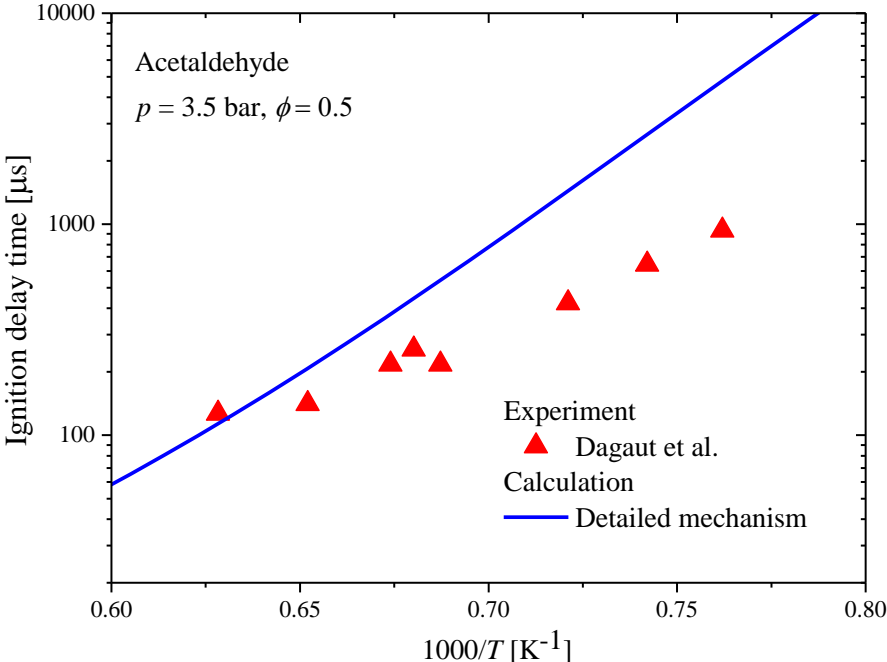

Figure 5.3: Calculated (line; detailed mechanism, Kathrotia et al. [43]) and experimental (symbols; Dagaut et al. [95]) ignition delay times of acetaldehyde/air mixtures: $p = 3.5$ bar, $\phi = 0.5$.
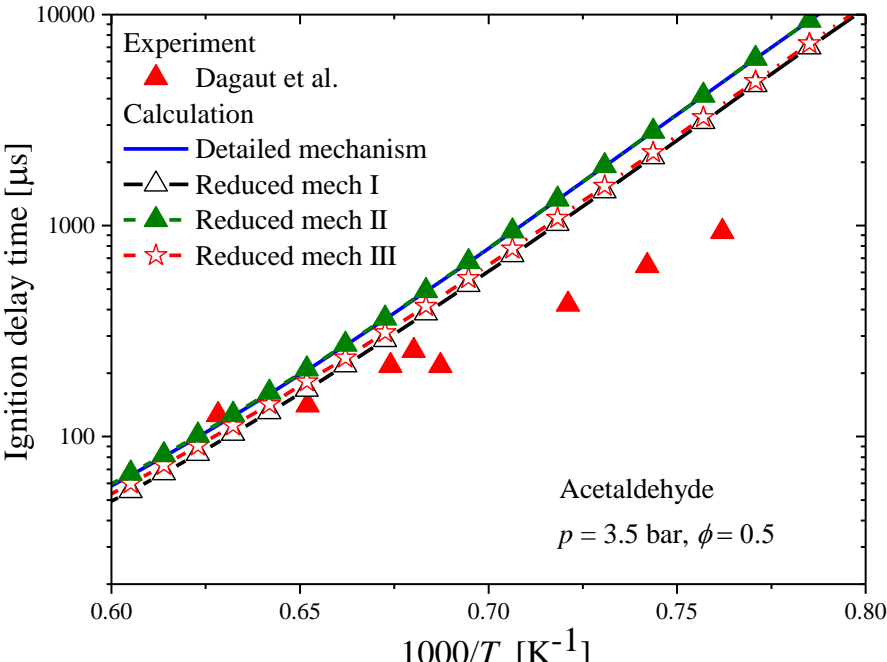
Figure 5.4: Calculated (lines; this work) and experimental (symbols; Dagaut et al. [95]) ignition delay times of acetaldehyde/air mixtures: $p = 3.5$ bar, $\phi = 0.5$.
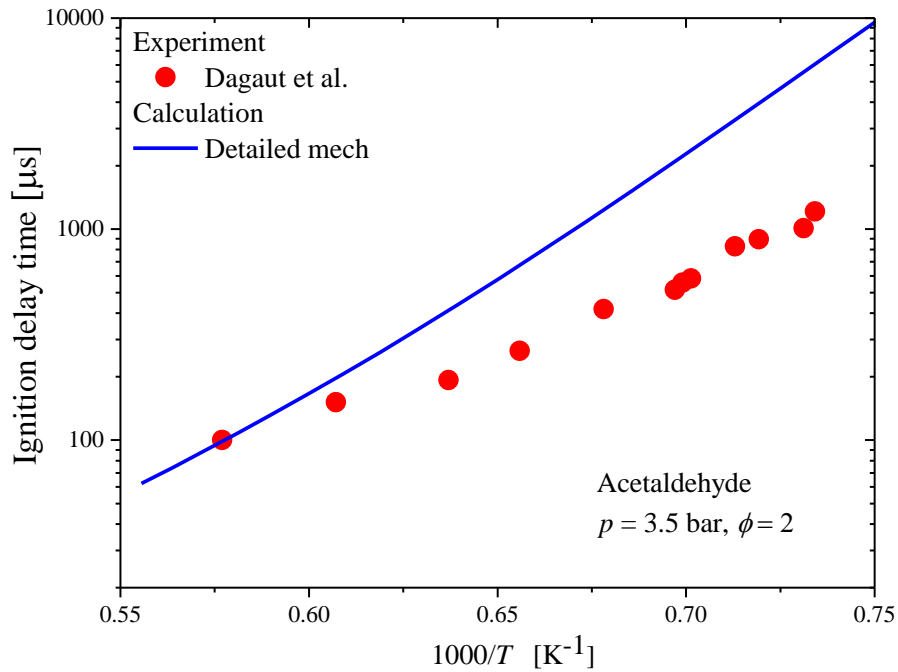
Figure 5.5: Calculated (lines; detailed mechanism, Kathrotia et al. [43]) and experimental (symbols; Dagaut et al. [95]) ignition delay times of acetaldehyde/air mixtures: $p = 3.5$ bar, $\phi = 2$.
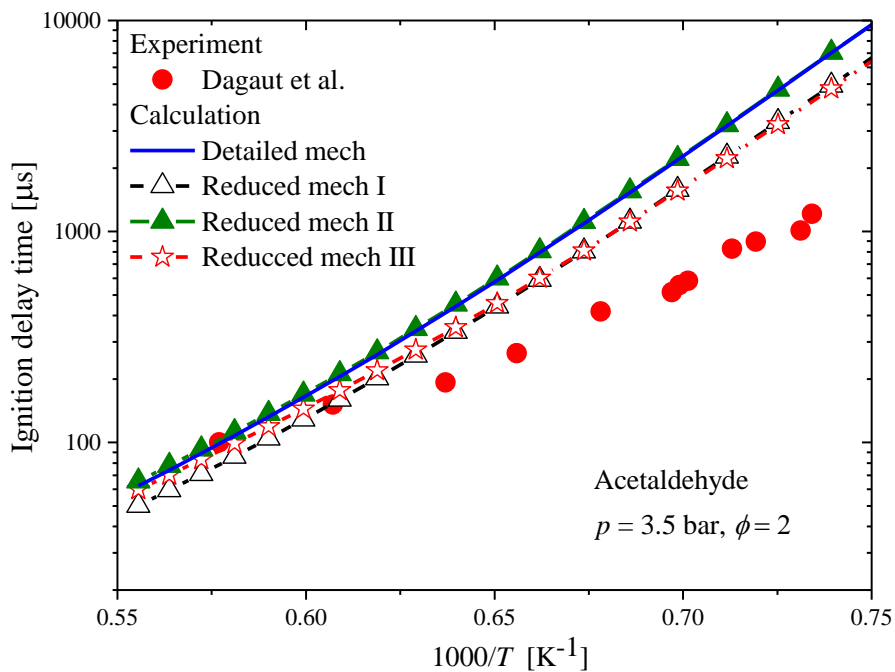

Figure 5.6: Calculated (lines; this work) and experimental (symbols; Dagaut et al. [95]) ignition delay times of acetaldehyde/air mixtures: $p = 3.5$ bar, $\phi = 2$.

Methane ignition delay times. In Figs. 5.7 - 5.10, the performances of the mechanisms are investigated with respect to methane ignition delay times. The IDTs are computed in the temperature range of 1515 K to 1725 K, a pressure of 3.5 bar and for an equivalence ratio of 0.5. According to the ROP analysis, see Fig. 5.1, methane is a further stable intermediate within the decomposition of ethylene glycol. However, in the entrained flow gasification experiments and hence also in simulations, methane is observed in very low concentrations (less than 1 vol %). In Figs. 5.7 and 5.8, the detailed mechanism and the reduced mechanisms I and II show little deviation among each other, these mechanisms over predict the methane ignition delay times with a highest deviation about 80 µs, in the investigated temperature range. The reduced mechanism III shows good agreement with the experimental data while deviating from the detailed mechanism. This is due to the post reduction optimization performed with the lin-TM reduction tool, where the reduced mechanism III is optimized with respect to atmospheric methane IDTs. The optimization procedure changes the rate constants of the reactions of the reduced mechanism III from the corresponding rate constants of the detailed mechanism. Also, the reduced mechanism III has a significantly lower number of species and reactions as compared to the other two reduced mechanisms (Table 5.1). Therefore, deviations between reduced mechanism III and the detailed mechanism can be expected.
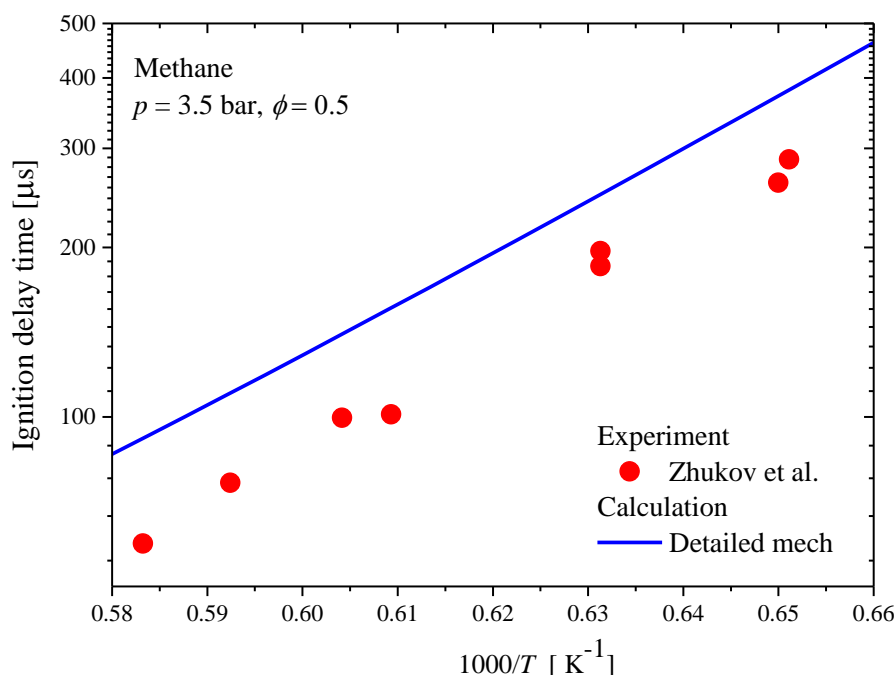

Figure 5.7: Calculated (lines; detailed mechanism, Kathrotia et al. [43]) and experimental (symbols; Zhukov et al. [96]) ignition delay times of acetaldehyde/air mixtures: $p = 3.5$ bar, $\phi = 0.5$.
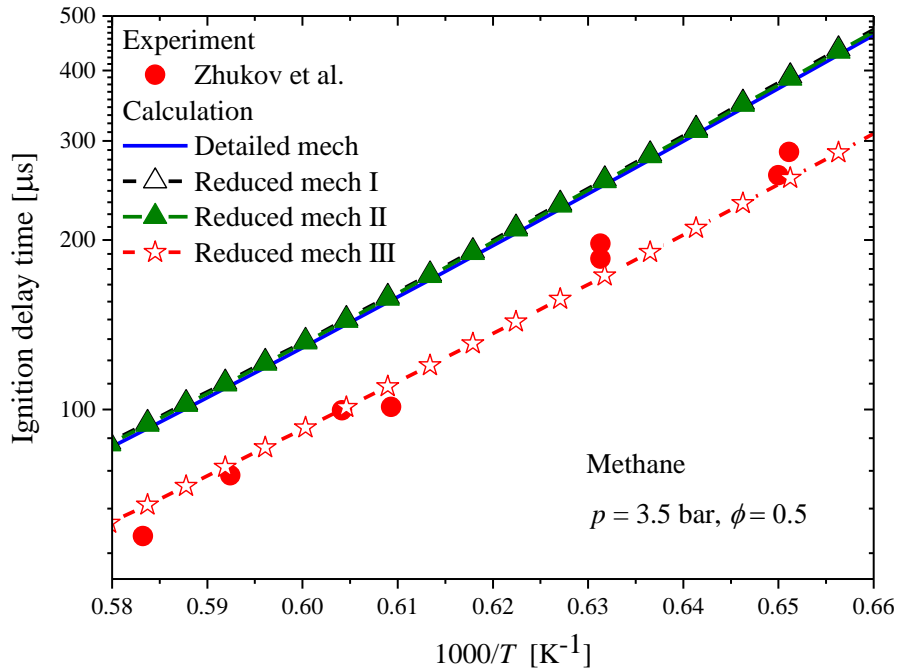
Figure 5.8: Calculated (lines; this work) and experimental (symbols; Zhukov et al. [96]) ignition delay times of methane/air mixtures: $p = 3.5$ bar, $\phi = 0.5$.
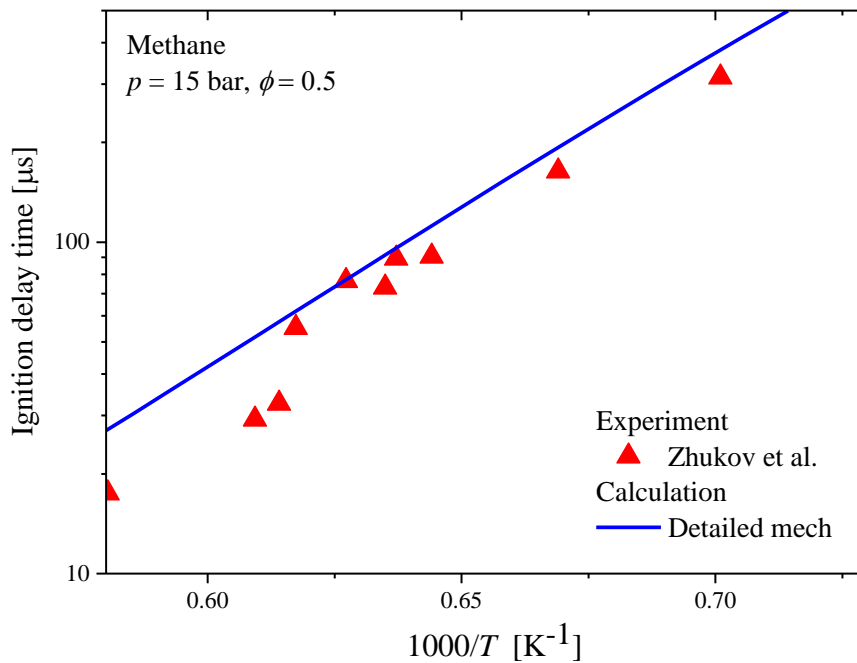
Figure 5.9: Calculated (lines; detailed mechanism, Kathrotia et al. [43]) and experimental (symbols; Zhukov et al. [96]) ignition delay times of methane/air mixtures: $p = 15$ bar, $\phi = 0.5$.

In Figs. 5.9 and 5.10, methane ignition delay times for a pressure of 15 bar are presented. At this condition, all reaction mechanisms show good agreement with the experimental methane ignition delay times. The reduced mechanisms I and II show good agreement with the detailed

mechanism, while the reduced mechanism III deviates from the detailed mechanism due to reasons mentioned earlier.
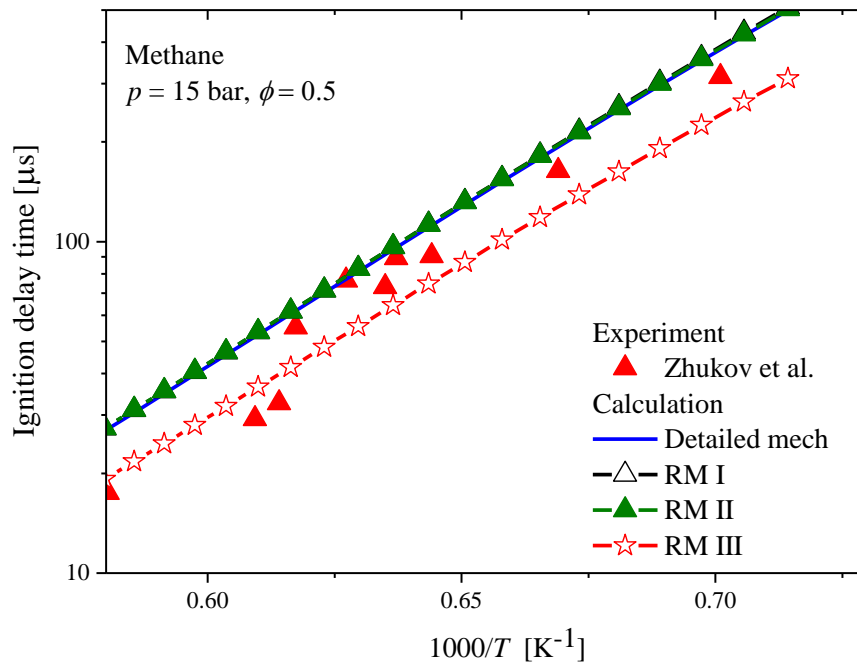

Figure 5.10: Calculated (lines; this work) and experimental (symbols; Zhukov et al. [96]) ignition delay times of methane/air mixtures: $p = 15$ bar, $\phi = 0.5$.

Syngas ignition delay times. The investigation of the syngas combustion characteristics of the mechanisms is important because of the recirculation of syngas in the gasifier as explained in section 2.4. In the gasification process, the syngas produced is brought to the top region of the reactor through a recirculation flow (see Fig. 2.4) and syngas combustion takes place in the reactor in addition to ethylene glycol oxidation. Therefore, the mechanisms should predict well the combustion characteristics of syngas. Figures 5.11 and 5.12 present the performance of the mechanisms in predicting the ignition delay times of syngas. Obviously, all mechanisms predict well the syngas IDL in the high temperature region which is important in the gasification process of REGA. The reduced mechanism III has a better performance in the low temperature region, for T < 1100 K. The reduced mechanisms I and II show similar agreement with the detailed mechanism.

In summary, it can be concluded that all the investigated mechanisms show very good performance in predicting the ignition delay times of ethylene glycol, syngas, acetaldehyde and methane under the investigated conditions.

Table 5.1 presents a summary of the performance of the reduced mechanisms in ignition delay time computations with respect to the detailed mechanism.
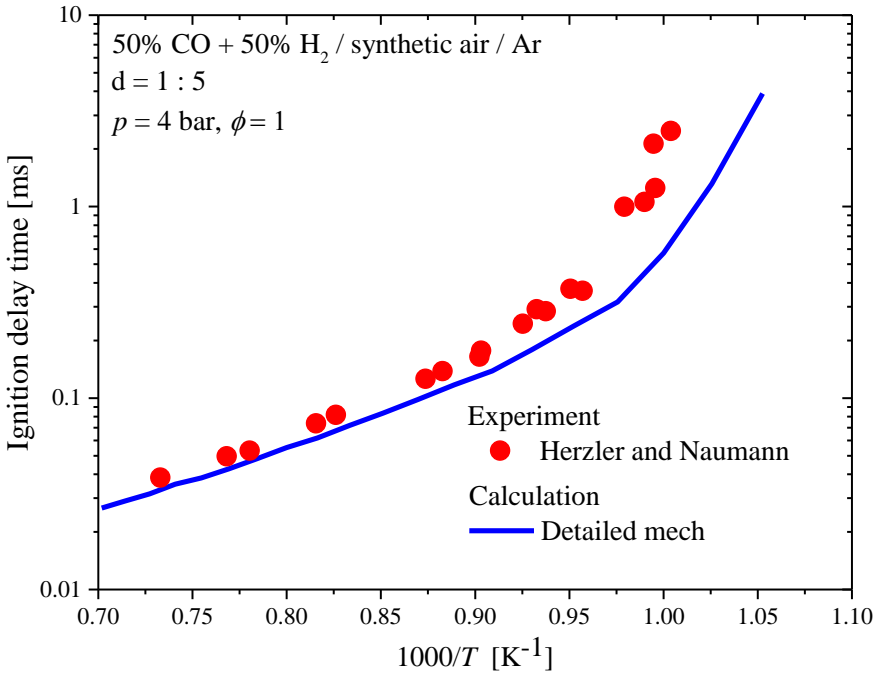

Figure 5.11: Calculated (lines; detailed mechanism, Kathrotia et al. [43]) and experimental (symbols; Herzler and Naumann [97]) ignition delay times of syngas/air mixtures: $p = 4$ bar, $\phi = 1$.
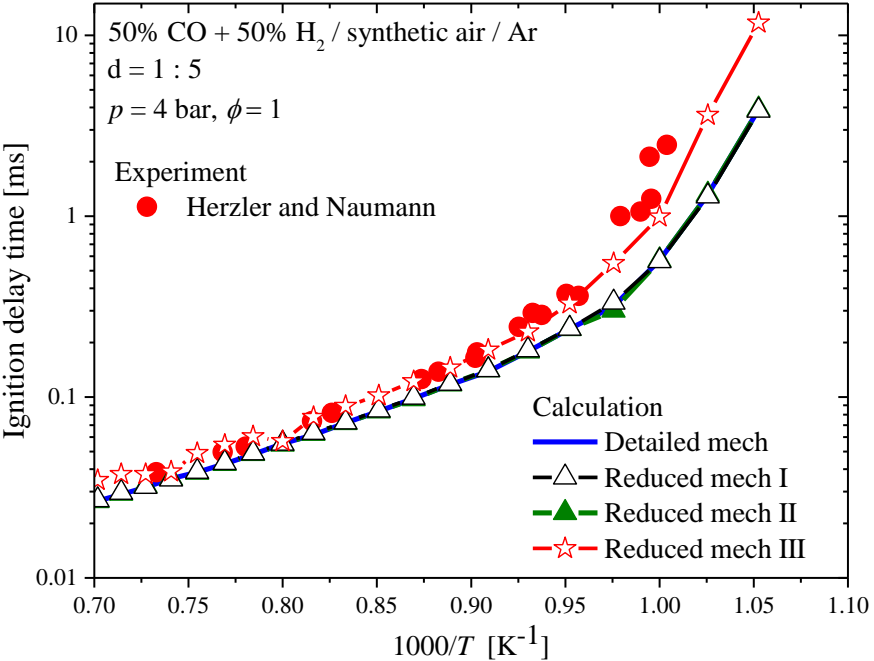

Figure 5.12: Calculated (lines; this work) and experimental (symbols; Herzler and Naumann [97]) ignition delay times of syngas/air mixtures: $p = 4$ bar, $\phi = 1.0$.

Table 5.1: Summary of the performance of the reduced mechanisms in ignition delay time computations with respect to the detailed mechanism. Green: Very good agreement, Yellow: Good agreement, Red: Satisfactory agreement.

ethylene glycol		acetaldehyde		methane		syngas	
Calc.	Overall Eval.	Calc.	Overall Eval.	Calc.	Overall Eval.	Calc.	Overall Eval.
16 bar	RI	3.5 bar	RI	3.5 bar	RI	3.5 bar	RI
Ø = 1	RII	Ø = 0.5	RII	Ø = 0.5	RII	Ø = 0.5	RII
800<T<1400	RIII	1300<T<1650	RIII	1500<T<1700	RIII	950<T<1400	RIII
		3.5 bar	RI	15 bar	RI		
		Ø = 2	RII	Ø = 0.5	RII		
		1300<T<1800	RIII	1400<T<1700	RIII		

5.3 Validation of the reaction mechanisms – Laminar flame speeds

As a second step of validating the reaction mechanisms used and developed within the present work, calculated laminar flame speeds (LFS) of the EG/air mixture and its major intermediates, acetaldehyde and methane are compared against experimental data from literature. A summary of LFS calculations are given in Table 2.4.

Ethylene glycol laminar flame speed data. Figure 5.13 presents the calculation results of laminar flame speeds of ethylene glycol over the equivalence ratio range of 0.5 to 1.75, at atmospheric pressure and at a preheat temperature of 318 K. Unfortunately, no experimental data are available for ethylene glycol flame speeds in the literature. Therefore, the performance of the three reduced mechanisms is compared against the detailed mechanism. According to Fig. 5.13, in the fuel lean region, for $\phi < 0.9$, all three reduced mechanisms show almost identical performance with respect to the detailed mechanism. All mechanisms predict the peak flame speed at an equivalence ratio of about 1.15 and the predicted value deviates only slightly (about 2%) among each other. The deviations between the reduced mechanisms increase for $\phi > 1.4$, with maximum deviation compared to the detailed mechanism, as shown by the reduced mechanism III, reaches about 14%. Overall, all three reduced mechanisms capture well the flame speeds predicted by the detailed mechanism.
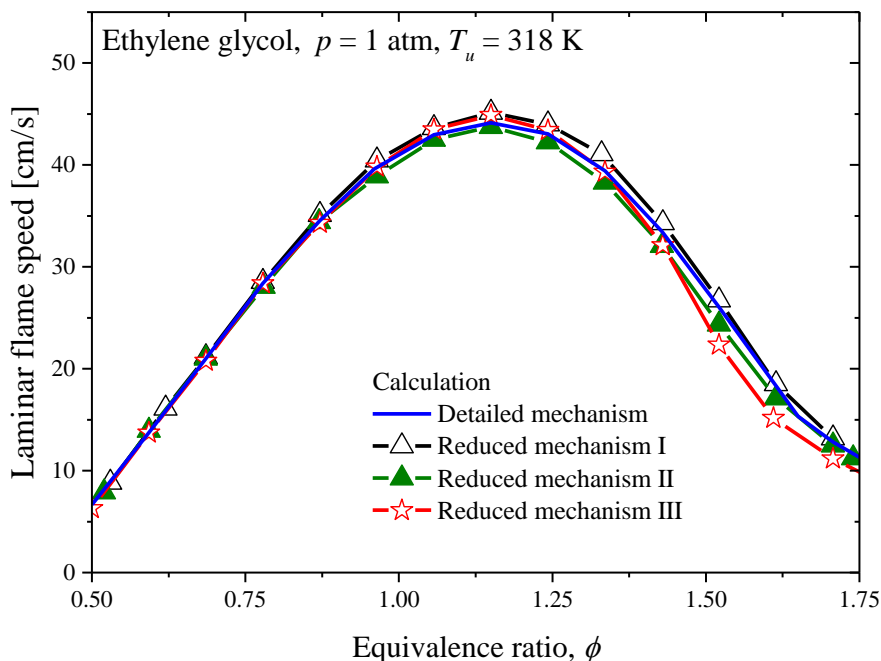
Figure 5.13: Calculated (curves; this work) laminar flame speeds of ethylene glycol/air mixtures: p = 1 atm, T_u = 318 K.

Acetaldehyde laminar flame speed data. Figures 5.14 and 5.15 present the comparison of the calculated and experimental laminar flame speeds of acetaldehyde / air mixtures at atmospheric pressure at two different temperatures (338 K and 348 K) for equivalence rations from 0.5 to 1.8. In both cases, the detailed mechanism (solid blue curves) reproduces the experimental data with good accuracy. The maximum flame speed and the location of the maximum, at around ϕ = 1.1, are well predicted by the computations. All reduced mechanisms show good agreement with the detailed mechanism in fuel lean conditions while a deviation of approx. 10% can be observed in fuel rich conditions. The slight deviation in fuel rich region can be explained by the target conditions used in the reduction procedure. The target conditions were selected to have an equivalence ratio of one. Overall, all three reduced mechanisms show a good agreement with the experimental data and the detailed mechanism in predicting laminar flame speeds of acetaldehyde.
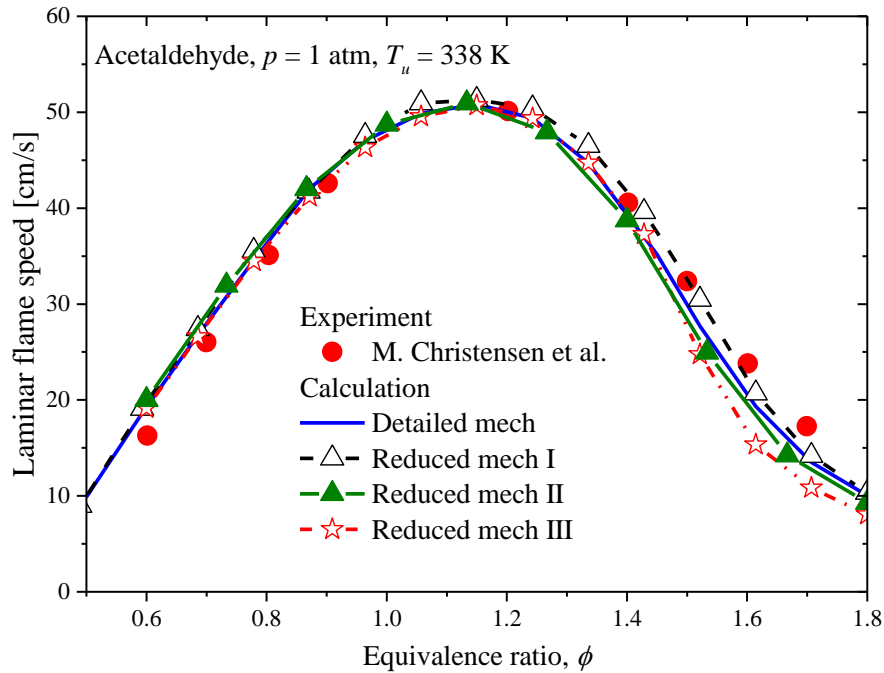
Figure 5.14: Calculated (lines; this work) and experimental (symbols; M. Christensen et al. [98]) laminar flame speeds of acetaldehyde/air mixtures: $p = 1$ atm, $T_u = 338$ K.
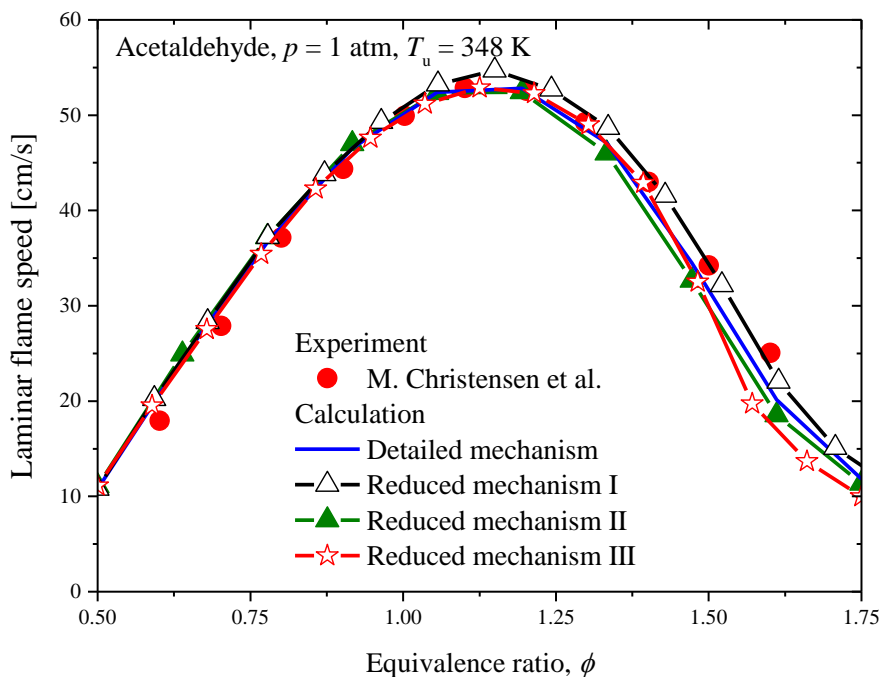
Figure 5.15: Calculated (lines; this work) and experimental (symbols; M. Christensen et al. [98]) laminar flame speeds of acetaldehyde/air mixtures: $p = 1$ atm, $T_u = 348$ K.

Methane laminar flame speed data. Figure 5.16 presents the results of the methane/air flame speed computations at atmospheric pressure at a preheat temperature of 298 K. The detailed reaction mechanism (solid blue curve) has a good agreement with the experimental data in the fuel lean region, for $\phi < 0.77$, and the fuel rich one, for $1.2 < \phi < 1.4$. The detailed mechanism

slightly underpredicts the laminar flame speed for $0.77 < \phi < 1.2$. The location of the maximum flame speed (at $\phi = 1.1$) is well predicted by the detailed mechanism.

All three reduced mechanisms show little deviation in the fuel lean region, as compared to the detailed mechanism. In the fuel rich region, the reduced mechanisms I and III show a divergence from the detailed mechanism by about 10 % and 12% respectively.
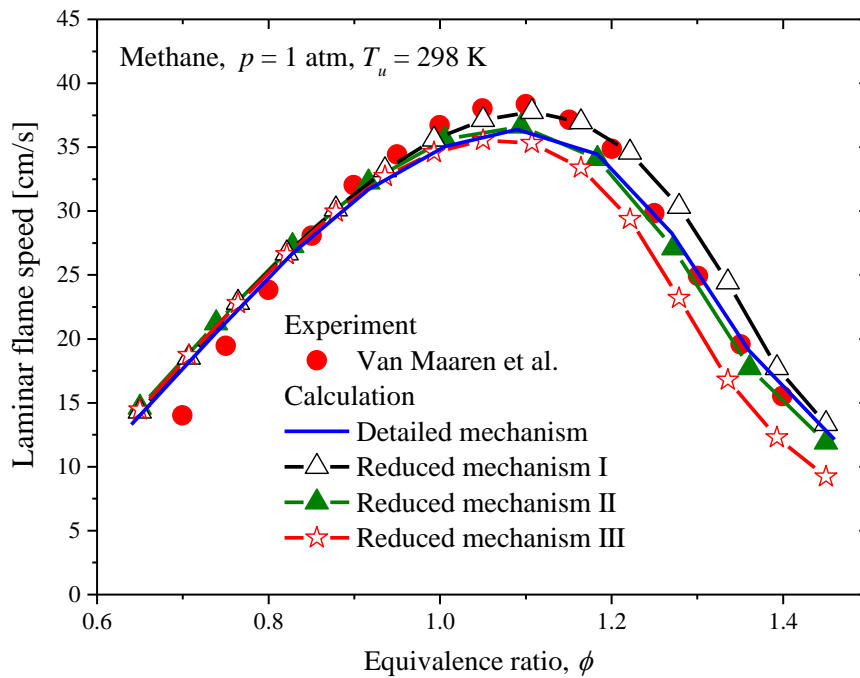

Figure 5.16: Calculated (lines; this work) and experimental (symbols; Van Maaren et al. [99]) laminar flame speeds of methane/air mixtures: $p = 1$ atm, $T_u = 298$ K.

Figure 5.17 presents the calculated and experimental methane flame speeds at a pressure of 3 bar and a preheat temperature of 300 K. It is observed that the detailed mechanism and two reduced mechanisms show a good agreement with the experimental data, but not the reduced mechanism III. The mechanisms reproduce well the flame speeds within the fuel lean and fuel rich regions as well as the maximum flame speed and the location of the maximum flame speed.

The reduced mechanism III underestimates the methane flame speed for most of the equivalence ratios at this pressure. As can be seen from Table 5.1, reduced mechanism III has a significantly lower number of species and reactions as compared to the other two reduced models. This can explain the observed deviation of reduced mechanism III with the other two reduced mechanisms and the detailed mechanism.
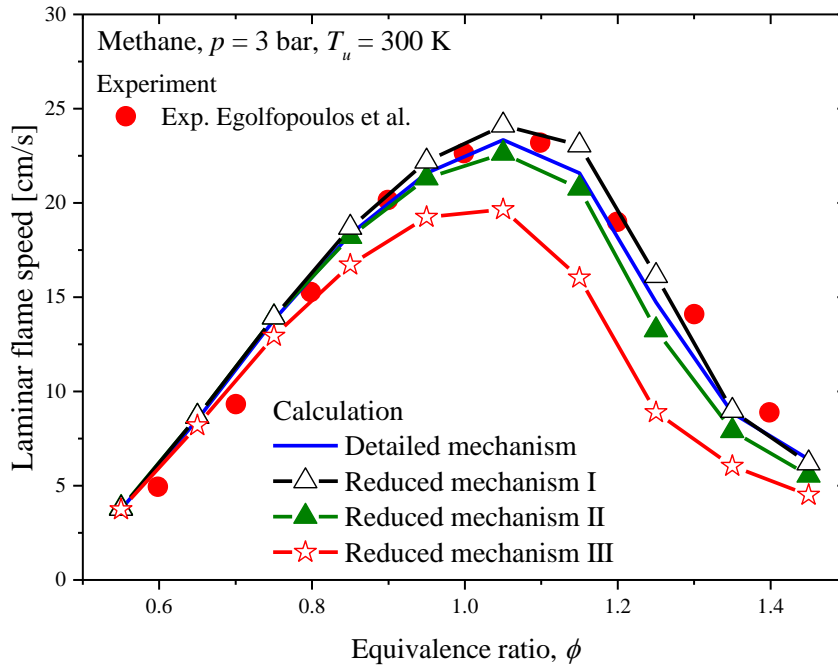
Figure 5.17: Calculated (lines; this work) and experimental (symbols; Egolfopoulos et al. [100]) laminar flame speeds of Methane/air mixtures: $p = 3$ bar, $T_u = 300$ K.

Table 5.2 presents a summary of the performance of the reduced mechanisms in laminar flame speed computations with respect to the detailed mechanism.

Table 5.2: Summary of the performance of the reduced mechanisms in laminar flame speed computations with respect to the detailed mechanism. Green: Very good agreement, Yellow: Good agreement, Red: Satisfactory agreement.

ethylene glycol		acetaldehyde		methane	
Calc.	Overall Eval.	Calc.	Overall Eval.	Calc.	Overall Eval.
1 atm	RI	1 atm	RI	1 atm	RI
$0.5 < \emptyset < 1.75$	RII	$0.5 < \emptyset < 1.8$	RII	$0.6 < \emptyset < 1.45$	RII
$T_u = 318$ K	RIII	$T_u = 338$ K	RIII	$T_u = 298$ K	RIII
		1 atm	RI	3 bar	RI
		$0.5 < \emptyset < 1.75$	RII	$0.6 < \emptyset < 1.45$	RII
		$T_u = 348$ K	RIII	$T_u = 300$ K	RIII

Performance of the detailed and the reduced mechanisms with respect to ignition delay time and laminar flame speed. Comparing the performances of the mechanisms with respect to ignition delay time and laminar flame speed computations, the detailed mechanism shows a good agreement with the experimental data for all investigated conditions for all fuels.

Among the three reduced mechanisms, the reduced mechanism II shows the best agreement with the detailed one (Tables 5.1 and 5.2). The reduced mechanism III has the smallest number of species and reactions among the three reduced mechanisms but showed the highest deviation from the detailed mechanism.

In the present work, a reduced mechanism will be used to perform a parameter study of for the REGA gasifier using CFD simulations. This makes it important for the reduced mechanism to perform similar to the detailed mechanism, i.e. with a similar accuracy, in a wide range of operating conditions, with respect to temperature, pressure and equivalence ratios. The CFD simulations introduce a harder test for the reduced mechanism compared to IDTs and laminar flame speeds. This is because the CFD simulation presents a largely varying set of thermochemical states with in a single simulation, as compared to the single specified condition in an IDT or laminar flame speed calculation.

The reduced mechanism II is selected as the most suitable one of the reduced three mechanisms for the REGA parameter study. This mechanism, having 48 species and 297 reactions (Table 2.3), is further validated by CFD simulations of the REGA gasifier and the results are presented in section 5.4.

5.4 Validation - CFD simulation using the detailed reaction mechanism

In this section, the performance of the detailed mechanism in a two-dimensional CFD simulation of the REGA environment will be presented. For the validation of the detailed mechanism, the radial profiles of the syngas components, CO, H_2, CH_4, CO_2, and temperature will be calculated at two locations along the height of the gasifier (300 mm and 680 mm downstream of the injection point) and compared against the experimental data obtained from [41]. The operating equivalence ratio of the gasifier is 2.12 in accordance with the experimental conditions [41].

Figure 5.18 presents the comparison of experimental data and calculated radial variation of the syngas components CO, H_2, and CH_4 together with CO_2 profiles at a distance of 300 mm downstream from the injection point. Away from the flame zone, the calculated species profiles show little radial variation. The trend of the distribution of the gas components is well predicted by the simulation. Methane (squares) is produced in small percentages according to the simulation, which is in agreement with the experimentally measured data. H_2 (traingles) concentrations are slightly underpredicted by the calculations, by up to about 6% (concentration difference), at the center. CO concentrations (circles) are overpredicted in the

simulation, with a maximum deviation of about 5% at the axis. The CO_2 concentrations (rhombs) are underpredicted by around 6%. These deviations can be attributed, at least to some extent, to simplifications in the CFD simulation, such as the RANS approach and turbulence chemistry interaction model. At the axis, the CO and CO_2 profiles have a peak value, while the H_2-profile depicts a minimum. These radial variations correspond to the radial extension of the flame zone, where the production of CO and CO_2 as well as the consumption of H_2 takes place.
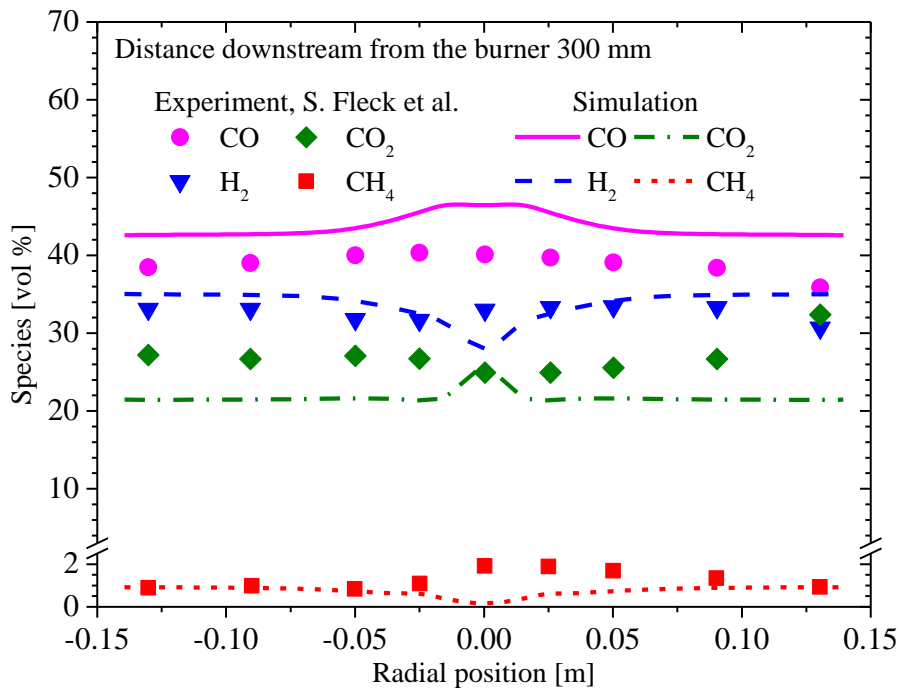
Figure 5.18: Calculated (curves; detailed mechanism, this work) and experimental (symbols; Fleck *et al.* [41]) radial species profiles of CO, H_2, CO_2, and CH_4 at a distance of 300 mm downstream from the injection point.

Figure 5.19 presents the comparison between calculated values and experimental data of CO, H_2, CH_4, and CO_2 profiles at a distance of 680 mm from the injection point. At this location, the calculated species profiles show a nearly uniform variation along the radial direction, which is in agreement with the experimental profiles. The simulation correctly predicts the relative distribution of the syngas components. The H_2-concentration is well predicted; the CO concentration is over predicted by about 3% (concentration difference), while the CO_2 concentration is under predicted by around 4%. The CH_4 percentages are less than 1% in both the experiment and the calculation, with the calculation slightly over predicting the measured values.

Figure 5.20 presents the comparison between calculated and experimental radial temperature profiles at two distances downstream from the injection point, at 300 mm (red) and 680 mm (black), respectively. The radial temperature measured at 680 mm is well predicted by the simulation. At 300 mm location, the experimental radial temperature in the wall region (red stars) is correctly predicted by the simulation (curve, red dash dotted), while it is over predicted by around 300 K in the flame region. This difference can be partly attributed to the hydrogen under prediction by the model at the axis mentioned earlier, which implies a high hydrogen burn out by the CFD model resulting in a high heat release and in a high temperature thus over predicting the experimental value. Experimental uncertainties can also contribute to the observed deviation between the experimental and the calculated values.
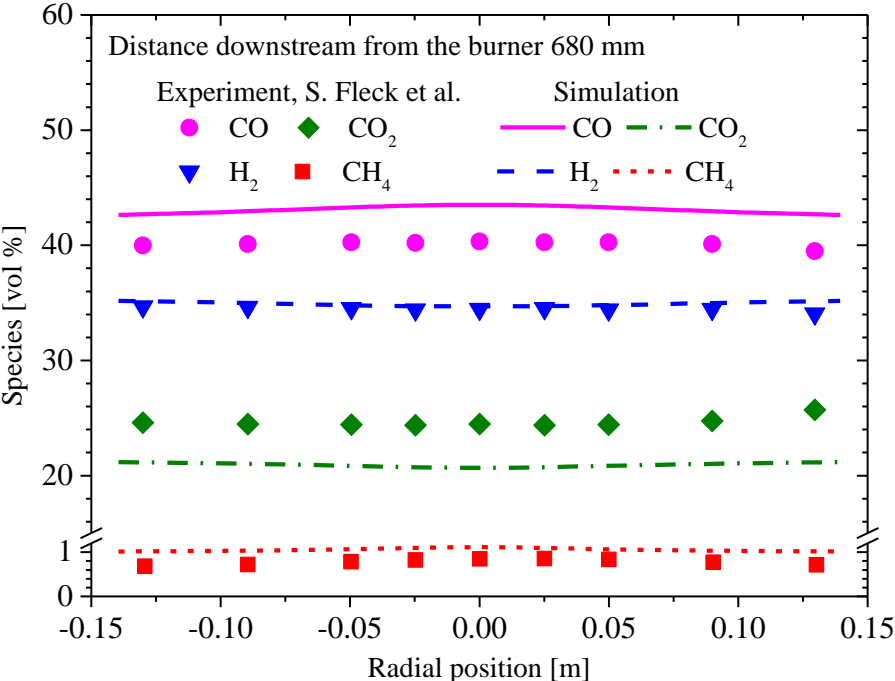

Figure 5.19: Calculated (curves; detailed mechanism, this work) and experimental (symbols; Fleck et al. [41]) radial species profiles of CO, H_2, CO_2 and CH_4 at a distance of 680 mm downstream from the injection point.

Based on the validation results presented in Figs. 5.18 – 5.20, it is concluded that the CFD simulation using the detailed reaction mechanism for ethylene glycol [43] is in good agreement with the experimental data [41] in terms of the prediction of the syngas components as well as of the radial temperature profiles in the REGA gasifier.
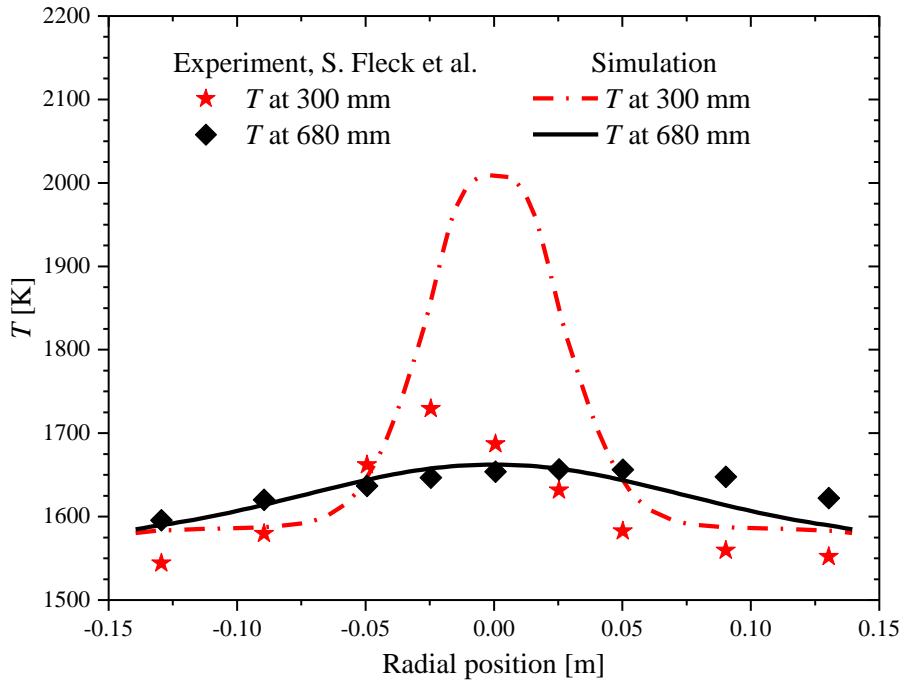
Figure 5.20: Calculated (curves; detailed mechanism, this work) and experimental (symbols; Fleck et al. [41]) radial temperature profiles at distances of 300 mm and 680 mm downstream from the injection point.

5.5 The flow fields calculated with the detailed EG reaction mechanism within the REGA

Figure 5.21 presents the two-dimensional flow fields of velocity, temperature, and mole fractions of ethylene glycol, O_2, as well as CO and H_2 which are major syngas components. The streamline plot shows the presence of the recirculation zone (Fig. 5.21a), also identified in previous studies using the Euler-Lagrange approach [65]. The recirculation zone brings the syngas from the bottom of the gasifier to the top where it is burnt together with the bio-slurry surrogate, ethylene glycol. Just below the injection point, the temperature field shows the maximum value (Fig. 5.21b). This region is rich with recirculated syngas and oxygen supplied at the injection (Fig. 5.21d), indicating the combustion of the recirculated syngas and ethylene glycol. The comparison of the H_2, CO, and O_2 fields suggests that (most) CO and H_2 are not produced within the combustion zone but outside, under fuel rich conditions within the lower region of the flame.

(a) Velocity field   (b) Temperature field   (c) ethylene glycol (gas)

(d) O_2 (e) CO   (f) H_2
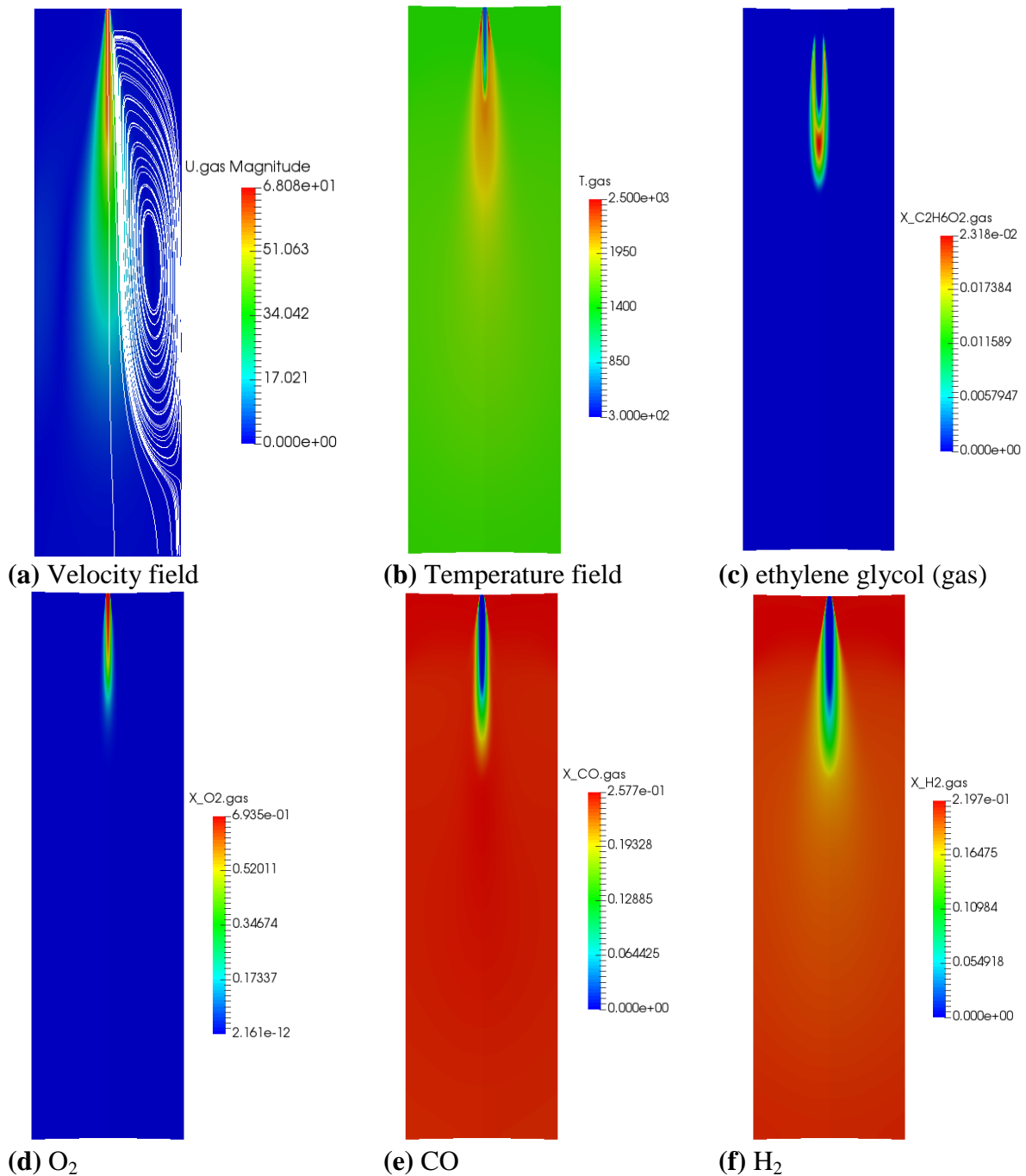
Figure 5.21: Calculated (detailed mechanism) two dimensional flow fields within the reactor.

5.6 Validation of the reduced mechanism II – CFD simulations

In this section, the results of the CFD simulations of the REGA gasifier obtained using the reduced mechanism are presented. The comparison between calculated and measured radial profiles of temperature and species concentrations of CO, H_2, CH_4, and CO_2 will be given. The ultimate aim of the present work is to develop a CPU time efficient, well validated

reduced reaction mechanism for ethylene glycol which can be used to perform parameter studies of REGA gasification process using CFD simulations. In terms of CPU time, the developed reduced reaction mechanism II is approximately 5 times faster compared to the detailed mechanism.

The selected reduced mechanism II is validated using two experimental data sets, one at an equivalence ratio ϕ of 2.12 [41] and the other one for $\phi = 1.67$ [42]. The operating conditions of the gasifier under these experimental conditions are summarized in Tables 4.1 and 4.2 in chapter 4.

5.6.1 Species and temperature profiles at an equivalence ratio of 2.12

Figure 5.22 presents the comparison of calculated radial species profiles using the reduced reaction mechanism II with experimental data obtained from [41].
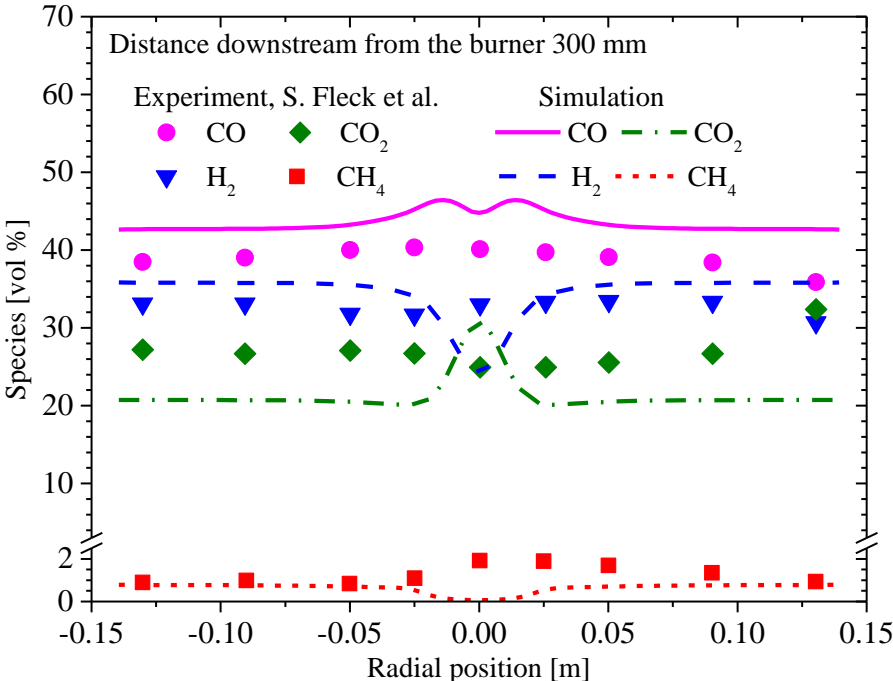
Figure 5.22: Calculated (curves; reduced mechanism II, this work) and experimental (symbols; Fleck et al. [41]) radial species profiles of CO, H_2, CO_2, and CH_4 at a distance of 300 mm downstream from the injection point.

The reduced mechanism predicts well the relative distribution of gas phase components. In the wall region, measured CO concentrations (peak about 40 %) - are over predicted by the calculations (peak about 45 %), with a deviation of about 5% by the concentration difference, while CO_2 concentrations are under predicted by around 8%. H_2 concentrations in the wall region are slightly over predicted (by around 2 %) by the simulation. Methane is predicted in

75

small percentages in the calculations, which is confirmed by the experiment. The species profiles in the central region of the reactor show strong radial variations. These radial variations correspond to the radial extension of the flame zone, where production of CO and CO_2 as well as H_2 consumption takes place.

In Fig. 5.23, species profiles calculated for a distance of 680 mm downstream of the injection point are presented against the experimental data. At this location, the simulation using the reduced mechanism correctly predicts the uniform radial variation of species profiles, as well as the distribution of syngas components. The H_2 concentrations are accurately predicted by the simulation. CO concentration is over predicted by around 4 % and CO_2 concentrations are under predicted by around 6 %.
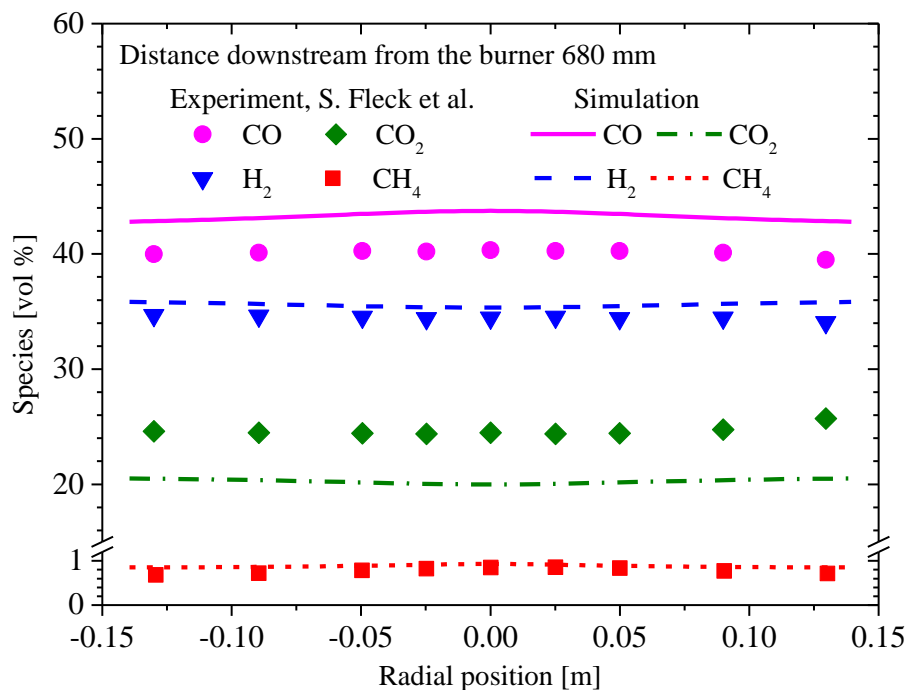

Figure 5.23: Calculated (curves; reduced mechanism II, this work) and experimental (symbols; Fleck et al. [41]) radial species profiles of CO, H_2, CO_2 and CH_4 at a distance of 680 mm downstream from the injection point.

Figure 5.24 presents the calculated and experimental temperature profiles at distances of 300 mm and 680 mm from the injection point. The simulation shows an over prediction of the temperature by about 300 K inside the flame zone while the temperatures outside the flame zone are well predicted. This behavior was also observed with the detailed mechanism. The experimentally measured temperatures at a location 680 mm downwards the injection are well predicted by the simulation.
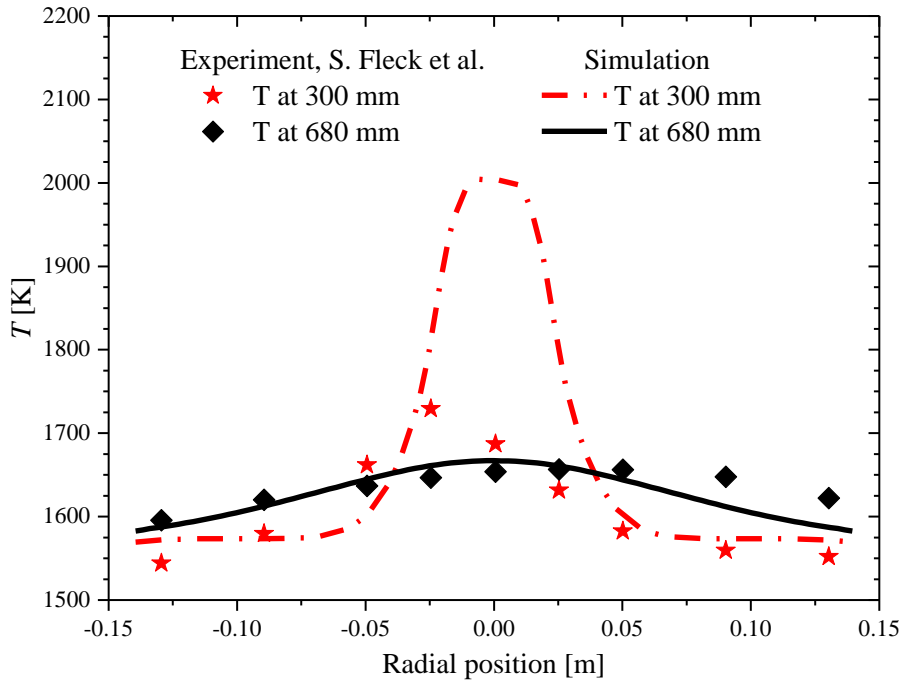
Figure 5.24: Calculated (curves; reduced mechanism II, this work) and experimental (symbols; S. Fleck et al. [41]) radial temperature profiles at distances of 300 mm and 680 mm downstream from the injection point.

5.6.2 Species and temperature profiles at an equivalence ratio of 1.67

Figure 5.25 presents the calculated radial species profiles of CO, H_2, CO_2 and CH_4 using the CFD simulation at a distance of 300 mm downstream of the injection point. The simulation is performed for an equivalence ratio of 1.67, corresponding to the experimental conditions described in [42]. The experimental data are obtained from [42]. The simulations are in good agreement with the experiment in the wall region of the reactor, in predicting the compositions of CO, H_2, and CO_2. In the flame region, both the CO and H_2 concentrations are under predicted in the simulations, while the CO_2 concentration is over predicted.

In Fig. 5.26, species profiles calculated at a distance of 680 mm downstream of the injection point is presented against the experimental data. All the major species concentrations show a very good agreement with the experimental data while the minor product methane concentration is over predicted by the simulation.
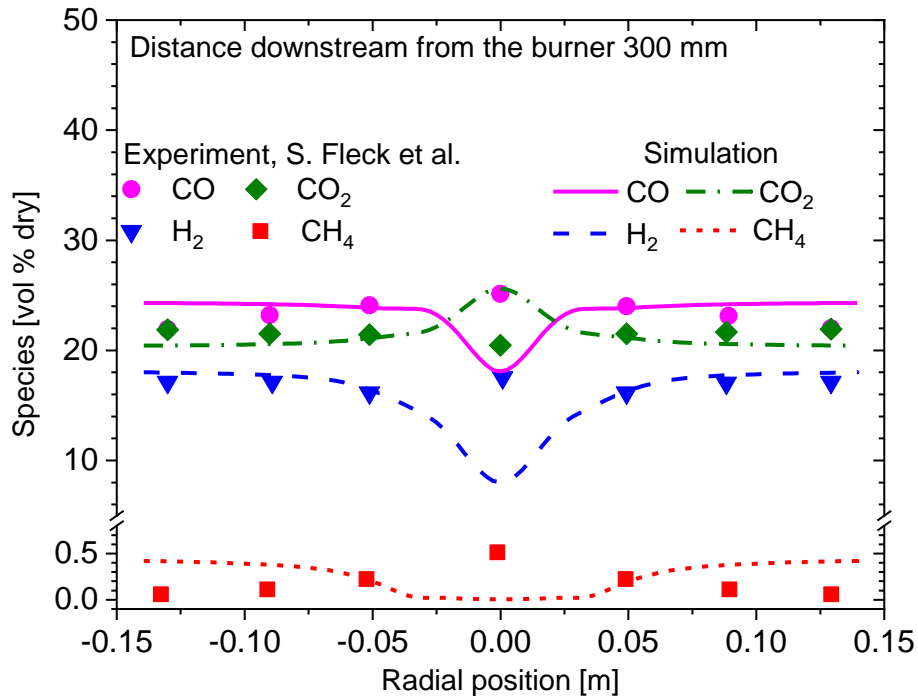
Figure 5.25: Calculated (curves; reduced mechanism II, this work) and experimental (symbols; S. Fleck et al. [42]) radial species profiles of CO, H_2, CO_2 and CH_4 at a distance of 300 mm downstream from the injection point.
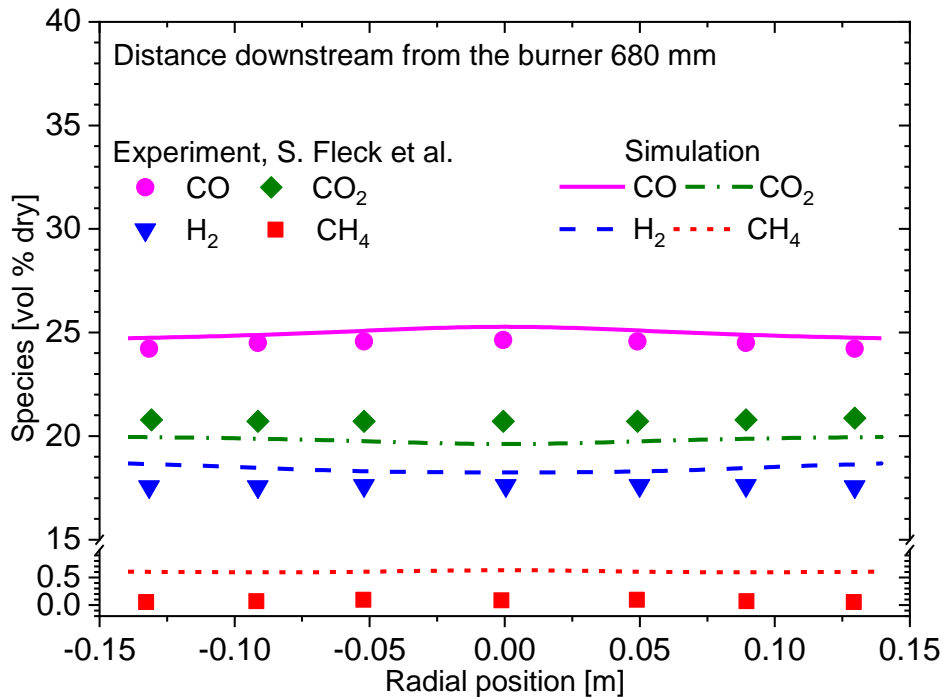
Figure 5.26: Calculated (curves; reduced mechanism II, this work) and experimental (symbols; S. Fleck et al. [42]) radial species profiles of CO, H_2, CO_2 and CH_4 at a distance of 680 mm downstream from the injection point.

Figure 5.27 presents the calculated temperature profiles of the REGA gasifier, at distances of 300 mm and 680 mm from the injection point. The calculated profiles are in good agreement with the experimental data.
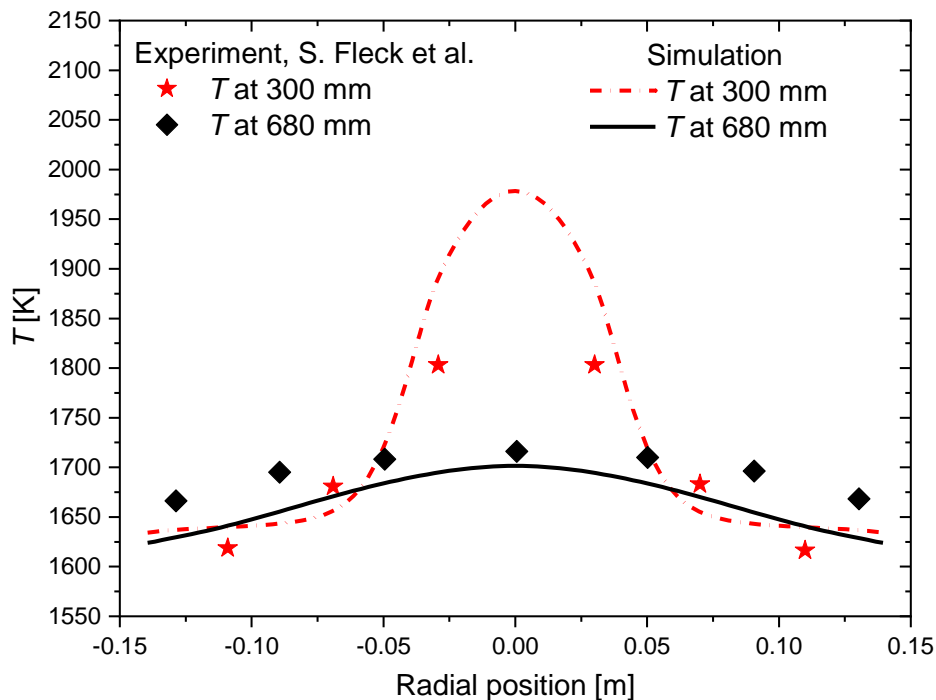

Figure 5.27: Calculated (curves; reduced mechanism II, this work) and experimental (symbols; S. Fleck et al. [42]) radial temperature profiles at distances of 300 mm and 680 mm downstream from the injection point.

In summary, by considering all the validation calculations, it can be concluded that the developed reduced mechanism can be used successfully to predict the gasification kinetics of ethylene glycol with respect to syngas production.

5.7 A parameter study on the effect of operating conditions on the syngas composition

5.7.1 Effect of the fuel preheat temperature

Figures 5.28 presents the variation of syngas component mole fractions at the exit against the preheat temperature of liquid ethylene glycol. The temperature range investigated was from room temperature to 425 K. The maximum investigated temperature was selected to be lower than the boiling point of ethylene glycol at atmospheric pressure, which is 473 K. The predicted effect of increasing the preheat temperature is a slight increase in CO and H_2 mole fractions and a slight decrease in CO_2 and H_2O mole fractions. This variation can be explained by considering the evaporation of liquid ethylene glycol. With an increase of

preheat temperature of the liquid ethylene glycol, the amount of evaporated ethylene glycol to the gas phase within the flame zone increases, which in turn increases the local equivalence ratio to the fuel rich direction, resulting in an increase of CO and H_2. The variation cannot be observed after the preheat temperature has reached a certain value (about 375 K), indicating that further increase in preheat temperature do not change significantly the fraction of evaporated liquid ethylene glycol within the flame zone.

(a)	(b)
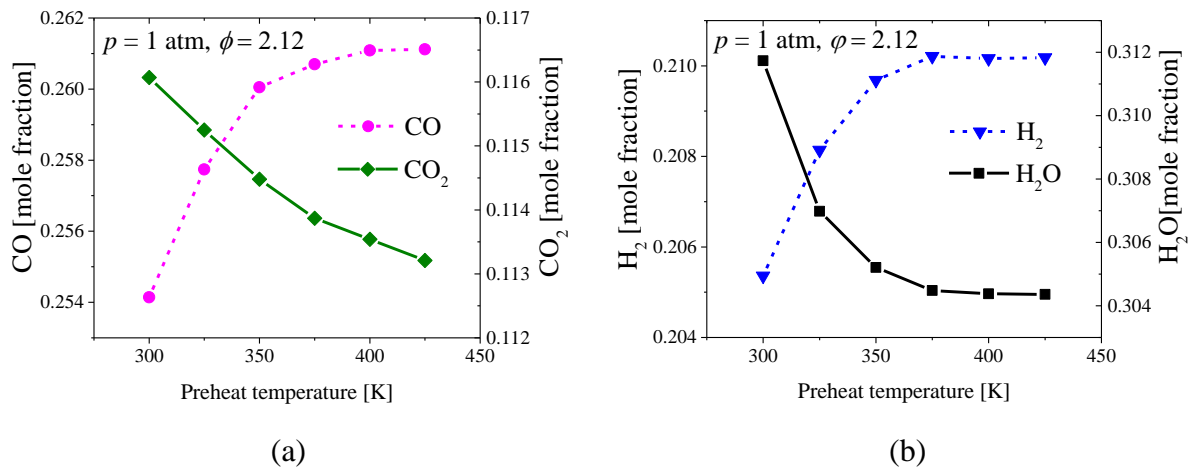
Figure 5.28: Calculated (reduced mechanism II) exit mole fractions of (a) CO and CO_2, (b) H_2 and H_2O vs. fuel preheat temperature at $p = 1$ atm and $\varphi = 2.12$.

5.7.2 Effect of the equivalence ratio

The equivalence ratio has the strongest effect on the composition of the syngas. Fig. 5.29 presents the variation of CO, H_2, CO_2, and H_2O mole fractions against the equivalence ratio.

|	
(a)	(b)
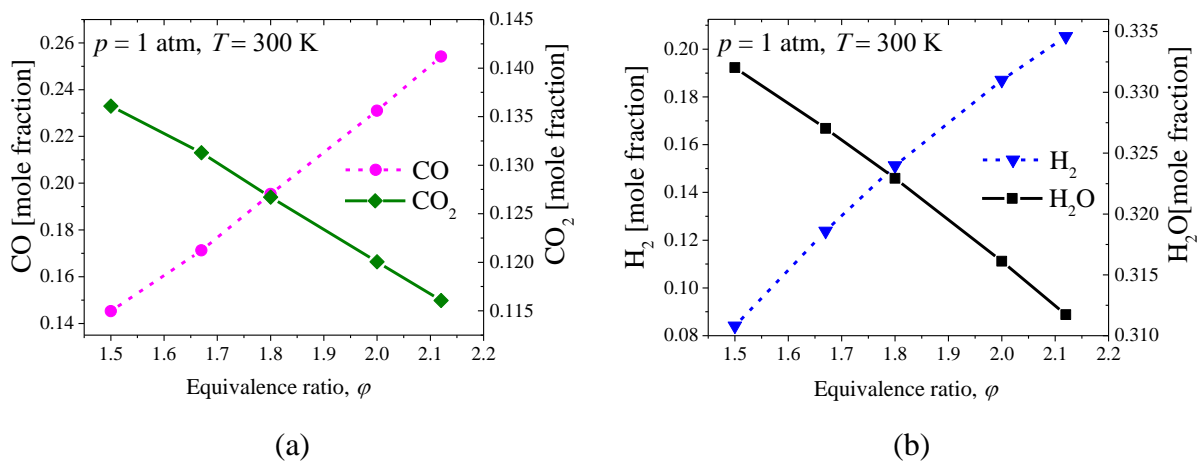
Figure 5.29: Calculated (reduced mechanism) exit mole fractions of (a) CO and CO_2, (b) H_2 and H_2O vs. equivalence ratio at $p = 1$ atm and fuel preheat temperature of 300 K.

It can be observed that the variation is almost linear in the investigated equivalence ratio range. Similar results have been observed by an earlier study of the REGA gasifier using

Euler-Lagrange simulations in the work of Rashidi et al. [86]. With the increase of equivalence ratio, the mole fractions of the combustible components (CO and H_2) increase, while those of the oxidation products H_2O and CO_2 decrease. This is because the oxygen amount in the inlet gas stream is increasingly insufficient to completely oxidize the fuel.

5.7.3 Effect of the operating pressure

Figure 5.30 presents the effect of operating pressure on the syngas composition. The mole fractions of CO and H_2O decrease with increasing pressure while the CO_2 and H_2 mole fractions increase. These results can be understood in terms of the equilibrium kinetics of the exit syngas. The equilibrium relation between the syngas components can be approximated by the water gas shift reaction,

$$CO + H_2O \leftrightharpoons CO_2 + H_2 \qquad\qquad R5.5$$

The equilibrium constant of the water gas shift reaction decreases with increasing temperature [101]. In the simulations it has been observed that the temperature of the exit gas slightly decreases with the increase of pressure, therefore driving the equilibrium of reaction R5.5 to the right; this explains the observed variation of species concentrations of CO, CO_2, H_2, and H_2O in Fig. 5.30. The slope of pressure vs. concentration curve decreases as the pressure increases. This observed behavior of the syngas composition vs. operating pressure was also reported in another study of the REGA, conducted using an ideal jet stirred reactor model [86].


(a)   (b)
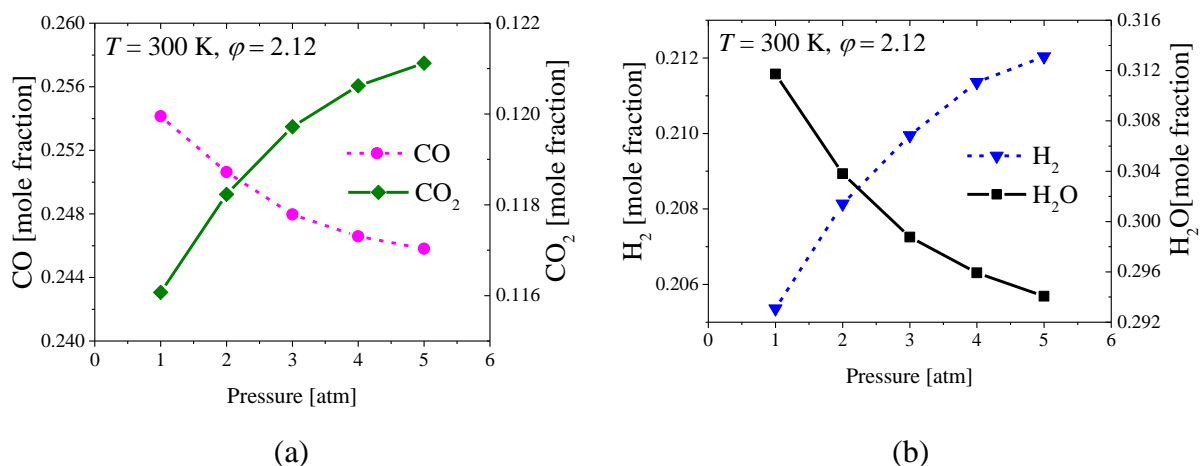
Figure 5.30: Calculated (reduced mechanism) exit mole fractions of (a) CO and CO_2, (b) H_2 and H_2O vs operating pressure at fuel preheat temperature of 300 K and $\varphi = 2.12$.

6. Summary and Conclusion

The adverse environmental impacts and increasing prices of fossil fuels indicate the need for the research on renewable fuels. Biomass based fuels are a widely used class of renewable energy sources. The aim of the present work was first, to develop a reduced and validated chemical kinetic reaction mechanism capable to describe the gasification process of a pyrolysis oil surrogate; second, to include this reduced reaction model into a CFD tool; and finally, to model the entrained flow gasification process of the REGA gasifier using CFD simulations.

A detailed reaction mechanism developed earlier in our group to model the oxidation process of ethylene glycol was used as the starting point to develop the reduced mechanism in the present work. Three reduced mechanisms were developed using three different reduction methods; sensitivity analysis, directed relation graph, and a novel reduction technique developed in our group which uses sensitivity analysis and linear transformations.

The performance of the detailed mechanism and the three reduced mechanisms was then investigated by computing ignition delay times and laminar flame speeds of ethylene glycol, methane and acetaldehyde over a wide range of conditions (pressure: 1 bar to 16 bar, temperature: 298 K to 1800 K, equivalence ratio: 0.5 to 2) and comparing the results with published experimental data. It was observed that all mechanisms show good agreement with the experimental data at the conditions investigated. Among the three reduced mechanisms, it was observed that the reduced mechanism developed using the directed relation graph method had the best performance. This reduced mechanism was selected for further validation using CFD simulations.

The CFD simulation of the REGA gasifier was performed using the open source CFD tool OpenFOAM. The Euler-Euler approach was used to model the two phase system. The results of the CFD simulations were compared against the published experimental data from the REGA. The calculated species profiles of CO, H_2, CO_2, and CH_4 as well as temperature profiles at two different locations on the axis of the gasifier; 300 mm and 680 mm downstream of the injection point, were compared against the published experimental data from REGA.

The simulation results obtained using the detailed mechanism were used to study the fuel conversion in the gasifier using two dimensional species, flow and temperature fields within

the reactor. A reaction pathway analysis was performed using the detailed reaction mechanism to investigate the pathways to syngas production under the gasification conditions of the REGA.

It was found that both the detailed mechanism and the reduced mechanism show very good agreement with the experimental data while the reduced mechanism was found to be approximately 5 times faster in terms of CPU time as compared to the detailed mechanism.

Finally, the validated reduced reaction mechanism was used to perform a parameter study of the REGA. The study consisted of conducting a series of CFD simulations under different operating conditions of the gasifier. The investigated parameters were the fuel preheat temperature, the operating pressure and the equivalence ratio. The results of the simulations showed that the equivalence ratio had the strongest impact on the syngas composition produced, leading to an increase of the mole fractions of combustible components (CO and H_2) of the syngas with the equivalence ratio. Fuel preheat temperature had a minor impact on the syngas composition. The effect was an increase of combustible components with increasing temperature. The composition of the syngas for a given equivalence ratio and a preheat temperature only slightly varied with pressure. However, conversion of syngas under higher pressures may have other advantages such as reduced sizing of the reactor and the ease of downstream fuel processing in situations where syngas is targeted to be subjected to high pressure fuel conversion processes.

In summary, it can be concluded that the tools developed in the present work can be successfully used to model the entrained flow gasification process of pyrolysis oil, in REGA and other similar entrained flow gasifiers, using ethylene glycol as a single component surrogate fuel for pyrolysis oil.

7. References

[1] "International Energy Agency," [Online]. Available: https://www.iea.org/. [Accessed 09 09 2019].

[2] P. McKendry, "Energy production from biomass (part 1): overview of biomass," *Bioresource Technology,* vol. 83, no. 1, pp. 37-46, 2002.

[3] J. Watson, Y. Zhang, B. Si, W. Chen and R. de Souza, "Gasification of biowaste: A critical review and outlooks," *Renewable and Sustainable Energy Reviews,* vol. 83, pp. 1-17, 2018.

[4] T. Nicodème, T. Berchem, N. Jacquet and A. Richel, "Thermochemical conversion of sugar industry by-products to biofuels," *Renewable and Sustainable Energy Reviews,* vol. 88, pp. 151-159, 2018.

[5] V. Dhyani and T. Bhaskar, "A comprehensive review on the pyrolysis of lignocellulosic biomass," *Renewable Energy,* vol. 129, no. Part B, pp. 695-716, 2018.

[6] S. Ladanai and J. Vinterbäck, "Global Potential of Sustainable Biomass for Energy," SLU, Institutionen för energi och teknik, Uppsala, 2009.

[7] P. McKendry, "Energy production from biomass (part 2): conversion technologies," *Bioresource Technology,* vol. 83, no. 1, pp. 47-54, 2002.

[8] V. S. Sikarwar, M. Zhao, P. S. Fennell, N. Shah and E. J. Anthony, "Progress in biofuel production from gasification," *Progress in Energy and Combustion Science,* vol. 61, pp. 189-248, 2017.

[9] I. U. Khan, M. H. D. Othman, H. Hashim, T. Matsuura, A. F. Ismail, M. Rezaei-DashtArzhandi and I. Wan Azelee, "Biogas as a renewable energy fuel – A review of biogas upgrading, utilisation and storage," *Energy Conversion and Management,* vol. 150, pp. 277-294, 2017.

[10] C. Di Blasi, "Modeling chemical and physical processes of wood and biomass pyrolysis," *Progress in Energy and Combustion Science,* vol. 34, no. 1, pp. 47-90, 2008.

[11] P. McKendry, "Energy production from biomass (part 3): gasification technologies," *Bioresource Technology,* vol. 83, no. 1, pp. 55-63, 2002.

[12] E. G. Pereira, J. N. da Silva, J. L. de Oliveira and C. S. Machado, "Sustainable energy: A review of gasification technologies," *Renewable and Sustainable Energy Reviews,*

vol. 16, no. 7, pp. 4753-4762, 2012.

[13] H. Mahmoudi, M. Mahmoudi, O. Doustdar, H. Jahangiri, A. Tsolakis, S. Gu and M. . L. Wyszynski, "A review of Fischer Tropsch synthesis process, mechanism, surface chemistry and catalyst formulation," *Biofuels Engineering,* no. 2, pp. 11-31, 2017.

[14] W. Chen, K. Annamalai, R. James Ansley and M. Mirik, "Updraft fixed bed gasification of mesquite and juniper wood samples," *Energy,* vol. 41, no. 1, pp. 454-461, 2012.

[15] "bioliq," [Online]. Available: https://www.bioliq.de/english/55.php. [Accessed 09 09 2019].

[16] M. Mohseni, B. Peters and M. Baniasadi, "Conversion analysis of a cylindrical biomass particle with a DEM-CFD coupling approach," *Case Studies in Thermal Engineering,* vol. 10, pp. 343-356, 2017.

[17] A. K. Sharma, "Equilibrium and kinetic modeling of char reduction reactions in a downdraft biomass gasifier: A comparison," *Solar Energy,* vol. 82, no. 10, pp. 918-928, 2008.

[18] J. C. Solarte-Toro, Y. Chacón-Pérez and C. A. Cardona-Alzate, "Evaluation of biogas and syngas as energy vectors for heat and power generation using lignocellulosic biomass as raw material," *Electronic Journal of Biotechnology,* vol. 33, pp. 52-62, 2018.

[19] N. Couto, A. Rouboa, V. Silva, E. Monteiro and K. Bouziane , "Influence of the biomass gasification processes on the final composition of syngas," *Energy Procedia,* vol. 36, pp. 596-606, 2013.

[20] "Fluidzed bed gasifiers," National energy technology laboratory, [Online]. Available: https://www.netl.doe.gov/research/coal/energy-systems/gasification/gasifipedia/fluidizedbed. [Accessed 03 04 2019].

[21] [Online]. Available: http://www.energy.kth.se/compedu/webcompedu/S4_Combustion/B10_Thermochemical_Conversion/C1_Introduction_to_Gasification/ID55_files/Fluidized_bed_gasifiers.htm. [Accessed 22 01 2019].

[22] "Biofuels Academy," [Online]. Available: http://biofuelsacademy.org/index.html%3Fp=204.html. [Accessed 22 01 2019].

[23] M. Puig-Arnavat, J. C. Bruno and A. Coronas, "Review and analysis of biomass gasification models," *Renewable and Sustainable Energy Reviews,* vol. 14, no. 9, pp. 2841-2851, 2010.

[24] C. Hanping, L. Bin, Y. Haiping, Y. Guolai and Z. Shihong, "Experimental Investigation of Biomass Gasification in a Fluidized Bed Reactor," *Energy & Fuels ,* vol. 22, no. 5, pp. 3493-3498, 2008.

[25] V. Kirsanovs, D. Blumberga, I. Veidenbergs, C. Rochas, E. Vigants and G. Vigants, "Experimental investigation of downdraft gasifier at various conditions," *Energy Procedia,* vol. 128, pp. 332-338, 2017.

[26] P. K. Senapati and S. Behera, "Experimental investigation on an entrained flow type biomass gasification system using coconut coir dust as powdery biomass feedstock," *Bioresource Technology,* vol. 117, pp. 99-106, 2012.

[27] Z. A. Zainal, A. Rifau, G. A. Quadir and K. N. Seetharamu, "Experimental investigation of a downdraft biomass gasifier," *Biomass and Bioenergy,* vol. 23, no. 4, pp. 283-289, 2002.

[28] A. Z. Mendiburu, J. A. Carvalho Jr. and C. J. R. Coronado, "Thermochemical equilibrium modeling of biomass downdraft gasifier: Stoichiometric models," *Energy,* vol. 66, pp. 189-201, 2014.

[29] M. Ruggiero and G. Manfrida, "An equilibrium model for biomass gasification processes," *Renewable Energy,* vol. 16, no. 1-4, pp. 1106-1109, 1999.

[30] H. Jiang and R. Vance Morey, "A numerical model of a fluidized bed biomass gasifier," *Biomass and Bioenergy,* vol. 3, no. 6, pp. 431-447, 1992.

[31] H. Liu, A. Elkamel, A. Lohi and M. Biglari, "Computational Fluid Dynamics Modeling of Biomass Gasification in Circulating Fluidized-Bed Reactor Using the Eulerian– Eulerian Approach," *Ind. Eng. Chem. Res.,* vol. 52, no. 51, p. 18162–18174, 2013.

[32] J. Li, M. C. Paul, P. L. Younger, I. Watson, M. Hossain and S. Welch, "Characterization of biomass combustion at high temperatures based on an upgraded single particle model," *Applied Energy,* vol. 156, pp. 749-755, 2015.

[33] B. Srinivas and N. R. Amundson, "A single-particle char gasification model," *AIChE journal,* vol. 26, no. 3, pp. 487-496, 1980.

[34] B. Fortunato, G. Brunetti, S. M. Camporeale, M. Torresi and F. Fornarelli, "Thermodynamic model of a downdraft gasifier," *Energy Conversion and Management,* vol. 140, pp. 281-294, 2017.

[35] D. F. Fletcher, B. S. Haynes , F. C. Christo and S. D. Joseph, "A CFD based combustion model of an entrained flow biomass gasifier," *Applied Mathematical Modelling,* vol. 24, no. 3, pp. 165-182, 2000.

[36] J. Xie, W. Zhong, B. Jin, Y. Shao and H. Liu, "Simulation on gasification of forestry residues in fluidized beds by Eulerian–Lagrangian approach," *Bioresource Technology,* vol. 121, pp. 36-46, 2012.

[37] Z. A. Zainal, R. Ali, C. H. Lean and K. N. Seetharamu, "Prediction of performance of a downdraft gasifier using equilibrium modeling for different biomass materials," *Energy Conversion and Management,* vol. 42, no. 12, pp. 1499-1515, 2001.

[38] N. Fernando and M. Narayana, "A comprehensive two dimensional Computational Fluid Dynamics model for an updraft biomass gasifier," *Renewable Energy,* vol. 99, pp. 698-710, 2016.

[39] S. Gerber and M. Oevermann, "A two dimensional Euler–Lagrangian model of wood gasification in a charcoal bed – Part I: model description and base scenario," *Fuel,* vol. 115, pp. 385-400, 2014.

[40] T. Kolb, M. Aigner, R. Kneer , M. Müller, R. Weber and N. Djordjevic, "Tackling the challenges in modelling entrained-flow gasification of low-grade feedstock," *Journal of the Energy Institute,* vol. 89, no. 4, pp. 485-503, 2016.

[41] S. Fleck, C. Hotz, P. Stoesser and T. Kolb, "Gasification of biomass-based suspension fuels in an atmospheric entrained flow gasifier," in *27. Deutscher Flammentag*, Clausthal-Zellerfeld, 16-17 September 2015.

[42] S. Fleck, U. Santo, C. Hotz, T. Jakobs, G. Eckel, M. Mancini, R. Weber and T. Kolb, "Entrained flow gasification Part 1: Gasification of glycol in an atmospheric-pressure experimental rig," *Fuel,* vol. 217, pp. 306-319, 2018.

[43] T. Kathrotia, C. Naumann, P. Oßwald, M. Köhler and U. Riedel, "Kinetics of Ethylene Glycol: The first validated reaction scheme and first measurements of ignition delay times and speciation data," *Combustion and Flame,* vol. 179, pp. 172-184, 2017.

[44] A. M. Omer, "Biomass energy resources utilisation and waste management," *Journal of Agricultural Biotechnology and Sustainable Development,* vol. 3, no. 8, pp. 149 - 170, 2011.

[45] A. Demirbas, "Combustion characteristics of different biomass fuels," *Progress in Energy and Combustion Science,* vol. 30, no. 2, pp. 219-230, 2004.

[46] C. A. Mullen and A. A. Boateng, "Chemical Composition of Bio-oils Produced by Fast Pyrolysis of Two Energy Crops," *Energy & Fuels,* vol. 22, no. 3, pp. 2104-2109, 2008.

[47] A. Oasmaa, I. Fonts, M. R. Pelaez-Samaniego, M. E. Garcia-Perez and M. Garcia-Perez, "Pyrolysis Oil Multiphase Behavior and Phase Stability: A Review," *Energy & Fuels,* vol. 30, no. 8, p. 6179–6200, 2016.

[48] S. Hafner, A. Rashidi, G. Baldea and U. Riedel, "A detailed chemical kinetic model of high-temperature ethylene glycol gasification," *Combustion Therory and Modelling,* vol. 15, no. 4, pp. 517-535, 2011.

[49] A. Rashidi, S. Hafner and U. Riedel, "Gasification of Ethylene Glycol as Model Substance for Biomass Based Pyrolysis Oil: Detailed Reaction Mechanism Development and CFD Simulation," in *4th European Combustion Meeting*, Vienna, Austria, April 14-17, 2009.

[50] A. I. o. C. E. (AIChE), *Evaluated Process Design Data,* Design Institute for Physical Properties (DIPPR), Project 801, 2006.

[51] M. Kaltschmitt, H. Hartmann and H. Hofbauer, Energie aus biomasse: grundlagen, techniken und verfahren, 2nd Edition, Springer, 2009.

[52] J. Warnatz, U. Maas and R. W. Dibble, Combustion: Physical and Chemical Fundamentals, Modeling and Simulation, Experiments, Pollutant Formation, Springer, 2006.

[53] N. Slavinskaya and M. Braun-Unkhoff, "Reduced Reaction Mechanisms for Methane and Syngas Combustion in Gas Turbines," *Journal of Engineering for Gas Turbines and Power ,* vol. 130, no. 2, 2008.

[54] N. Fernando, T. Kathrotia, Q. Fradet, M. Braun-Unkhoff and U. Riedel, "The oxidation of ethylene glycol - a pyrolysis oil surrogate," in *Proc. 26th European Biomass Conference and Exhibition, Session Code 2BO.14.3*, Copenhagen, Denmark, 14-18 May 2018.

[55] N. A. Slavinskaya and C. Lenfers, "Skeletal Mechanism Production for n-Decane," in *2nd Internat. Workshop on Model Reduction in Reacting Flow*, University of Rome "La Sapienza", Rome, Italy, September 3-5, 2007.

[56] N. A. Slavinskaya, "Skeletal mechanism for kerosene combustion with PAH production," in *46th AIAA Aerospace Sciences Meeting and Exhibit, Paper AIAA 2008 - 0992*, Reno, Nevada, USA, 2008.

[57] A. V. Lebedev, M. V. Okun, V. A. Chorkov, P. M. Tokar and M. Strelkova, "Systematic procedure for reduction of kinetic mechanisms of complex chemical processes and its software implementation," *Journal of Mathematical Chemistry,* vol. 51, no. 1, pp. 73-107, 2013.

[58] T. Methling, M. Braun-Unkhoff and U. Riedel, "A novel linear transformation model for the analysis and optimisation of chemical kinetics," *Combustion Theory and Modelling,* vol. 21, no. 3, pp. 503-528, 2017.

[59] A. Zizin, *Development of a Reduced Chemical-Kinetic Combustion Model for Practical Fuels,* Ph.D dissertation, Institute of Combustion Technology for Aerospace Engineering, University of Stuttgart, 2014.

[60] "Chemical workbench," Kintech Laboratory, [Online]. Available: http://www.kintechlab.com/products/chemical-workbench/. [Accessed 05 12 2018].

[61] "Cantera," [Online]. Available: https://cantera.org/. [Accessed 05 12 2018].

[62] S. Gerber, F. Behrendt and M. Oevermann, "A Comparative Study of Euler-Euler and Euler-Lagrange Modelling of Wood Gasification in a Dense Fluidized Bed," in *In: Yue G., Zhang H., Zhao C., Luo Z. (eds) Proceedings of the 20th International Conference on Fluidized Bed Combustion*, Springer, Berlin, Heidelberg, 2009.

[63] Y. Wu, Q. Zhang, W. Yang and W. Blasiak, "Two-Dimensional Computational Fluid Dynamics Simulation of Biomass Gasification in a Downdraft Fixed-Bed Gasifier with Highly Preheated Air and Steam," *Energy & Fuels,* vol. 27, no. 6, p. 3274–3282, 2013.

[64] E. Loth, "Numerical approaches for motion of dispersed particles, droplets and bubbles," *Progress in Energy and Combustion Science,* vol. 26, no. 3, pp. 161-223, 2000.

[65] M. Mancini, M. Alberti, M. Dammann, U. Santo, G. Eckel, T. Kolb and R. Weber, "Entrained flow gasification. Part 2: Mathematical modeling of the gasifier using RANS method," *Fuel,* vol. 225, pp. 596-611, 2018.

[66] L. Fréret, S. De Chaisemartin, J. Reveillon, F. Laurent and M. Massot, "Eulerian models and three-dimensional numerical simulation of polydisperse sprays," in *Internation Conference on Mutiphase Flows*, Tampa - Florida USA, United States, May 2010.

[67] M. Vujanović, Z. Petranović, W. Edelbauer, J. Baleta and N. Duić, "Numerical modelling of diesel spray using the Eulerian multiphase approach," *Energy Conversion and Management,* vol. 104, pp. 160-169, 2015.

[68] F. Jaegle, J. -M. Senoner, M. García, F. Bismes, R. Lecourt, B. Cuenot and T. Poinsot , "Eulerian and Lagrangian spray simulations of an aeronautical multipoint injector," *Proceedings of the Combustion Institute,* vol. 33, no. 2, pp. 2099-2107, 2011.

[69] W. P. Jones, A. J. Marquis and K. Vogiatzaki, "Large-eddy simulation of spray combustion in a gas turbine combustor," *Combustion and Flame,* vol. 161, no. 1, pp. 222-239, 2014.

[70] "OpenFOAM," [Online]. Available: https://openfoam.org/. [Accessed 05 12 2018].

[71] "OpenFOAM user guide," [Online]. Available:

https://www.openfoam.com/documentation/user-guide/. [Accessed 05 12 2018].

[72] H. K. Versteeg and W. Malalasekera, An Introduction to Computational Fluid Dynamics: The Finite Volume Method, Harlow, England: Pearson Education Limited, 2007.

[73] H. Rusche, *Computational fluid dynamics of dispersed two-phase flows at high phase fractions,* London: Imperial College of Science, Technology & Medicine, Department of Mechanical Engineering, December 2002.

[74] P. P. Baila, "A twoPhaseEulerFoam tutorial," in *Proceedings of CFD with OpenSource Software*, 2008, Edited by Nilsson. H, http://dx.doi.org/10.17196/OS_CFD#YEAR_2008.

[75] D. Cappelli, "A detailed description of reactingTwoPhaseEulerFoam, focusing on the links between mass and heat transfer at the interface," in *Proceedings of CFD with OpenSource Software, 2018, Edited by Nilsson H. http://dx.doi.org/10.17196/OS_CFD#YEAR_2018.*

[76] D. Christ, "Simulating the combustion of gaseous fuels," in *6th OpenFoam Workshop Training Session*, Pennsylvania, United States., 13-16 June 2011.

[77] M. T. Lewandowski and J. Pozorski, "Assessment of turbulence-chemistry interaction models in the computation of turbulent non-premixed flames," *Journal of Physics: Conference Series,* vol. 760, 012015.

[78] D. B. Spalding, "The combustion of liquid fuels," *Symposium (International) on Combustion,* vol. 4, no. 1, pp. 847-864, 1953.

[79] Q. Fradet, M. Braun-Unkhoff and U. Riedel, "A Sectional Approach for the Entrained-Flow Gasification of Slurry Fuels," *Energy & Fuels,* vol. 32, no. 12, p. 12532–12544, 2018.

[80] R. Clift, J. Grace and M. E. Weber, Bubbles, Drops, and Particles, Mineola, NY: Dover Civil and Mechanical Engineering Series, Dover Publications, 2005.

[81] T. Engen, *CFD analysis of gas-particle flow in a scaled circulating fluidized bed,* Stavanger: Faculty of Sicence and Technology, University of Stavanger, 2016.

[82] P. Cheng, "Two-dimensional radiating gas flow by a moment method," *AIAA Journal,* vol. 2, no. 9, pp. 1662-1664, 1964.

[83] S. Haider, K. M. Pang, A. Ivarsson and J. Schramm, "Combustion and radiation modeling of laminar premixed flames using OpenFOAM: A numerical investigation of radiative heat transfer in the RADIADE project," in *CIMAC Congress 2013 Conseil International des Machines a Combustion. (CIMAC Paper; No. 274)*, 2013.

[84] A. Vdovin, "Radiation heat transfer in OpenFoam," in *Proceedings of CFD with OpenSource Software, 2009, Edited by Nilsson H. http://dx.doi.org/10.17196/OS_CFD#YEAR_2009.*

[85] *Ansys Fluent Theroy Guide,* Canonsburg, PA: ANSYS Inc, 2011.

[86] A. Rashidi, CFD Simulation of Biomass Gasification Using Detailed Chemistry, PhD dissertation, Naturwissenschaftlich-Mathematischen Gesamtfakultät, Ruprecht-Karls-Universität, Heidelberg., 2011.

[87] A. Lundström, "reactingFoam tutorial (simple gas phase reaction)," in *Proceedings of CFD with OpenSource Software, 2007, Edited by Nilsson H. http://dx.doi.org/10.17196/OS_CFD#YEAR_2007*, 2007.

[88] H. Jasak, Error Analysis and Estimation for the Finite Volume Method with Applications to Fluid Flows, PhD dissertation, University of London, 1996.

[89] R. I. Issa, "Solution of the implicitly discretised fluid flow equations by operator-splitting," *Journal of Computational Physics,* vol. 62, no. 1, pp. 40-65, 1986.

[90] S. V. Patankar, Numerical Heat Transfer and Fluid Flow, Hemisphere Publishing Corporation, 1980.

[91] "OpenFOAM wiki: OpenFOAM guide/The SIMPLE algorithm in OpenFOAM," [Online]. Available: https://openfoamwiki.net/index.php/OpenFOAM_guide/The_SIMPLE_algorithm_in_OpenFOAM. [Accessed 02 04 2019].

[92] "CFD: PIMPLE Algorithm," [Online]. Available: https://www.simscale.com/forum/t/cfd-pimple-algorithm/81418. [Accessed 02 04 2019].

[93] E. Roohi, M. Pendar and A. Rahimi, "Simulation of three-dimensional cavitation behind a disk using various turbulence and mass transfer models," *Applied Mathematical Modelling,* vol. 40, no. 1, pp. 542-564, 2016.

[94] A. Manni, *An introduction to twoPhaseEulerFoam with addition of an heat exchange model in 23x version,* Dept of Industrial Engineering, University of Rome "Tor Vergata", Italy, 2014.

[95] P. Dagaut, M. Reuillon, D. Voisin, M. Cathonnet, M. McGuinness and J. M. Simmie, "Acetaldehyde Oxidation in a JSR and Ignition in Shock Waves: Experimental and Comprehensive Kinetic Modeling," *Combustion Science and Technology,* vol. 107, no. 4-6, pp. 301-316, 1995.

[96] V. P. Zhukov, "Kinetic model of alkane oxidation at high pressure from methane to n-

heptane," *Combustion Theory and Modelling,* vol. 13, no. 3, pp. 427-442, 2009.

[97] J. Herzler and C. Naumann, "Shock Tube Study of the Ignition of Lean CO/H2 Fuel Blends at Intermediate Temperatures and High Pressure," *Combustion Science and Technology,* vol. 180, no. 10-11, pp. 2015-2028, 2008.

[98] M. Christensen, M. T. Abebe, E. J. K. Nilsson and A. A. Konnov, "Kinetics of premixed acetaldehyde+air flames," *Proceedings of the Combustion Institute,* vol. 35, no. 1, pp. 499-506, 2015.

[99] A. Van Maaren, D. S. Thung and L. P. H. De Goey, "Measurement of Flame Temperature and Adiabatic Burning Velocity of Methane/Air Mixtures," *Combustion Science and Technology,* vol. 96, no. 4-6, pp. 327-344, 1994.

[100] F. N. Egolfopoulos, P. Cho and C. K. Law, "Laminar Flame Speeds of Methane-Air Under Reduced and Elevated Pressures," *Combustion and Flame,* vol. 76, no. 3-4, pp. 375-391, 1989.

[101] C. A. Callaghan, Kinetics and Catalysis of the Water-Gas-Shift Reaction: A Microkinetic and Graph Theoretic Approach, PhD dissertation, Department of Chemical Engineering, WORCESTER POLYTECHNIC INSTITUTE, 2006.